Self-assembly and Luminescence Properties of Alkyl Ammonium Gold(I) Iso-maleonitriledithiolate Coordination Polymers

by

Khuong Duy Ho

B.Sc., University of the Fraser Valley, 2021

Thesis Submitted in Partial Fulfillment of the
Requirements for the Degree of
Master of Science

in the
Department of Chemistry
Faculty of Science

SIMON FRASER UNIVERSITY
Summer 2024

Declaration of Committee

Name:	**Khuong Duy Ho**
Degree:	**Master of Science**
Title:	**Self-assembly and Luminescence Properties of Alkyl Ammonium Gold(I) Iso-maleonitriledithiolate Coordination Polymers**
Committee:	**Chair: Loren G. Kaake** Associate Professor
	Daniel B. Leznoff Co-supervisor Professor, Chemistry
	Vance E. Williams Co-supervisor Professor, Chemistry
	Jeffrey J. Warren Committee Member Associate Professor, Chemistry
	Tim Storr Committee Member Professor, Chemistry
	Gary W. Leach Examiner Associate Professor, Chemistry

Abstract

This thesis focuses on the design of tunable photoluminescence, control of supramolecular packing, and the preparation of stimuli-responsive gold(I) coordination polymers. This is explored *via* gold(I) *iso*maleonitriledithiolate, $[Au_2(i\text{-mnt})_2]^{2-}$ as the anionic building block, with soft cations containing long alkyl chains in the form of tetraalkylammonium, $[(C_nH_{2n+1})_4N]^+$ and alkyltrimethylammonium, $[RMe_3N]^+$ (where n = 5, 7, 8 and R = C_4H_9, C_8H_{17}, $C_{10}H_{21}$, $C_{16}H_{33}$). These structures were synthesized and displayed luminescent properties, with the emission colour ranging between green, orange, and red at room temperature due to the presence of aurophilic interactions.

Modifications in the alkyl chain-length in $[RMe_3N]_2[Au_2(i\text{-mnt})_2]$ resulted in changes in supramolecular packing - from columnar to smectic C–like structures with $[C_{16}Me_3N]_2[Au_2(i\text{-mnt})_2]$. Notably, the C_{16}-containing structure shows mechanical softness inherent from the parent surfactant cation $[C_{16}Me_3N]^+$, where alterations in structural and emission properties occur upon applying mild pressure from the tip of a spatula.

Keywords: Aurophilicity; Gold(I); Coordination Polymers; Luminescence; Supramolecular Packing; Soft Materials

To my families

Acknowledgements

This work would not have been possible without the help and support of many people. First and foremost, I would like to express my undying gratitude and appreciation to both of my supervisors, Prof. Daniel Leznoff and Prof. Vance Williams for their guidance, limitless patience, deep understanding, sympathy, and invaluable support they have given me throughout my degree. Danny and Vance were and are the most awesome professors and mentors that taught me so many skills, lessons, and wisdom that I will carry throughout the rest of my life. I also acknowledge and thank my undergraduate supervisors Dr. Jacob Spooner and Dr. Linus Chiang for kindling my interest in chemistry research at SFU and for the countless talks we had.

I would like to thank all members of the Leznoff group that I have the chance to work with for all the advice on research problems, presentations, and directions for my research. A special thanks to Jefferson Pells for his patience with me and for providing instrumental training and guidance on pretty much everything about coordination polymers. Thank you to Thomas Karpiuk, Leanna Karn, Steven Kidd, and Dr. Yumeela Ganga-sah for all the numerous interesting conversations and help about science and life. Thank you to Dr. Wen Zhou for also helping to training me to run XRD and running my elemental analysis. Thank you to all members of the Williams group for showing me the amazing world of liquid crystals and giving advice, feedback, and insight on my research from another different area. Thank you to Simranjeet Kaur and Homayoun Ghaseminezhad for all the fun talks and helps. Another special thanks to Dr. Carson Zellman for training me in running DSC and POM.

Thank you to my supervisory committee members Prof. Jeffrey Warren and Prof. Tim Storr for their thoughtful perspective and feedback on research and taking the time to read my thesis.

Thank you to Dr. Rebecca Goyan, Dr. Garry Mund, and Dr. John Canal for all the enjoyable talks and help during TA time. Thank you to the SFU chemistry department for financial assistance.

To my families, my mother and father, my aunt and uncle, thank you for believing in me, thank you for always being there, thank you for all the immense emotional support, love, and guidance, and thank you for always looking after me through the ups and downs.

Thank you to my beloved girlfriend Thy for has always been so supportive and bear with my garrulousness.

Table of Contents

List of Tables

List of Figures

List of Symbols and Abbreviations

0D	Zero-dimensional
1D	One-dimensional
2D	Two-dimensional
3D	Three-dimensional
Å	ångstrom (unit), $1x10^{-10}$ m
ATR	Attenuated total reflectance
CP	Coordination polymer
CTAB	cetyl ammonium bromide
DMF	Dimethylformamide
DMSO	Dimethylsulfoxide, $(CH_3)_2SO$
dopdtc	Di(*o*-pyridyl)aminedithiocarbamate
DSC	Differential scanning calorimetry
EA	Elemental analysis
EMM	Excitation-emission matrix
EtOH	Ethanol
HDMG	Dimethylglyoxime
HOMO	Highest occupied molecular orbital
imi	Imidazolium
i-mnt	*Iso*maleonitriledithiolate
i-Pr	Iso-propyl
i-PrOH	Propan-2-ol
IR	Infrared (spectroscopy)
LLCT	ligand to ligand charge transfer
LMCT	ligand to metal charge transfer
LUMO	Lowest unoccupied molecular orbital
Me	Methyl
Me_3Ph	1,3,5-bis(trimethyl)diphenyl
MeCN	Acetonitrile
MeOH	Methanol

MLCT	metal-to-ligand charge transfer
MM	Metal-metal interaction
mnt	Maleonitriledithiolate
MOF	Metal-organic framework
n	Normal, i.e. straight chain
Pedtc	Dipentyldithiocarbamate
PXRD	Powder X-Ray diffraction
SC-XRD	Single crystal X-Ray diffraction
SFU	Simon Fraser University
SmC	Smectic C liquid crystal
TGA	Thermogravimetric analysis
thf	Tetrahydrofuran
tht	tetrahydrothiophene
UV	Ultraviolet
UV-Vis	Ultraviolet-Visible
λ	Lambda, wavelength

Chapter 1. Introduction

1.1. Coordination Polymer

The field of coordination polymers (CPs) has been an active research area, averaging more than 1000 articles per year for the last 10 years. The term “coordination polymer” was first used by J. C. Bailar in 1967 to describe inorganic complexes that can repeatedly bind like polymers. Unlike traditional polymers, it was established from the beginning that both metal and ligands should be present, held together by metal-ligand coordination bonds, in order to be termed as CPs.[1]

Coordination polymers are defined as entities consisting of two elementary building blocks: the metal nodes and the linkers that join them together via direct coordination bonds or weaker non-covalent interactions in the solid state.[1] As a result, CPs can propagate in up to three dimensions, including linear 1D chains, 2D sheets, and 3D networks as shown in Figure 1.1.[2,3] An important subset among the CP family is metal-organic frameworks (MOF), which normally contain empty voids (i.e., they are porous) and extend into ordered 3D structures.[4] CPs can show a diverse range of properties and applications, such as birefringence,[5] chemical sensing,[6,7] catalysis,[8,9] porosity,[10,11] magnetism,[12,13] functional gels,[14,15] and many others.[16-22] One way to approach CP research is to think of it as a game of architecture. Depending on the desired properties, structural topology, and applications, chemists can choose suitable building blocks through multiple combinations of metals and linkers. This makes CPs a flexible and intriguing platform to investigate and engineer new materials.

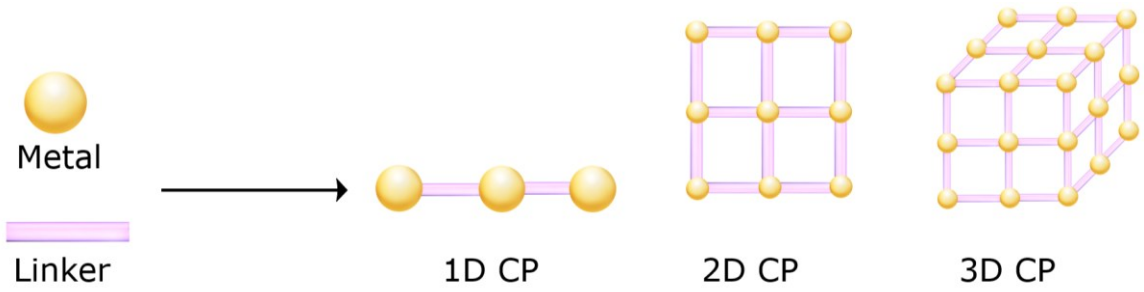

Figure 1.1: Cartoon representation demonstrating 1-, 2-, and 3-dimensional coordination polymer networks.

Further exploring the process of constructing CPs, the observed dimensionality of CPs is usually related to factors like the number of available coordination sites on the metal, any non-covalent interactions between the building blocks, whether the solvent can act as a ligand, and if neutral linker ligands are used, what counter ions are used. In any case, the overall network of the CP is built using metal-ligand coordination bonds and the geometric factors that direct this propagation are critical. For example, a linear node can bind repeatedly with linear linkers, resulting in a repeating linear structure; tetrahedral or octahedral nodes will likely favour more high dimensionality structures. Stoichiometry between metal and linkers could also dictate the dimensionality of structure (e.g., stoichiometry of 1 to 2 or 1 to 3 between metal and linkers could result in a 2-D or 3-D structure). Similarly, the number of binding sites on the linker can influence the dimensionality of the structure. For instance, 1,4-pyrazine is a ditopic linker; when combining it with silver(I), a parallel 1-D chain structure was obtained, whereas the tritopic linker 1,3,5-triazine formed 3-connected nets with silver(I) (Figure 1.2).[23,24]

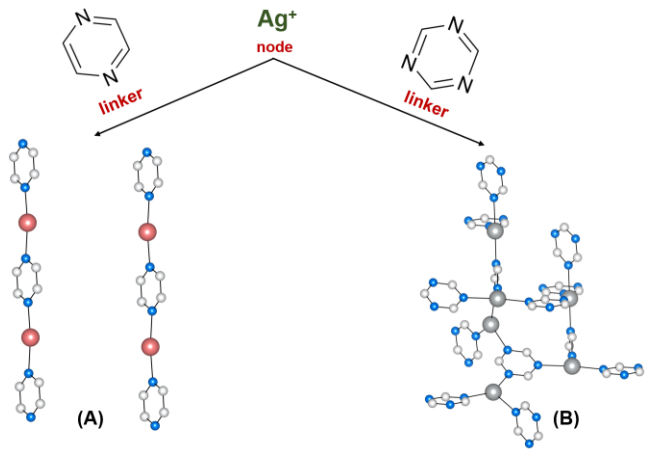

Figure 1.2: Examples of how different topicity of the linker influences the dimensionality of structures with a Ag(I) node. (a) parallel 1D chains, and (b) 3-D nets. The counter ion has been omitted for clarity. Light grey, Ag; blue, N; white, C.

On the other hand, capping ligands can be used to restrict the framework growth, hence lowering dimensionality of the nets; in extreme cases, this can create 0-D supramolecular structures, as reported by Fujita and co-workers.[25] In addition, the product CPs can inherit properties from the starting building blocks; these properties can be enhanced due to the cooperative effects of coordination polymer structures. For example, incorporating luminescent metal ions like lanthanides or gold(I) can bring emissive

character to CPs, metals with unpaired electrons can induce magnetic properties in the materials, or geometric features can engineer porous, as seen in MOF materials, and birefringent systems.[26] One should also take into account other factors like steric bulk effects, crystal growth, interpenetration, and non-covalent interactions, all of which can alter the final topology of CP frameworks.[27]

It should be highlighted that major beneficial features of working with CPs include their simplicity and tunability. Most CP chemical reactions are completed in one-step; the syntheses are often simply the addition of both the metal and ligands in appropriate experimental conditions and solvent system, with the CP products isolated as precipitates from the mixture. Synthesis of a range of derivates of nodes and linkers can be done in matrix fashion to better understand the relationship between component building blocks, properties correlation, and optimize the materials for various applications. However, the most difficult step perhaps lies in crystal growth. Many structural properties and parameters can be acquired from the crystallographic analysis of single crystal X-Ray diffraction (SC-XRD) data, hence there is a significant reliance on high-quality crystals procured from crystal growth techniques. Powder X-Ray diffraction (PXRD) data can be obtained to compare new systems that are the same in structural composition and crystallographic parameters, i.e., are isomorphous, or to confirm already known structures.[28]

The mixing of component building blocks and metal ion in general yields micro-crystalline precipitates of the CP products. As these powdered products are not easily amenable toward structural determination, the next step is the (informed) “trial and errors” of crystal growth. A few methods and crystal growing techniques involved in this research are listed below. Depending on the solubility profile of the building blocks and the CP product, the simplest method is slow evaporation of a soluble product, which should be carried out by completely solubilizing the starting materials in a minimal amount of solvent (raising the temperature or sonication can also assist this process), then allowing excess solvent to evaporate slowly over time until at a particular concentration point, nucleation happens and crystals suitable for SC-XRD could develop (Figure 1.3).

The second technique is vapour diffusion: the powdered CP is dissolved in a solvent where it is moderately soluble, in a small chamber/vial. The next step is to place this vial in a larger sealed vessel which is partially filled with a different solvent that meets

the following requirements: low boiling point, does not dissolve the CP product, and is miscible with the inner solvent. As the outer solvent diffuses inside the chamber over time, the product would become insoluble in the mixture, and at the nucleation point crystals could begin to grow (Figure 1.4).

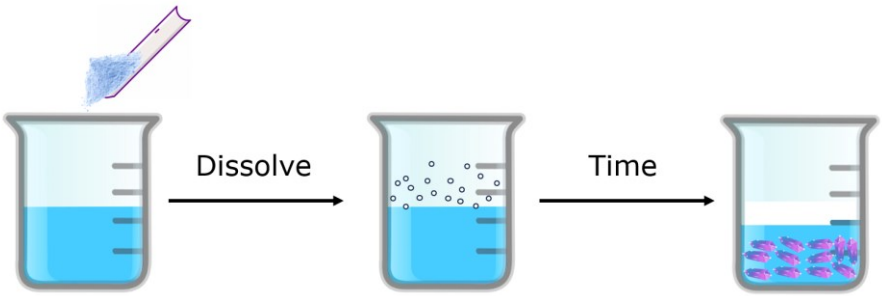

Figure 1.3: Simple illustration of slow evaporation method. The powdered product is completely dissolved by either applying heat or sonication, then the mixture is allowed to concentrate and crystals could form over time.

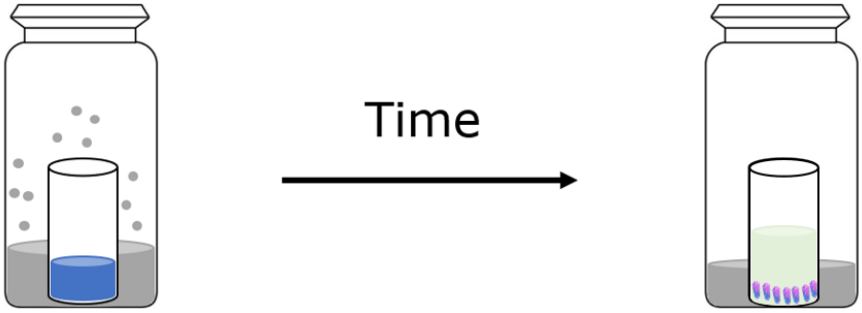

Figure 1.4: Illustration of vapour diffusion. The CP product is pre-dissolved in minimal solvent and placed inside a large, sealed vessel, filled with another solvent in which the CP would not be soluble (left). The crystal growth begins as more solvent diffuses inside the small vessel and the product becomes insoluble in the mixture (right).

Another technique similar to vapour diffusion is layered diffusion. Instead of using two vessels, it is performed in a test tube involving two miscible solvents that are different in density. The compound should be solubilized in the denser solution, then put in an empty tube. It is critical to avoid disturbance when adding the less dense solution on top of the content as otherwise it would cause powdered products to crash out immediately; thus, this addition should be done with a syringe. Crystals would grow gradually as the two layers diffuse slowly together and the contents become less soluble (Figure 1.5). Additionally, this method can also be used for setting up reactions between a metal and linker where these components are separated in two different layers and as these layers

slowly diffuse into each other, the reaction occurs accordingly slowly. These methods listed above are some of the oldest, most widely used in crystal growth and are classified as in-solution growth.[29] Alternatives to these traditional methods are using electric potential (electro-crystallization), ultrasound, mechanical force, and electromagnetic radiation.[30] Though systems differ case by case and certain techniques could not guarantee desirable and high-quality crystals all the time, one should attempt and decide which methods would work best.

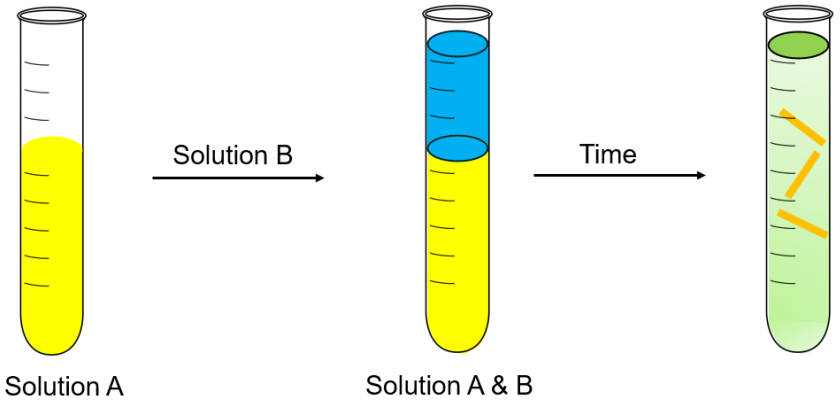

Figure 1.5: The layered diffusion technique; two miscible solutions A and B are sequentially added to a long vessel and slow diffusion of both solutions over time prompts formation of crystals. Solution A and B contain metal node and linker respectively (or vice versa).

1.2. Aurophilicity in Luminescent Coordination Polymers

1.2.1. Aurophilicity

Gold(I) chemistry is considered among the most fascinating fields of chemistry and is widely applicable to prominent areas including medicinal chemistry,[31] catalytic reactions,[32] the electronics industry,[33] and biotechnology.[34] Perhaps the most interesting property lies in its strong photoluminescence.[35] This optical emission source is achieved by utilizing the concept of aurophilicity.

Aurophilicity refers to the observation of short Au(I) – Au(I) attractive interactions and was first introduced by Schmidbaur in 1989.[36] A more general term - "metallophilicity" - was later coined to describe this phenomenon, which occurs in closed-shell systems such as s^2, d^{10}, and pseudo closed-shell d^8 ions. Aurophilic bonds have an average length of 2.7 Å – 3.6 Å, and energies between 5 kcal mol^{-1} and 15 kcal mol^{-1}.[37-39] The nature of a metallophilic interaction is a non-covalent metal-metal attraction that is weaker than an ionic bond, stronger than a typical van der Waals interaction and comparable in strength to a standard hydrogen bond, thus it is sometimes referred to as a "super van der Waals" interaction. An early example of this gold – gold interaction was found in the $[Au^{III}(HDMG)_2][Au^{I}Cl_2]$ complex between gold(III) and gold(I) centres (HDMG = dimethylglyoxime). A more relevant example of the much more common gold(I) – gold(I) interaction was later found in the Cl_3PAuCl complex in 1962. Some recent examples that highlight the usage of gold(I) – gold(I) bonds include the work of Schmidbaur,[39] Puddephatt,[40] Laguna,[41] Yam,[35] Fackler,[42] and Leznoff.[43]

Aurophilicity, or metallophilicity of heavy elements in general can be enhanced by relativistic effects roughly by 20%, as noted by theoretical calculations performed by Pyykkö et al.[44] A relativistic effect is a phenomenon derived from Einstein's theory of relativity where electrons of the outer orbitals in heavy elements have an increasing average velocity and approach the speed of light (due to the higher positively charged nucleus), thus leading to an increase in mass of the outer electrons and a contraction of the inner s and p orbitals. As a consequence of this phenomenon, mercury is a liquid at room temperature due to weak relativistic effects, and gold absorbs blue wavelengths of light to reflect a shiny yellow colour.[45,46] The combination of relativistic effects, with the

greatest effect observed in gold, and aurophilic interactions gives rise to the unique colour and luminescent behaviour in gold(I) complexes.

Generally, the two common oxidation states of gold compounds are Au(I) and Au(III), yet Au(III) exhibits much weaker aurophilic interactions than Au(I) due to its high Coulombic repulsion.[47] For simple systems that contain aurophilic interactions in the form of linear, two-coordinate gold(I) AuR_2, where R can be an anionic or neutral ligand, the relevant mechanism of this luminescent property can be described as the transition from the $5d\sigma^* \longrightarrow 6p\sigma$ where the $5d\sigma^*$ is an antibonding orbital of $5d_z^2$ and $6s/6p_z$ (with the direction of aurophilic interaction is defined as the principle z-axis). The emission of a gold(I) complex can also originate from other pathways such as metal-to-ligand charge transfer (MLCT), or in some less common cases, ligand to metal charge transfer (LMCT), and ligand to ligand charge transfer (LLCT) in addition to its primarily metal-metal interaction from aurophilicity.[48] Au(I) atoms are also capable of forming an infinite 1-D gold(I) chain that is held by aurophilic interactions and self – assembly into various structures. The bond strength of a 1-D gold(I) chain is notably stronger than a diatomic Au(I) – Au(I) aurophilic system, thus reducing the energy gap between the HOMO and LUMO, resulting in a red – shift in emission spectra of 1-D chain systems compared to isolated Au(I) dimers.

The concept of closed – shell metal ions with the same charges forming an attractive bond was initially viewed as implausible. While the molecular orbital diagram for a closed – shell d^{10} dimer system does not fully explain why these metallophilic interactions are an attractive interaction, it was suggested that metallophilic and particularly aurophilic interactions are induced by correlation effects and enhanced by relativistic effects.[83] A more reasonable and accepted view currently for metallophilic and aurophilic interactions is that they are driven by London dispersion forces.[39, 44, 83] The strength of this interaction decreases as distance increases, obeying the rule of London dispersion force. In short, the attractive force between Au(I) atoms are largely van der Waals interactions that are strengthened by strong relativistic effects.

1.2.2. Using aurophilicity to generate multidimensional structures

In addition to the useful property of photoluminescence, it has been shown that aurophilicity can be utilized to increase the dimensionality of a supramolecular structure.

One of the most well-known compounds in gold chemistry is the ditopic, linear, gold(I) containing anion dicyanoaurate, $[N{\equiv}C\text{-}Au\text{-}C{\equiv}N]^-$, which was first mainly employed for gold cyanidation - the process of extracting gold by combining aqueous cyanide solutions and gold metal. It is also a metabolite from Au(I)-based drugs and used as a starting material for reactions, notably as a versatile building block in coordination polymer chemistry.

Dicyanoaurate features a linearly coordinated and sterically unhindered gold(I) metal centre which can form aurophilic interactions with neighboring dicyanoaurate anions, and the lone pairs on the terminal nitrile groups can act as donors to another Lewis metal and form CPs. This aurophilic bond is perpendicular to the linear dicyanoaurate anion, and could potentially increase the overall supramolecular dimensionality of the CP. Various examples of dicyanoaurate-based CP (including work from the Leznoff group) have featured their structural properties and magnetism,[49-56] birefringence,[57-62] included emissive lanthanide dicyanoaurate-based materials,[63] and illustrated thermal expansion.[64] The Patterson group also investigated primarily the structural and photophysical properties of various dicyanoaurate-based CPs.[65-77] These are some of many examples showcasing the versatility of not only dicyanoaurate but also aurophilicity in coordination polymers applications.

Designing emissive multidimensional structures using dicyanoaurate should include another metal cation such as zinc (since it is colourless), or one of the lanthanides that are independently emissive and have a range of coordination number from 3 to 12.[78] For example, $Zn[Au(CN)_2]_2$ exists in multiple polymorphs (termed α, β, γ, and δ).[79,80] In regard to the structure of α-$Zn[Au(CN)_2]_2$, it features four-coordinate N-cyano binding around a tetrahedral zinc(II) centre. (Figure 1.6) The N-cyano group comes from the terminal nitrile on dicyanoaurate, and these dicyanoaurate anions are held together by aurophilic interactions, with Au – Au distances of 3.11 and 3.16 Å. This Au(I) – Au(I) interaction creates multiple aurophilic chains to form an overall 3-D hexagonal network and is responsible for the blue emission at 390 and 480 nm. Interestingly, $Zn[Au(CN)_2]_2$ is sensitive to ammonia vapour, which results in yellow powder $[Zn(NH_3)_2][Au(CN)_2]_2$ after exposure. The structure consists of octahedral zinc(II) centres linked to axial ammonia and equatorial N-cyano units from dicyanoaurate. It has shorter Au – Au interactions of 3.06 Å than its parent structure, with red-shifted emission to green at λ_{max} = 500 nm. This illustrates the dynamic coordination sphere of zinc(II), changing coordination number from

4 to 6 after ammonia exposure and also the potential of luminescent sensory materials using dicyanoaurate.

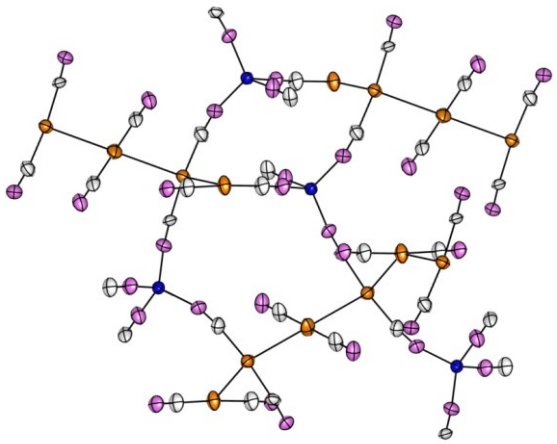

Figure 1.6: Crystal structure of α-$Zn[Au(CN)_2]_2$ with aurophilic interactions as chains.[79] Colour scheme: Au, orange; Zn, blue; C, white; N, pink.

Despite being a useful framework in heterobimetallic coordination polymers, the formation of aurophilicity in dicyanoaurate materials does not always occur, as any presence of stronger repulsive interactions or steric bulk could suppress the weak attractive aurophilic interaction in the solid-state structure.[81] While the nature of the closed-shell interaction of aurophilicity is unchangeable, it was suggested that the strength of Au(I) – Au(I) interactions can be enhanced by changing to a more polarizable donor on the gold(I) centre, in particular iodo- and thio-based ligands.[82-84]

Thus, one candidate that offers improved chemical softness (a more polarizable framework) and is more ideal than cyanide to incorporate aurophilic bonds is gold(I) thiol-based complexes, or aurothiolate motifs. Two common classes of aurothiolates include monodentate, $[Au(SR)]_n$, and bidentate dithiolate ligands, RCS_2Au, in which this bidentate dithiolate form already contains an inherent intramolecular aurophilic core in the motif (Figure 1.7).

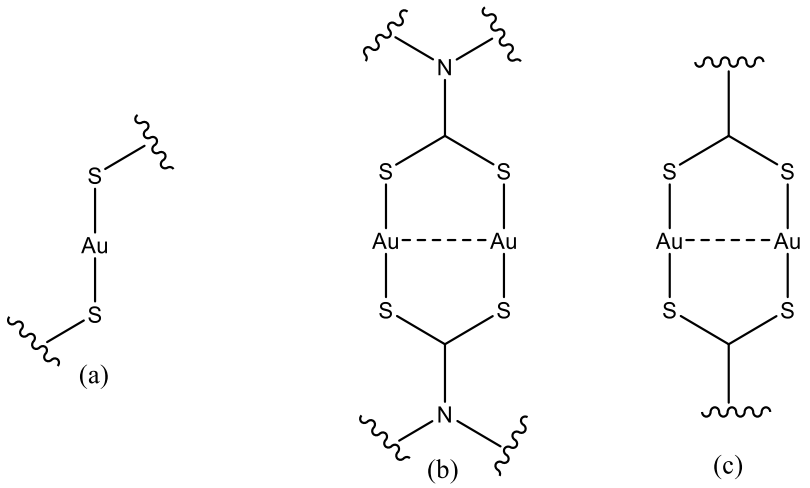

Figure 1.7: Examples of different thiol-based gold(I) moieties (a) Two coordinate monodentate gold(I) thiolate, (b) bis(dithiocarbamatogold(I)), and (c) bis(dithiolategold(I)) which adopts the bidentate dithiolate framework containing an intramolecular aurophilic core.

Some examples of bis(dithiocarbamatogold(I)) complexes including the work on dipentyldithiocarbamate, ($[S_2CN(C_5H_{11})_2]^-$, $Pedtc^-$) which can respond to volatile organic compounds.[85] The unsolvated colourless crystal $[Au(Pedtc)]_2$ is non-emissive due to its structure containing isolated dimers of $[Au(Pedtc)]_2$ with large intermolecular Au – Au distances of 8.135 Å between [Au(Pedtc)] units while still retaining an intramolecular Au(I) – Au(I) interaction (Figure 1.8a). Exposing the crystals to dimethyl sulfoxide (DMSO) solvent changed the colourless powder to orange and induced the formation of intermolecular aurophilic interactions between dimers of $[Au(Pedtc)]_2$ to create an infinite 1-D gold(I) chain with a short intermolecular aurophilic interaction of 2.968 Å (Figure 1.8b).

Another example of the bis(dithiocarbamatogold(I)) class that the Leznoff group reported is $[Au(dopdtc)]_2$ (dopdtc = di(*o*-pyridyl)aminedithiocarbamate).[86] This structure features aggregation in the solid state between $[Au(dopdtc)]_2$ units with intermolecular Au – Au interactions of approximately 2.9 – 3.1 Å (Figure 1.9a). Interestingly, the Au-Au-Au angles deviated from linearity to a twisted conformation of approximately 108° and 166°, which formed an overall 1-D kinked staircase aurophilic chain instead of the usually observed linear or nearly linear chain (Figure 1.9b).

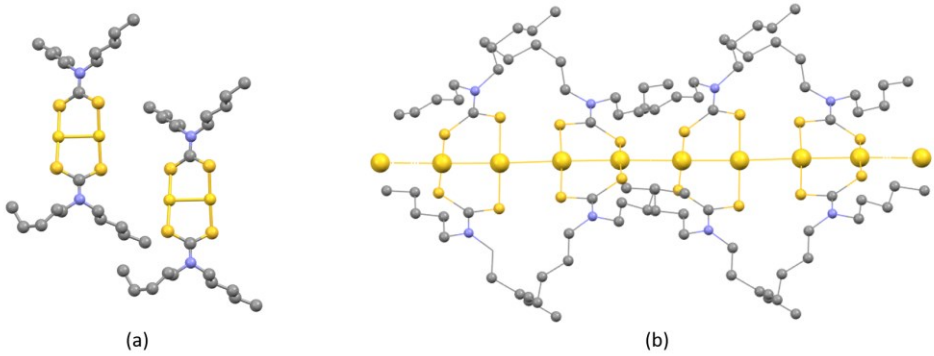

Figure 1.8: Crystal structure of (a) non-solvated and non-luminescent $[Au(Pedtc)]_2$ showing isolated dimers of $[Au(Pedtc)]_2$ and (b) solvated structure of $[Au(Pedtc)]_2$·DMSO containing infinite 1-D gold(I) chain that displays photoluminescent properties (DMSO solvent and hydrogen atoms removed for clarity). Colour scheme: Au, orange; S, yellow; C, grey; N, blue.

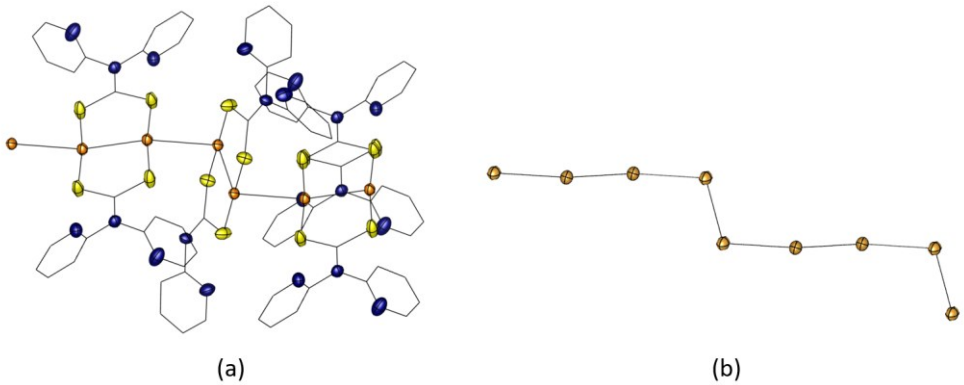

Figure 1.9: (a) Crystal structure of $[Au(dopdtc)]_2$ containing kinked 1-D aurophilic chain (b) 1-D kinked staircase aurophilic chain of $[Au(dopdtc)]_2$ (carbon atom showed as wire frame and hydrogen atoms removed for clarity). Colour scheme: Au, orange; S, yellow; N, blue.

1.2.3. Origin of photoluminescent properties

Compounds containing aurophilic interactions are often emissive. The origin of this luminescence has been discussed briefly above, and the basic concept of luminescence can be summarized and represented more in detail by using a Jablonski diagram (Figure 1.10).[124] When a chromophore encounters a photon, the photon's energy may be absorbed, corresponding to a transition to a permissible vibrational sub-level of the electronic excited state. The energy of the excited electron can be dissipated in multiple ways, with two of the more mechanisms being vibrational relaxation and resulting heat loss to the environment, or by relaxation with accompanying emission of a photon.

Vibrational relaxation is a non-radiative process whereby the excited electrons first drop to the ground vibrational state of the excited electronic state. The excess energy is then converted as kinetic energy to other vibrational modes, which could lead to a variation in dipole moment, bond length and angle in the excited state's molecular structure. If the vibrational energy state overlaps with electronic states, an internal conversion occurs, and the excited electron transitions from the higher excited electronic energy state back to the electronic ground state, and it must maintain the same spin state through the transition.

The chromophore in the vibrational ground state of the lowest excited electronic energy state can also relax back to the ground state via photoemission in a process known as photoluminescence. This is a fast transition, on the order of nano to microseconds after the electron is excited, with an excited state-lifetime in the range of 10^{-9} to 10^{-6} seconds. In fluorescence, the spin state of the electrons remain the same during the transition to the ground state, i.e., the transition is a singlet – singlet transition ($S_1 \rightarrow S_0$). The emitted photon has a longer wavelength than the wavelength of absorbed photons due to non-radiative relaxation processes in the excited state. The wavelength difference between the maximum of the excitation band and the maximum of the emission band is termed the Stokes shift. Emission bands are generally broad due to multiple vibrational ground states that electrons can relax back into. A plot of an emission spectrum for given excitation wavelength and excitation spectrum for given emission against excitation wavelength is obtained in this manner (see Section 1.6). Fluorescence can only occur after an analyte has absorbed radiation, and hence the intensity of emitted light will vary depending on the amount of light absorbed. As such, the excitation spectrum, which plots the emission intensity as a function of excitation wavelength, often closely matches the absorption spectrum of the compound.[125]

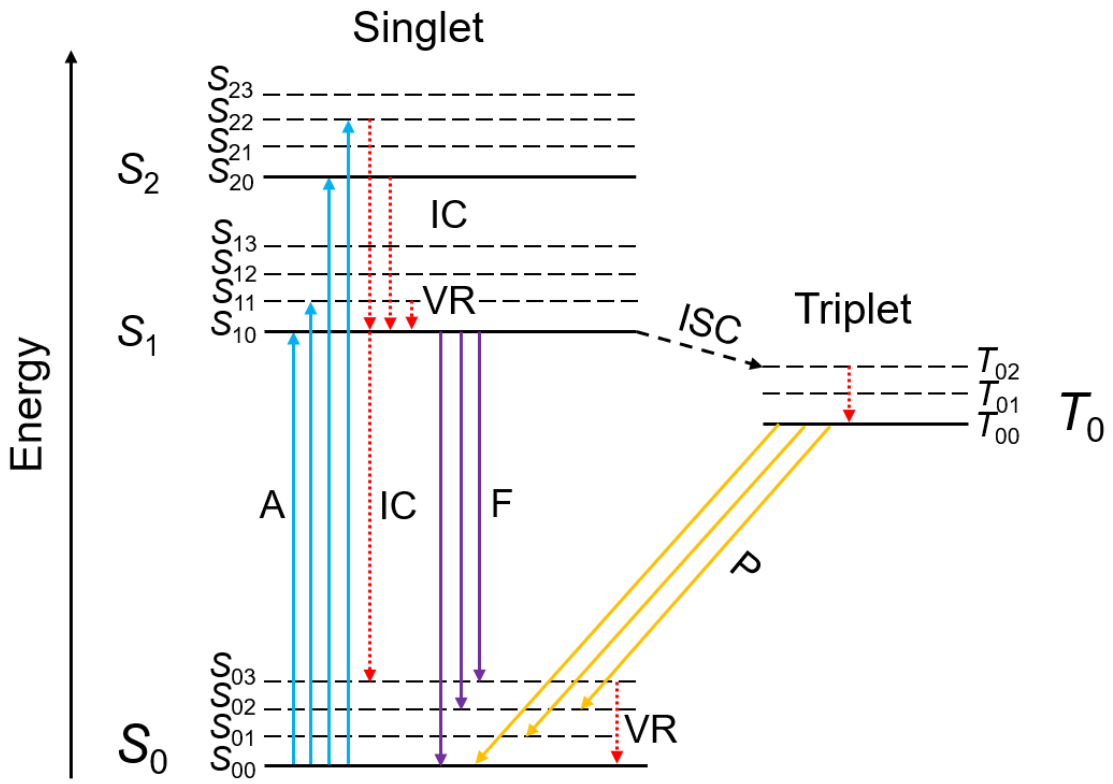

Figure 1.10: Schematic representation of the important processes that occur in photoluminescence spectroscopy, commonly known as a Jablonski diagram. The notations drawn as solid arrows are referred to absorption (A, light blue), fluorescence (F, purple), and phosphorescence (P, orange). The dissipation of energy are drawn as red dashed arrows referred to as internal conversion (IC) or vibrational relaxation (VR) and intersystem crossing (ISC, black). The horizontal columns are specific spin multiplicities and each substate within the horizontal column is shown as eigenstates. Within each electronic state, a possible vibrational state of the molecule is coupled with that particular electronic state. Xyz refers to the y'th excited electronic state molecule with 0 being the ground state and z'th vibrational substates of the singlet (X = S) or triplet (X = T) state.

Phosphorescence is another photoemission pathway by which excited electrons can return to the ground electronic state. This occurs when the process of conversion from excited singlet state (S_{10}) to the triplet state (T_{02}) through intersystem crossing (ISC) occurs. This is possible due to the similarity in energy level of the lowest vibrational level of the excited singlet state and the upper vibrational energy level of a triplet state. The transitions between a ground state singlet and excited triplet states are formally forbidden from taking place, and thus phosphorescence requires a minimum of 10^{-4} seconds up to 10^{2} seconds. This long excited state-lifetime is a key feature of phosphorescence,

reflecting the conversion of spin state from an excited triplet state to the singlet ground state. Due to the non-radiative energy loss in ISC, phosphorescence emission occurs at a lower energy (higher wavelength) than the corresponding fluorescence, leading to a larger Stokes shift.

The intensity of these transitions is dictated by the difference in population of initial and final vibronic transitional electronic states, which can be explained and calculated by using the Franck-Condon principle (Figure 1.11). In a classical picture, the Franck-Condon principle approximates that the electronic transition likely occurs on fixed nuclear coordinate due to larger size of nuclei than electrons, thus resulting in a relatively slow nuclear motion compared to the fast electronic transition. In the quantum mechanical terms of the Franck – Condon principle, this separation of electronic and vibrational wavefunctions is based on the fundamental assumption of the Born–Oppenheimer approximation, where wavefunctions of the molecular states of electronic and vibrational components are separated. The probability of a vibronic transition is proportional to the overlap integral between their vibrational wavefunctions. The ground state v'' = 0 is the most populated according to the Boltzmann distribution at room temperature and absorption would mostly happen from this particular energetic level. Given the shift in nuclear coordinates of the excited singlet state, the absorption generally populates a higher vibrational level instead of the lowest excited singlet state v' = 0, as example by v' = 3 in Figure 1.11. This transition dictates the absorption maximum of the molecule. The excess vibrational energy is lost, and fluorescence would occur from only the lowest excited singlet state v' = 0, which is termed Kasha's rule, to the ground state at a longer and fixed nuclear coordinate. This energy gap dictates the fluorescence maximum of the molecule.

These concepts are important toward understanding the complex nature of photoluminescent properties for aurophilic containing frameworks. A flexible system with many degrees of freedom would result in more opportunities for non – radiative processes and vice versa.

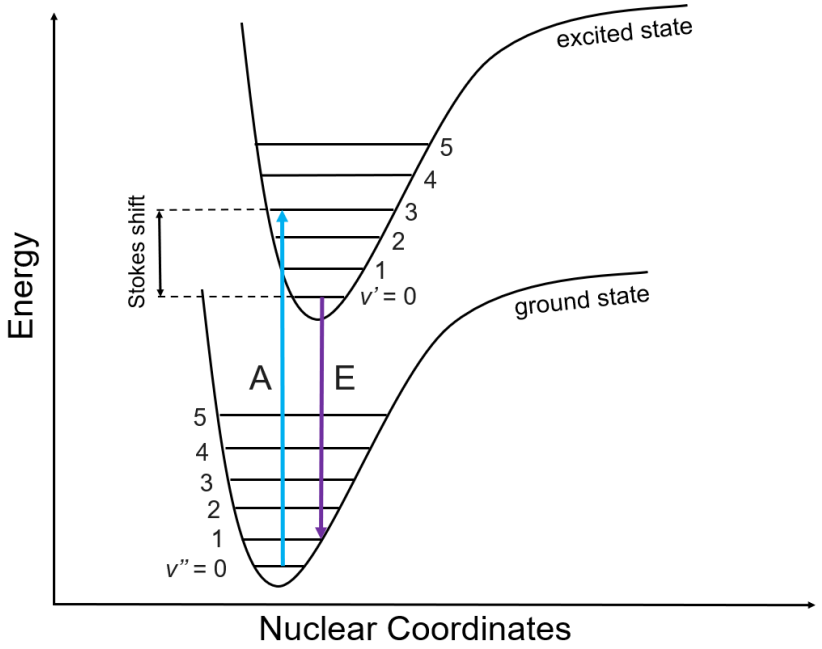

Figure 1.11: The Franck – Condon energy diagram depicts a hybrid picture between classical and quantum mechanics. The y – axis shows the energy of the molecule and the x – axis is the nuclear separation. v'' and v' represent quantum numbers of the ground state and excited state. The solid arrows indicate Absorption (A), and Emission (E). Absorption leads to a higher energetic state and fluorescence leads to a lower energetic state, and the shift in nuclear coordinates between ground and excited states indicates a new equilibrium separation distance between nuclei in that state.

1.3. [Au(mnt)] and [Au(*i*-mnt)] materials and the literature knowledge

With the above points in mind, efforts to design 2nd generation CPs with pre-existing aurophilic interactions beyond dicyanoaurates focused on several requirements. The CP framework targeted should ideally exhibit photoluminescent properties that arise from aurophilicity. The building block should be anionic (compared to the neutral dopdtc-based system above) so that cations can be utilized to tune the overall structural properties, and to increase the solubility of the products in polar solvents. In addition, the Au-based building block should contain softer donor ligands to increase the strength of aurophilic interactions and should not be so sterically hindered as that might not be suitable to form gold(I) chains.[87-89]

Considering all the given parameters above, a dithiolate building block which features the electron rich Au_2S_4 core from a bidentate dithiolate ligand was chosen; this

class of molecules, as noted above, has the requisite built–in intramolecular Au – Au interaction, is anionic, and under the right conditions can aggregate together to make *inter*-molecular aurophilic bond with other Au_2S_4 cores, creating infinite molecular gold(I) strings. Two known members of the bis(dithiolenegold(I)) family are maleonitriledithiolate ($[(CN)SC=CS(CN)]^{2-}$, $(mnt)^{2-}$) and its isomer *iso*-maleonitriledithiolate ($[S_2C=C(CN)_2]^{2-}$, $(i\text{-}mnt)^{2-}$) (Figure 1.12). Critically, these building blocks include sterically unhindered N-cyano groups at the periphery of the building block that could bind to other cationic groups (including metal centres) to form CPs. The small bite angles of these bridging bidentate ligands encourage formation of this intramolecular aurophilicity. With the right choice of cations, they can self-assemble into infinite 1-D gold(I) chains and generate higher-dimensionality systems (see below).[79,90-92] The Leznoff group has thus in particular focused on the gold(I) *iso*maleonitriledithiolate, $[Au_2(i\text{-}mnt)_2]^{2-}$ for these reasons.

In addition to their dynamic role in supramolecular structures, aurophilic interactions often give rise to highly emissive materials whose photoluminescent properties depend strongly on the geometry and extent (in particular, distances and angles) of the Au(I) – Au(I) contacts. The sensitivity of their luminescent properties to minor structural changes makes aurophilic interactions particularly suited to the design of materials that respond to external stimuli such as mechanical stress (mechanochromism), vapour (vapochromism), or temperature change.[93-96] Given these beneficial effects that are desirable toward designing stimuli-responsive materials, these aurophilic-based coordination polymer frameworks are a flexible “toolbox” and can be engineered accordingly. The focus of this research is to explore $[Au_2(i\text{-}mnt)_2]^{2-}$ as an anionic building block with a range of cations for aurophilic coordination polymers.

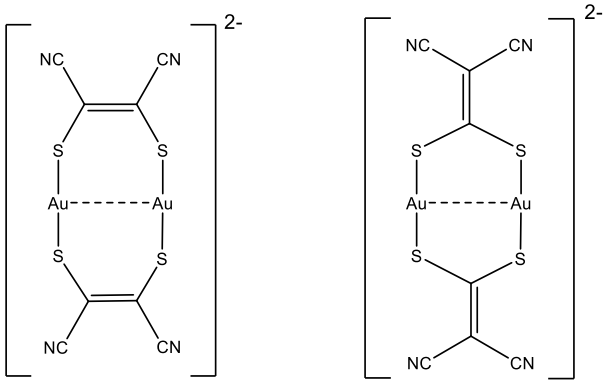

Figure 1.12: Structure of (left) $[Au_2(mnt)_2]^{2-}$ and (right) $[Au_2(i\text{-}mnt)_2]^{2-}$.

In this context, the $[Au_2(i\text{-mnt})_2]^{2-}$ framework is still underexploited, with very few examples reported in supramolecular chemistry in the past decades that explored $[Au_2(i\text{-mnt})_2]^{2-}$ as tunable aurophilic materials or their ability to make coordination polymers. $[Au_2(i\text{-mnt})_2]^{2-}$ was first reported by Fackler and co-workers in 1988 using $[n\text{-Bu}_4N]^+$ cations, and the structure of $[n\text{-Bu}_4N]_2[Au_2(i\text{-mnt})_2]$ features isolated $[Au_2(i\text{-mnt})_2]^{2-}$ anions without intermolecular aurophilic interactions, likely due to the steric hindrance effect of the large cations (Figure 2.1). Much later, in 2015, the Leznoff group showed that hydrogen bond containing cations, 3,5-dimethylpyrazolium and piperidinium, could be employed to reduce the Coulombic repulsion barrier between the $[Au_2(i\text{-mnt})_2]^{2-}$ anions, thus inducing interaurophilic interactions between them to yield infinite 1-D gold(I) chains of $[Au_2(i\text{-mnt})_2]^{2-}$ anions.[94] The emission drastically changed from green to red, consistent with the lower-emission energy requirements for 1-D gold(I) chains vs. isolated dimers. More recently, the Leznoff group also reported heterobimetallic systems using DMF-solvated Ln(III) cations with the $[Au_2(i\text{-mnt})_2]^{2-}$ building block, which also resulted in 1-D gold(I) chains.[98] Structurally, the Ln(III) cations were bound by DMF solvent rather than N-cyano groups from the $[Au_2(i\text{-mnt})_2]^{2-}$ and so these are not formally CPs, except for their 1-D chain network structure generated by aurophilic interactions. This work presented two vital considerations for designing aurophilic frameworks with $[Au_2(i\text{-mnt})_2]^{2-}$: the solvent systems used are important, and a strong interaction (e.g. hydrogen-bonding) between the cation and the N-cyano groups on the $[Au_2(i\text{-mnt})_2]^{2-}$anions are not necessarily required to facilitate intermolecular aurophilic interactions between anions.

In other unpublished work from the Leznoff group, salts containing short tetraalkylammonium R_4N^+ (where R = Me, Et, and n-Pr) cations with $[Au_2(i\text{-mnt})_2]^{2-}$ were prepared similarly to the synthesis of $[R_4N]_2[Au_2(i\text{-mnt})_2]$ in Chapter 2 and as according to the reaction equation in Figure 1.11. The crystal structures of these products indicated the presence of 1-D gold(I) chains. The supramolecular packing of these structures show cations wrapped around the 1-D gold(I) chain to create a columnar structure when observing down the 1-D gold(I) chains (Figure 1.13). The resemblance between $[R_4N]_2[Au_2(i\text{-mnt})_2]$ and some columnar structures that are present in the field of liquid crystal materials prompted us to ask ourselves: *Could we design emissive gold(I) coordination polymers with tunable luminescence, morphology and mechanical softness with a judicious choice of counter ion*?

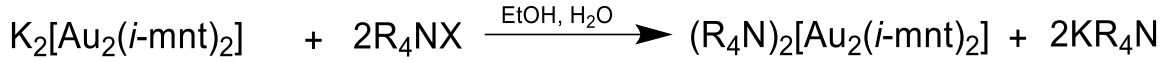

Figure 1.13: Reaction equation showing how $(R_4N)_2[Au_2(i\text{-mnt})_2]$ is prepared.

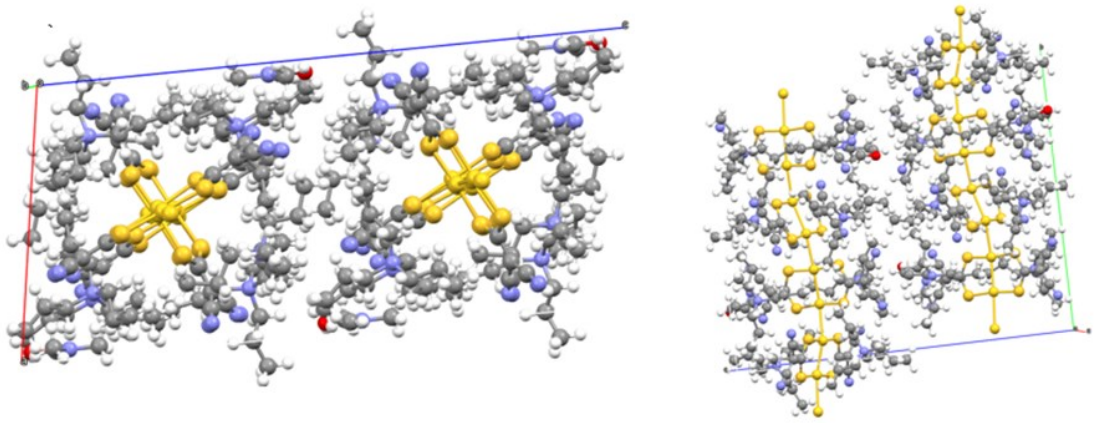

Figure 1.14: Crystals structure of $(Pr_4N)_2[Au_2(i\text{-mnt})_2]$ illustrates (right) formation of 1-D gold(I) chain, and (left) columnar supramolecular packing when looking down the gold(I) chain. Colour scheme: Au: yellow, N: blue, C: grey, H: white, S: orange.

1.4. Mechanical softness of materials and mechanochromism

Surfactants are molecules composed of both hydrophilic head groups and hydrophobic parts in the form of long alkyl chains, which can modify the surface properties of the liquid state and self-assemble into various patterned micellar or vesicular structures. These surfactants are classified as soft materials that function as systems that are tunable and can self-assemble in a controllable manner. Given the large structural sizes of these surfactants which are loosely packed, and held together by weak non-covalent interactions, they are generally deformable and responsive under the influence of external stimuli.

One particularly intriguing property among stimuli-responsive materials is mechanochromism, which is defined as a change in colour upon applying mechanical forces to the materials (i.e., pressure). If these materials also display luminescent properties in addition to mechanochromism, it can be defined as a mechanoresponsive luminescent material.[99] Upon mechanical stress, these crystalline materials undergo a phase transition in which the weak intermolecular interactions or molecular arrangement

in the crystal lattice are altered or destroyed.[100] Therefore, mechanoresponsive luminescent materials can have flexible luminescent profiles with unique emission colors after undergoing a structural change induced by pressure. This class of materials is dynamic and can be useful in a wide range of applications as sensors, memory storage, informational and security features.[101]

It is important to distinguish the concept of mechanical softness (i.e., physical hardness and softness of the materials) and the chemical softness of the atoms (i.e., hard soft acid base theory in relation to polarizability of chemical species). Mechanical softness and hardness of materials refers to the ability to undergo local deformation, induced mechanically by pressure or abrasion.[126] The hardness of a material can be quantified in described in several ways, including elasticity, stiffness, strain, toughness, etc.[126] Mechanical softness is important toward designing materials that are stimuli responsive. On the other hand, chemical softness refers to the polarizability of an acid or base. In particular, a larger, low-charge, polarizable metal or ligand is termed "soft", while a hard acid or base would typically have high charge density, be less polarizable, and smaller in size. A hard acid generally binds strongly and more favourably with a hard base, and similarly a soft acid prefers to interact with a soft base instead of hard base. This theory is used to predict if a metal and ligand interaction is favourable or not.

These dynamics in property and morphology of $[Au_2(i\text{-mnt})_2]^{2-}$ were seen through a diverse portfolio of cations. One strategy that can further mechanically soften the materials is to implement a known flexible cation such as a surfactant to this anionic building block, which could induce a potential phase transition upon change in pressure or temperature. In addition, surfactants are known to adopt various structures and play a critical role as a template that controls the size or shape of overall structures. This combination could open more methods to engineer and modify materials geared toward luminescence, mechanical softness, and generating different morphologies.

1.5. Thesis goal

My research objective is to utilize the readily emissive $[Au_2(i\text{-mnt})_2]^{2-}$ anion and combine it with soft surfactant $[RMe_3N]^+$ and its derivatives cations ($R = C_nH_{2n+1}$, n = 4, 6, 8, 10, 16) to further enhance the mechanical softness of materials that ideally would display both luminescent properties and could be responsive to external stimuli. Chapter 2 comprises

two parts: the first part examines tetraalkylammonium cations $[R_4N]^+$ with alkyl chains longer than the prototypical ^{n}Bu-unit, and the second part is to investigate how changing a single alkyl group chain length in the alkyltrimethylammonium cations $[RMe_3N]^+$, combining with $[Au_2(i\text{-mnt})_2]^{2-}$ could impact the supramolecular packing and emissive properties, particularly with the goal of preparing soft, stimuli responsive gold(I)-containing CP materials. The cations are all readily accessible, and the CTAB-containing cations in particular are related to common surfactants. The research will also address the question of how would long alkyl chains influence the photoluminescent and mechanical properties of any aurophilic materials.

1.6. Characterization Techniques for Gold(I)-based CP materials

The two properties of particular interest for the gold(I)-based materials herein are structure (from X-ray crystallography; see below) and the luminescent properties, which are obtained from measuring the absorption and emission spectra. The measurement of these optical properties includes two related techniques: (a) Ultraviolet-visible (UV-Vis) absorption spectroscopy and (b) a fluorometry experiment, using a fluorometer.

UV-visible Absorption and Reflectance Spectroscopy. UV-Vis spectroscopy is a method to obtain the light absorption spectra of the compound, which in general is carried out by passing incident photons of UV and visible light through a cell containing a solution of the compound of interest, and a detector measures the intensity of the light that was not absorbed, as a function of wavelength. The instrument is then measuring the light absorbed or transmitted at individual wavelength over the range of UV to visible light to give a UV absorption spectrum. The absorbance peak observed in the UV-Vis spectrum, which indicates wavelengths that the molecules can absorb, is then used as the excitation peak to measure emission spectra of potentially fluorescent materials. On the other hand, performing UV-visible absorption spectroscopy for solid-state materials is more challenging, and it is easier to measure the light that is reflected (i.e., not absorbed) from solid materials instead, using a reflectance spectrometer setup. In reflectance spectroscopy, a portion of light radiation is reflected on the upper interface of materials and another fraction of radiation penetrates through the sample, which can be absorbed or be reflected. The reflected radiation intensity from the sample is then collected as a function of wavelength to obtain the reflection spectrum, which is the inverse of the

absorption spectrum. Due to technical limitations, neither absorption nor reflectance spectra were collected for the solid samples described in this thesis.

Excitation and Emission Spectroscopy. Excitation and emission spectroscopy are part of a fluorometry experiment. The fluorometer consists of multiple parts: an excitation light source such as a Xenon arc lamp hooked up with an excitation monochromator to illuminate the material. Light that is emitted from the sample is then measured at 90° from the incident radiation to minimize its interference, and then passes through an emission monochromator to strike the detector; this geometry prevents both scattering and the exciting light from reaching the detector. An excitation wavelength is required to be specified when producing the emission spectrum, which specifies which wavelengths of light the sample produces upon excitation. Similarly, an emission wavelength that the fluorimeter needs to hold at while the excitation wavelength is swept through needs to be specified - this generates an excitation spectrum, which illustrates at what wavelengths the samples can absorb energy to produce its emission. Generally, for most fluorophores, the absorption and excitation spectra should overlap and have similar peaks. The absorption or reflectance spectra of solid-state materials that display luminescent behavior are often tricky to obtain due to emitted photons being part of the reflected light during excitation. A clear distinction that should be re-emphasized is that the UV-Vis absorption spectrum would show a spectrum of wavelengths that the fluorophore absorbs whereas an excitation spectrum displays the wavelength that the fluorophore would need to absorb to emit at that particular wavelength. While it is still viable to obtain absorbance spectra in this manner, another technique that we could utilize is to collect an excitation-emission matrix (EEMs).

Excitation-Emission Matrix. An excitation-emission matrix or excitation-emission map (EEM) is a built-in data collection and presentation feature of the fluorometer, which provides a 3D map of the excitation and emission wavelengths in two dimensions versus fluorescence intensity of the materials in the 3rd dimension. These matrices are obtained over a wide range scan of wavelengths by a series of synchronous emission and excitation scans with an increasing and fixed wavelengths offset. An example of a completed EEM map is shown in Figure 1.15, with the bright and intensive red – yellow colour (left y-axis; intensity counts) representing the most emissive regions on the x-axis (emission wavelength) and the corresponding excitation wavelength required to obtain it on the right y-axis. The most intensive emissive wavelength region, which is highlighted by a red

colour, is then chosen as the emission maximum to perform an excitation scan. Then, the resulting excitation maximum is used to perform an emission scan one more time to confirm if the emission maxima were correctly picked.

While EEMs are arguably a more convenient way to study solid-state fluorescence using a fluorometer, without the need for measuring UV-vis absorbance spectra (to find the ideal excitation wavelength), some limitations exist: EEMs are obtained by using a fluorometer, which is by default a fluorescence measurement, and will ignore or miss any absorbance and colour information for all non-fluorescent compounds. Another drawback is that many fluorometers use single channel scanning and take longer times to collect the entire EEM data set, thus dynamic structures that can undergo any structural change during acquisition are also not suitable for EMM measurement.

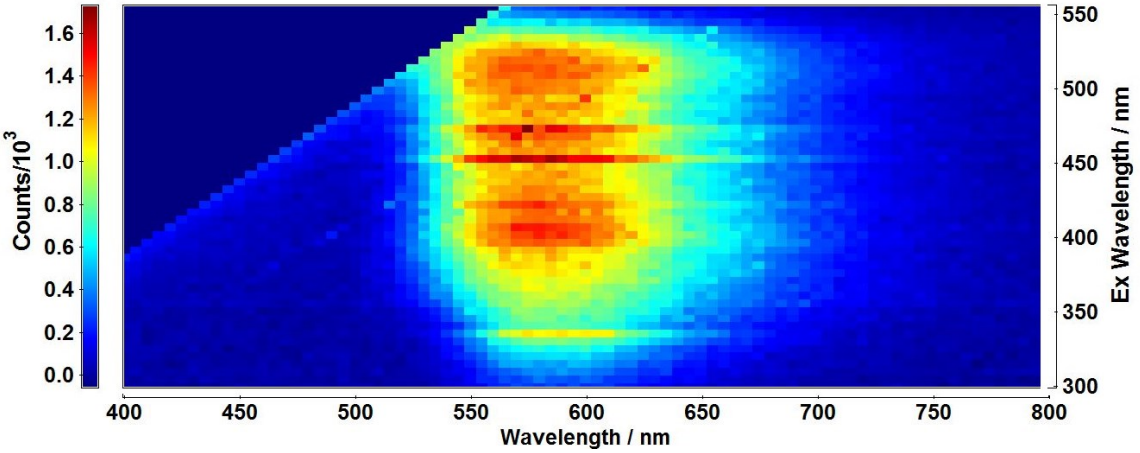

Figure 1.15: Example of a 2D Excitation-Emission Matrix (EEM) highlighting the emissive wavelength via bright, intensive red/yellow region. The blue region indicates the non-emissive wavelengths (where the counts are very low). The x-axis is the emission wavelengths whereas the y-axis on the right represents the excitation wavelength, while the y-axis on the left represents the emissive intensity of the samples at each excitation/emission pair in two dimensions.

Fluorescence Quantum Yield. Quantum yield (Φ) measures the efficiency of emissive materials at a given wavelength, which is defined as the number of photons emitted divided by the number of photons absorbed by the materials; a perfect efficiency would thus be 1.0 (or 100%). The method to carry out quantum yield measurement in this work involves using an integrating sphere sample module, which is a hollow spherical attachment to the fluorimeter that allows maximum light reflection and captures all of the light emitted from the sample. The procedure for calculating the quantum yield using the

integrating sphere included three different steps: reference, indirect, and direct measurement.[102,103]

Infrared, Raman spectroscopy, Elemental Analysis, and Single Crystal X-Ray Diffraction. These are a common set of techniques utilized to analyze and characterize solid-state coordination polymers, and to give insight into the structural composition and purity. Non-destructive techniques like IR and Raman spectroscopy are crucial to solid-state materials by confirming the presence of key functional groups. For example, cyanometallate-based CPs such as dicyanoaurate, $[Au(CN)_2]^-$, contain an important stretching mode $\nu_{C\equiv N}$, the energy of which can be utilized to determine if the N-terminus is bound to another atom or not. In this thesis, focusing on $[Au_2(i\text{-mnt})_2]^{2-}$, IR and Raman spectroscopy are not as instructive since the materials prepared herein do not generally have components that bind to the N-cyano termini, but IR and Raman spectroscopy are still useful to check for the presence of unexpected impurities or bound solvents.

Elemental analysis (EA) is another quantitative tool to analyze the chemical composition and purity of solid materials. The analytical method, also termed combustion analysis, fully burns the material including carbon, hydrogen, nitrogen, and sulfur (CHNS) into their respective gaseous oxide forms of CO_2, H_2O, NO_x, and SO_x, which get passed through gas chromatographic analysis to determine the percentage of CHNS elements in the materials. This information can be used to confirm stoichiometric ratios of components (e.g. metal:ligand:cation) in the final material.

One of the most vital techniques in the CP field is X-Ray diffraction (XRD), notably single crystal X-Ray diffraction (SC-XRD). While the prerequisite to any SC-XRD experiment is to have a high-quality single crystal through crystal-growth, it is one of the most powerful techniques to determine the solid-state structure of CPs. Powder X-ray diffraction (PXRD) is also another useful characterization tool to provide more evidence about the phase transition, purity, and to compare with other similar structures.[104] This thesis relies heavily on both single-crystal and powder X-ray diffraction data to determine solid-state supramolecular structures of the key materials herein. A detailed discussion of the theoretical background behind X-ray diffraction is beyond the scope of this thesis.[105]

Thermal properties. To study the thermal stability/decomposition profile and whether or not a phase transition as a function of temperature might occur with the gold(I)

CPs herein, thermogravimetric analysis (TGA) and differential scanning calorimetry (DSC) can be used. TGA is primarily employed to investigate the thermal stability of materials, and it shows mass losses as a function of temperature, thereby determining decomposition temperatures in general. DSC can detect phase transitions of materials as a function of temperature.

Chapter 2. Designing Tunable Photoluminescence and Stimuli-Responsive Coordination Polymers using Gold(I) *iso*-maleonitriledithiolate as an anionic Building Block

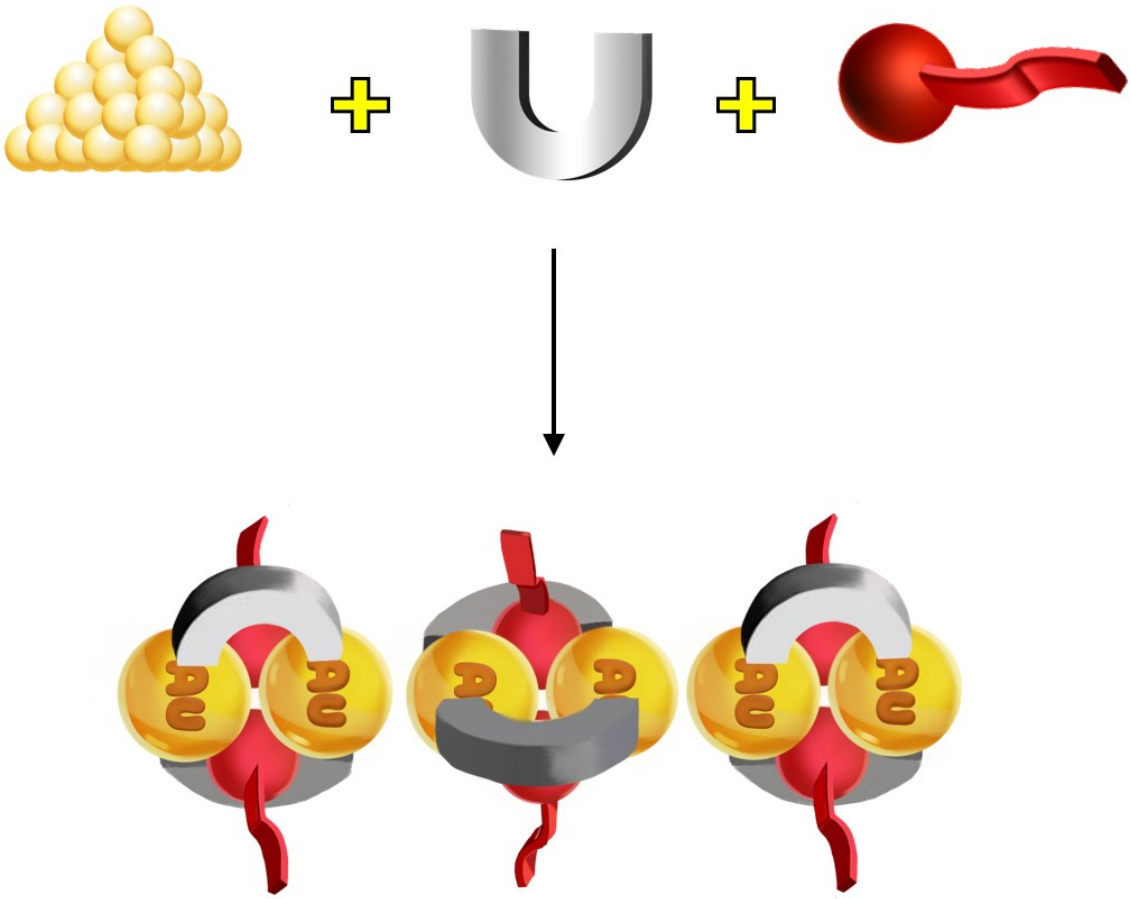

2.1. Synthesis and Photoluminescent Properties of $[(C_nH_{2n+1})_4N]_2[Au_2(i\text{-mnt})_2]$

2.1.1. Introduction

As outlined in the introduction chapter, the non-covalent aurophilic interaction can be exploited for designing tunable photoluminescent materials and control the overall dimensionality of supramolecular structures in coordination polymers. While the photoluminescent properties derived from aurophilic interactions are not guaranteed to be observed, a fully ligand-supported anionic bidentate dithiolate coordination framework with an intramolecular aurophilic bond, in this case $[Au_2(i\text{-mnt})_2]^{2-}$ is postulated to favour the observation of emission properties, given its inherent aurophilic bond. Thus, Chapter 2 concentrates on exploring tuning the supramolecular arrangement of $[Au_2(i\text{-mnt})_2]^{2-}$ by employing long alkyl chain ammonium cations and exploring the stimuli-responsiveness of the resulting materials via testing their mechanochromic properties. We will first discuss the large tetraalkylammonium units, $[(C_nH_{2n+1})_4N]^+$, as cations for $[Au_2(i\text{-mnt})_2]^{2-}$ and whether these cations can induce intermolecular aurophilic interactions. A great emphasis will be placed on the latter portion of the chapter, which focuses on the less bulky alkyl trimethylammonium cations $[RMe_3N]^+$ (R = C_nH_{2n+1}, n = 4, 6, 8, 10, 16) that could allow intermolecular aurophilicity between anions to form 1-D aurophilic chains with flexible emission profiles as the alkyl chain is changed.

Previous work on the tetraalkylammonium cations with $[Au_2(i\text{-mnt})_2]^{2-}$ showed that the crystal structure of $[n\text{-Bu}_4N]_2[Au_2(i\text{-mnt})_2]$ was seen as isolated Au(I) dimers with no intermolecular aurophilic interaction. This was hypothesized as due to the large steric bulk of the tetrabutylammonium ($[n\text{-Bu}_4N]^+$) cations that prevents the formation of inter-molecular aurophilic interactions between the anions (Figure 2.1). In contrast, using the appropriate cations, for example smaller cations that allow the intermolecular Au(I) – Au(I) interaction between anions to form could consequently promote formation of infinite 1-D gold(I) chains (Figure 2.2).

The $[n\text{-Bu}_4N]_2[Au_2(i\text{-mnt})_2]$ complex was reported to have a distinct green emission maximum at λ_{max} = 515 nm, which is typical for isolated gold(I) dimers.[94,106] Related unpublished work in the Leznoff group using smaller alkyl chain lengths (e.g. $Propyl_4N^+$, Me_4N^+) in tetraalkylammonium cations with the $[Au_2(i\text{-mnt})_2]^{2-}$ unit, found that these

structures were able to form infinite 1D gold(I) chains with emission maxima that are substantially red-shifted from the green wavelength. While these results adhered to the hypothesis that smaller cations do not interrupt the inter-molecular aurophilic interaction between anions and the emission profile is no longer green, we wanted to further explore this idea by testing whether with bulkier tetraalkylammonium cations to pair with $[Au_2(i\text{-}mnt)_2]^{2-}$ could produce similar results as the structure of $[n\text{-}Bu_4N]_2[Au_2(i\text{-}mnt)_2]$ and to explore any phase transition these materials could have in response to temperature.

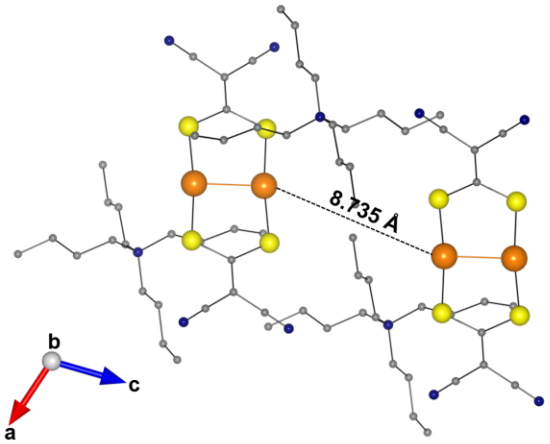

Figure 2.1: Crystal structure of $[n\text{-}Bu_4N]_2[Au_2(i\text{-}mnt)_2]$ illustrates the separation of $[Au_2(i\text{-}mnt)_2]^{2-}$ anion units and bulky $[n\text{-}Bu_4N]^+$ cations, or isolated gold(I) dimers. Colour scheme: Au, orange; S, yellow; N, blue; C, grey. Hydrogen atoms are omitted for clarity.[106]

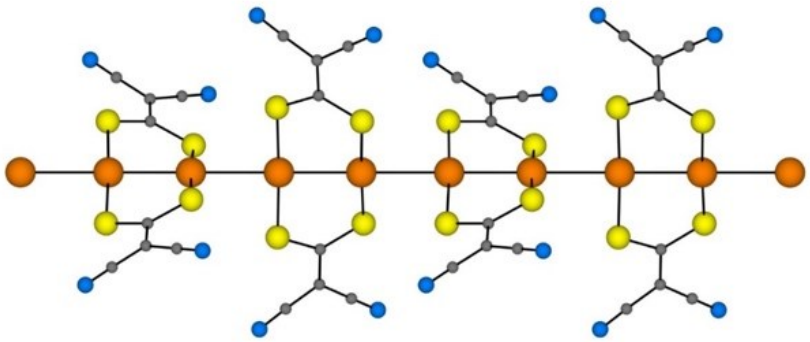

Figure 2.2: Crystal structure (unpublished Leznoff group work) illustrating how the appropriate cations could induce inter-molecular aurophilic interaction between $[Au_2(i\text{-}mnt)_2]^{2-}$ anion units, thus the formation of infinite 1D gold(I) chains is observed. Colour scheme*:* Au, orange*;* S, yellow*;* N, blue*;* C, grey. Hydrogens and $[Propyl_4N]^+$ cations are omitted for clarity. Synthesis and structure by Jeffery Cheung and Jefferson Pells.

2.1.2. Synthesis and Structures of $[R_4N]_2[Au_2(i\text{-mnt})_2]$ Complexes

The synthesis of the $[R_4N]_2[Au_2(i\text{-mnt})_2]$ salts was performed as follows: combine 1 equivalent of $K_2[Au_2(i\text{-mnt})_2]$ to 2 equivalents of $[(C_nH_{2n+1})_4N]X$ (X = Br, I; n = 5, 7, 8, i.e., linear alkyl chains) in a mixture of 1:1 EtOH:H_2O.

$$K_2[Au_2(i\text{-mnt})_2] + 2R_4NX \xrightarrow{\text{EtOH, acetone}} [R_4N]_2[Au_2(i\text{-mnt})_2] + 2KX$$

A dark red oily bubble appeared on the surface of the mixture after combining. Further stirring resulted in the formation of an orange solid, which was collected via vacuum filtration, washed multiple times to remove KX, and dried overnight to yield a bright orange powder of $[R_4N]_2[Au_2(i\text{-mnt})_2]$, which then was analyzed by the typical characterization methods of CPs (e.g. %CHNS elemental analysis, IR spectroscopy). Infrared spectra spectroscopy showed a common ν(C≡N) energy between 2190-2195 cm^{-1}, which is consistent with the presence of terminal nitrile groups. It is expected that there should be no interaction between cations or solvents with this terminal nitrile group, thus it is unsurprising that the ν(C≡N) should be similar across the series. These materials are slightly soluble in some fairly polar solvents including ethyl acetate and chloroform, and in non-polar toluene, and are highly soluble in dimethyl sulfoxide (DMSO) and dimethylformamide (DMF). The orange powdered materials were then used for crystal growth attempts with various methods including vapor diffusion (e.g., dissolve the materials in DMF and let MeOH, EtOH, *i*-PrOH, acetone, or acetonitrile diffuse inside), slow evaporation, and layered diffusion, yet these materials did not crystallize well and generally yielded poor quality crystals or microcrystalline powders, none of which were suitable for SC-XRD analysis.

In one specific case, while efforts were made toward synthesizing and crystallizing the $[(C_6H_{13})_4N]_2[Au_2(i\text{-mnt})_2]$ material, this compound was not completely purified and contained some traces of a black solid at the bottom of the crystallization vials, which was postulated to be evidence of a disproportionation reaction of gold(I) into Au(0) and Au(III). The structure of the gold(III) complex formed and isolated during crystal growth, namely $[(C_6H_{13})_4N][Au^{III}(i\text{-mnt})_2]$, was revealed via SC-XRD. The crystal structure features isolated gold(III) anions with the closest Au – Au distance of 10.603 Å, and with $[(C_6H_{13})_4N]^+$ cations tiling between the isolated anions (Figure 2.3).

Although no crystal structures of Au(I) derivatives of $[R_4N]_2[Au_2(i\text{-mnt})_2]$ could be obtained due to the low-quality crystals obtained from crystal growth, a comparison of their photoluminescent spectra is another method to distinguish whether these materials contain isolated gold(I) dimers or infinite 1D gold(I) chains. Isolated gold(I) dimers were expected to emit a green colour similar to $[n\text{-}Bu_4N]_2[Au_2(i\text{-mnt})_2]$, as discussed above.

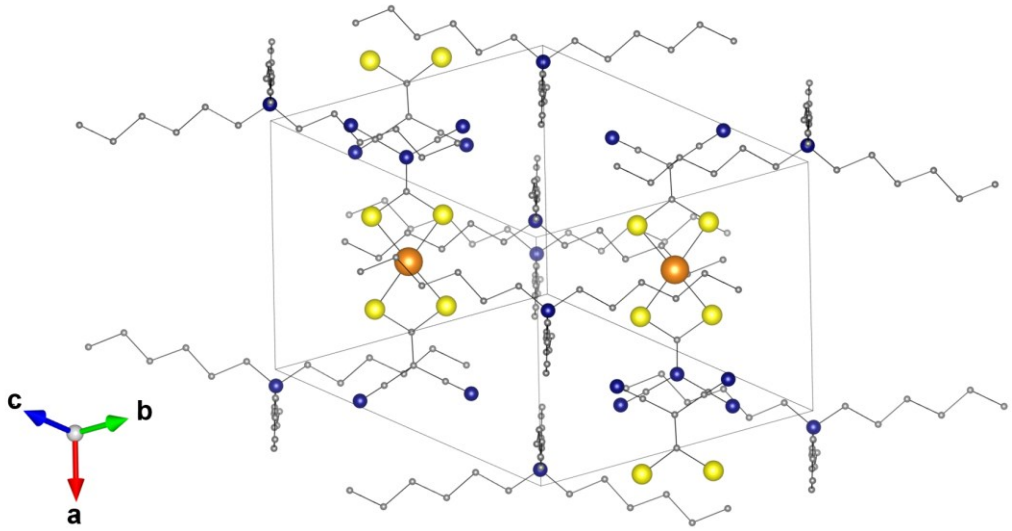

Figure 2.3: Crystal structure of $[(C_6H_{13})_4N][Au^{III}(i\text{-mnt})_2]$ illustrates an isolated gold(III) anion resulting from the disproportionation reaction of $[(C_6H_{13})_4N]_2[Au_2(i\text{-mnt})_2]$. Colour scheme: Au, orange; S, yellow; N, blue; C, grey. Au^{III}–S = 2.329(3) – 2.343(4) Å, terminal C–N = 1.13(2) – 1.141(18) Å, C=C = 1.359(16) –1.386(15) Å. Hydrogen atoms are omitted for clarity.

2.1.3. Photoluminescence properties of $[(C_nH_{2n+1})_4N]_2[Au_2(i\text{-mnt})_2]$

The photoluminescent properties of these salts were investigated by first obtaining their excitation-emission matrix spectrum. In general, the EMM spectra of these materials illustrate that the emissive regions are located approximately at 525 nm (Figure 2.4). The excitation spectra were collected by monitoring emission at 525 nm, yielding excitation maxima (λ_{max}) between 450-480 nm; the resulting excitation maxima were then used to obtain emission spectra.

The luminescence spectra indicated that these compounds all emit green light, thus suggesting that these structures are likely in the form of isolated gold(I) dimers and do not form 1-D gold(I) chains (Figure 2.5). Some emission spectra produced a sharp and noticeable shoulder peak at 580 and 590 nm, which potentially corresponds to an

instrumental artifact. The excitation and emission λ_{max} of each structure is summarized in Table 2.1, which highlights the similar green emission across the systems. Interestingly, the $[(C_7H_{15})_4N]_2[Au_2(i\text{-mnt})_2]$ material showed particularly bright emission among the tetraalkylammonium series (Φ = 10%) and possessed the closest emission at λ_{max} = 520 nm to the reference compound $[n\text{-}Bu_4N]_2[Au_2(i\text{-mnt})_2]$, which has an emission λ_{max} = 515 nm. The emission spectra of the other two compounds, $[(C_5H_{11})_4N]_2[Au_2(i\text{-mnt})_2]$ and $[(C_8H_{17})_4N]_2[Au_2(i\text{-mnt})_2]$, also exhibited similar green emissions at λ_{max} = 532 nm and 530 nm, respectively, although the $[(C_5H_{11})_4N]^+$ system shows a potential impurity of $K_2[Au_2(i\text{-mnt})_2]$ that emits at 625 nm (Figure 2.8). These observations further confirmed that bulkier tetraalkylammonium cations, when pairing with $[Au_2(i\text{-mnt})_2]^{2-}$ do not support intermolecular aurophilic interactions between anions and form isolated gold(I) dimers instead.

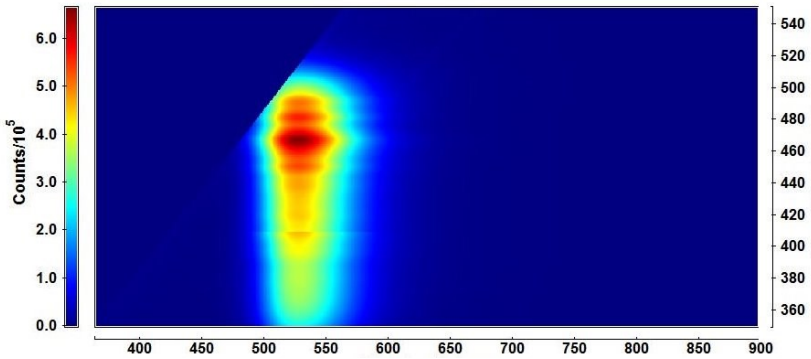

Figure 2.4: EEM spectrum of the $[(C_7H_{15})_4N]_2[Au_2(i\text{-mnt})_2]$ structure illustrates the emissive region at ca. 525 nm.

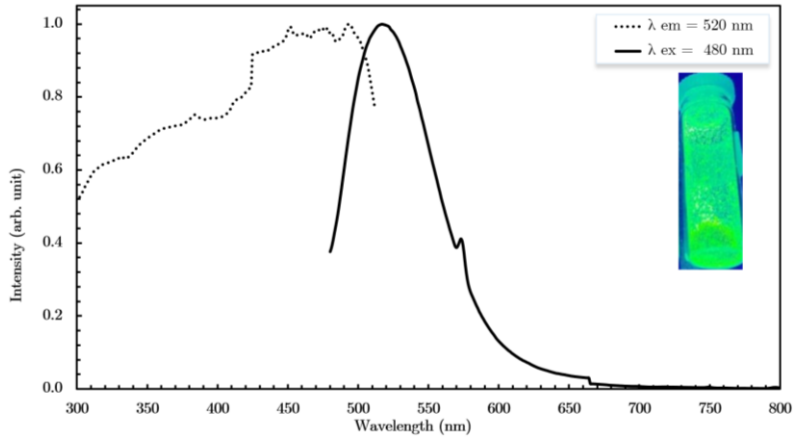

Figure 2.5: Excitation (dotted line) and emission (solid line) spectra of $[(C_7H_{15})_4N]_2[Au_2(i\text{-mnt})_2]$. The sharp peak at ca. 580 nm is an instrumental artifact. The inset is a photo of the green-emitting solid material on a UV-light table.

Table 2.1: Summary of luminescence wavelengths (nm) of $[(C_nH_{2n+1})_4N]_2[Au_2(i\text{-mnt})_2]$ and the reference compound $[(n\text{-}Bu_4N)]_2[Au_2(i\text{-mnt})_2]$ at room temperature.

$[R_4N]^+$	$[n\text{-}Bu_4N]^+$	$[(C_5H_{11})_4N]^+$	$[(C_7H_{15})_4N]^+$	$[(C_8H_{17})_4N]^+$
Excitation max (nm)	420	450	480	485
Emission max (nm)	515	532	520	535

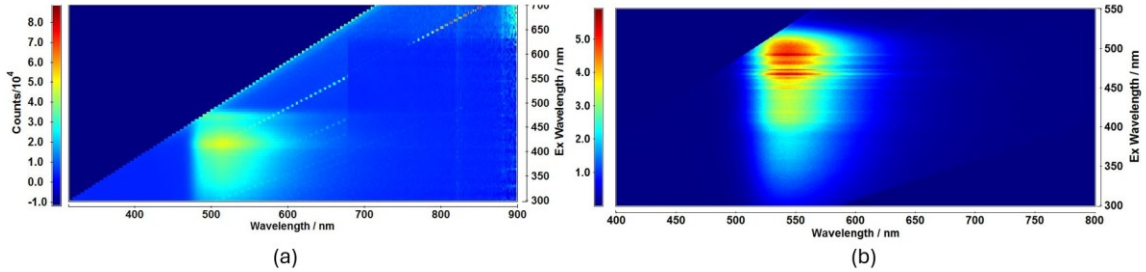

Figure 2.6: EEM spectra of (a) $[(C_5H_{11})_4N]_2[Au_2(i\text{-mnt})_2]$ and (b) $[(C_8H_{17})_4N]_2[Au_2(i\text{-mnt})_2]$ illustrates emissive region at ca. 530 nm.

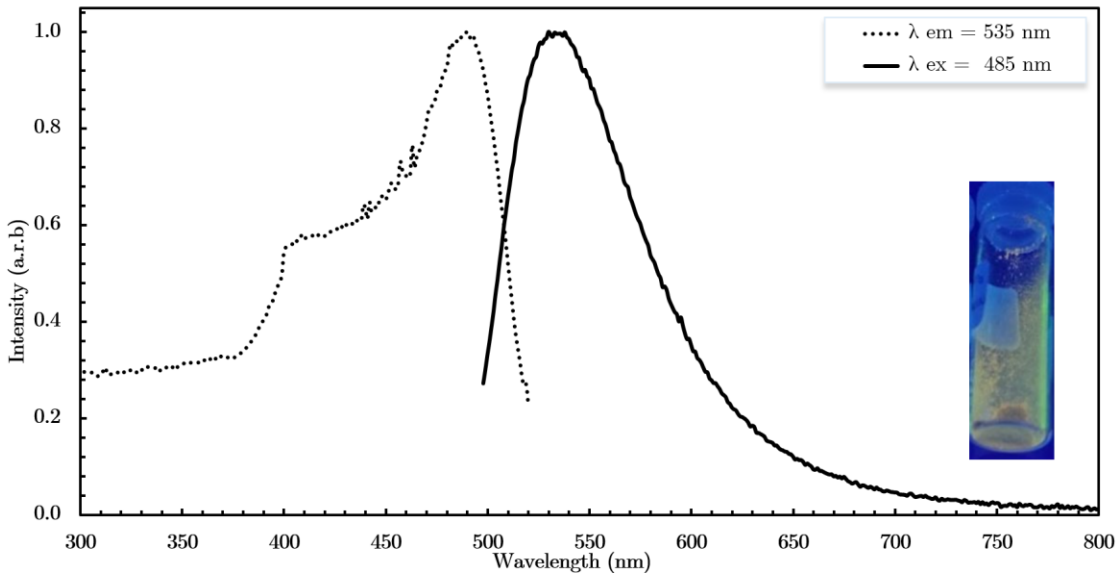

Figure 2.7: Excitation (dotted line) and emission (solid line) spectra of $[(C_8H_{17})_4N]_2[Au_2(i\text{-mnt})_2]$. The inset is a photo of the emitting material on a UV-light table.

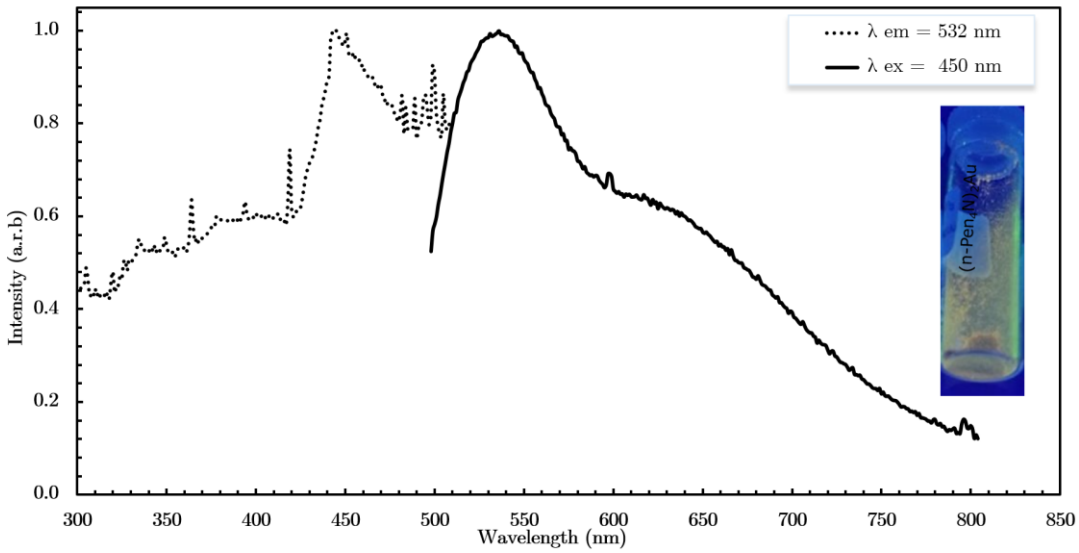

Figure 2.8: Excitation (dotted line) and emission (solid line) spectra of $[(C_5H_{11})_4N]_2[Au_2(i\text{-mnt})_2]$. The peak at 625 nm is attributed to some remaining $K_2[Au_2(i\text{-mnt})_2]$ starting material. The inset is a photo of the emitting material on a UV-light table.

2.1.4. Thermal Properties of $[(C_nH_{2n+1})_4N]_2[Au_2(i\text{-mnt})_2]$

The phase behaviour of one of these compounds was investigated by differential scanning calorimetry (DSC) and optical microscopy, performed on the $[(C_7H_{15})_4N]_2[Au_2(i\text{-mnt})_2]$ salt. When heated to 150 °C, some black traces started to appear on the orange solid, and the sample completely converted into black solid at 170 °C. DSC and optical microscopy showed no obvious phase transition. The fact that the material turned black when heated could be consistent with a potential disproportionation reaction that occurred, or simply decomposition of the material, although the TGA suggests mass losses only at higher temperatures. Indeed, the thermogravimetric analysis (TGA) of both $[n\text{-}Bu_4N]_2[Au_2(i\text{-mnt})_2]$ (Figure 2.9) and $[(C_7H_{15})_4N]_2[Au_2(i\text{-mnt})_2]$ (Figure 2.10) show many similarities, particularly a common significant mass drop past 210 °C, which indicates decomposition of the materials at this higher temperature; note that this temperature of mass loss is higher than the temperature at which the material turns black (i.e., without an accompanying mass loss). Mass loss takes place in stepwise manner, with distinct events observed at 210°C (calculated as 48% sudden mass loss, and another 12%) and 500 °C (calculated as 13% mass loss); a similar degradation pattern is observed for $[(C_7H_{15})_4N]_2[Au_2(i\text{-mnt})_2]$.

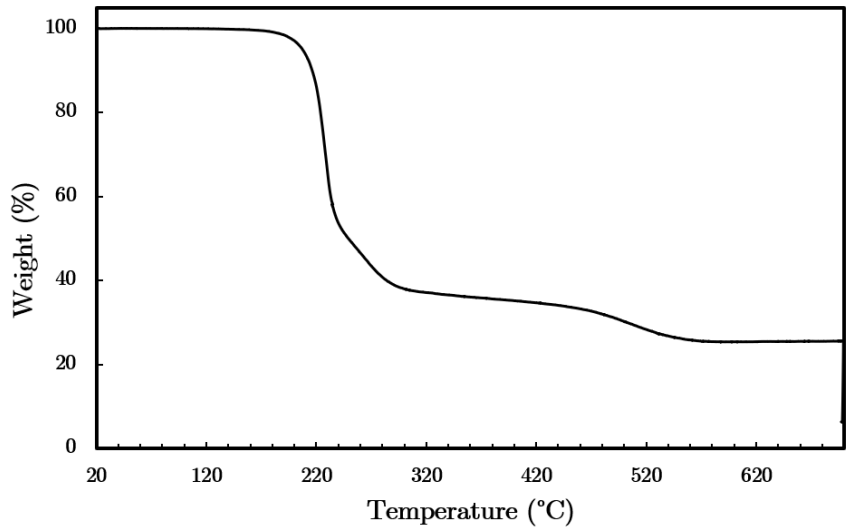

Figure 2.9: Thermogravimetric analysis curve of $[n\text{-}Bu_4N]_2[Au_2(i\text{-}mnt)_2]$ with mass loss occurring around 210 °C.

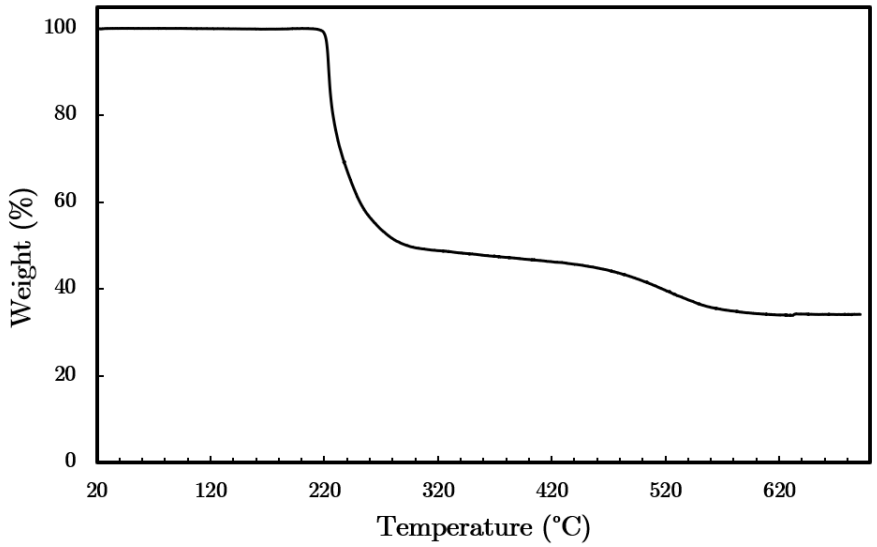

Figure 2.10: Thermogravimetric analysis curve of $[(C_7H_{15})_4N]_2[Au_2(i\text{-}mnt)_2]$ with mass loss occurring around 230 °C.

2.2. Synthesis and Characterization of $[RMe_3N]_2[Au_2(i\text{-}mnt)_2]$

2.2.1. Introduction

The aim of switching from tetraalkylammonium to alkyl-trimethylammonium cations was to reduce the steric hindrance that disrupts the formation of aurophilic interactions that facilitate the formation of infinite 1D gold(I) chains between the anions. These amphiphilic alkyl-trimethylammonium salts, particularly the cetyl trimethylammonium bromide (CTAB), are widely known to adopt distinctive supramolecular arrangements in both the solid state and lyotropic liquid crystal phases as the alkyl chain length is varied.[117-121] CTAB is commonly used as a tool to assist structural self-assembly of various compounds. We speculated that by tuning alkyl chain length on these organic cations could guide the self-assembly of the $[Au_2(i\text{-}mnt)_2]^{2-}$ units into different supramolecular packing motifs without disrupting the aurophilic chain and increasing the alkyl chain length could provide the necessary flexibility for generating softer materials. Cations $[RMe_3N]^+$ with an even number of carbons ($R = C_nH_{2n+1}$, n = 4, 6, 8, 10, 16) on the alkyl chain were investigated, as they are cheaply commercially available.

2.2.2. Synthesis and Structures of $[RMe_3N]_2[Au_2(i\text{-}mnt)_2]$

The targeted salts $[RMe_3N]_2[Au_2(i\text{-}mnt)_2]$ (RMe_3N = butyltrimethylammonium $[C_4Me_3N]^+$, hexyltrimethylammonium $[C_6Me_3N]^+$, octyltrimethyl ammonium $[C_8Me_3N]^+$, decyltrimethylammonium $[C_{10}Me_3N]^+$, and cetyltrimethylammonium $[C_{16}Me_3N]^+$) were synthesized by cation metathesis. Two equivalents of $RNMe_3X$ (X = Cl or Br) were added to an orange solution of $K_2[Au_2(i\text{-}mnt)_2]$, resulting in dark orange $[C_6Me_3N]_2[Au_2(i\text{-}mnt)_2]$, $[C_8Me_3N]_2[Au_2(i\text{-}mnt)_2]$ and $[C_{10}Me_3N]_2[Au_2(i\text{-}mnt)_2]$, or light orange $[C_4Me_3N]_2[Au_2(i\text{-}mnt)_2]$, or green $[C_{16}Me_3N]_2[Au_2(i\text{-}mnt)_2]$ powders. These materials in general are not soluble in water or non-polar solvents, are highly soluble in DMSO, DMF, and are moderately soluble in MeCN, CH_2Cl_2 and chloroform.

$$K_2[Au_2(i\text{-}mnt)_2] + 2RMe_3NX \xrightarrow{\text{EtOH, acetone}} [RMe_3N]_2[Au_2(i\text{-}mnt)_2] + 2KX$$

Finding the right combination of solvent systems and crystal growth techniques that yielded suitable single crystals for X-Ray diffraction was challenging. Slow evaporation and vapour diffusion in a 5-dram vial were the two techniques for crystals

growth in this series that were found to be most successful. In addition, the amount of materials used for crystal growth could sometimes influence the texture of crystals; too much could lead to fiber-like textures and too little could yield low-quality crystals. Attempts toward growing suitable crystals of the $[C_6Me_3N]^+$, $[C_{12}Me_3N]^+$ and $[C_{14}Me_3N]_2[Au_2(i\text{-mnt})_2]$ analogues were unsuccessful, resulting in typically long needle-shaped crystals that showed evidence of twinning and were generally low-quality and not suitable for collection of SC-XRD data. Among these, the $[C_6Me_3N]_2[Au_2(i\text{-mnt})_2]$ crystal structure resolved better than the other two, but the hexyl chains display multiple positionally disordered and could not be modeled properly, and the low-quality of the structural data limited its use for any structure-property correlations and thus was not included herein.

Similar to $[(C_7H_{15})_4N]_2[Au_2(i\text{-mnt})_2]$, when heated to around 150°C, crystals of $[RMe_3N]_2[Au_2(i\text{-mnt})_2]$ started to crack and change morphology, as observed by optical microscopy for R = C_4, C_{10} and C_{16}; further heating changed the materials to completely black at approximately 160°C. TGA data of the representative sample $[C_{16}Me_3N]_2[Au_2(i\text{-mnt})_2]$ indicated ca. 25% mass loss at ca. 210°C, which is consistent with loss of the *i*-mnt ligand (calculated as a 23% loss); further heating resulted in decomposition/loss of $[C_{16}Me_3N]^+$ (Figure 2.11), although a detailed decomposition pathway and identification of the volatile products was not attempted. No phase transitions were detected for any of the $[RMe_3N]_2[Au_2(i\text{-mnt})_2]$ materials, and these materials started to change colour after ca. 150°C.

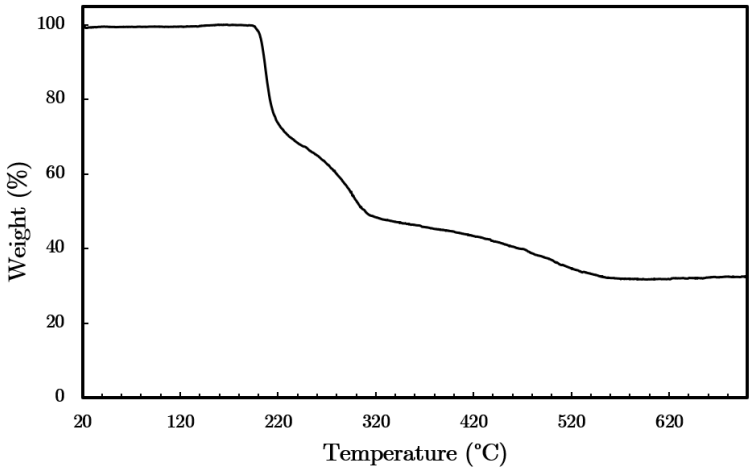

Figure 2.11: Thermogravimetric analysis of $[C_{16}Me_3N]_2[Au_2(i\text{-mnt})_2]$.

No substantial differences in the v(C≡N) peak was observed in the IR spectra of these salts; they all lie within the range of 2193 – 2198 cm^{-1}, which suggests that there is no presence of any interaction to the N-terminus in the gold(I) anion.

During the process of crystal growth, it was noted that occasionally a small yet noticeable amount of black solid, which we speculated was gold(0) based on the near-zero values of %CHNS from elemental analysis, appeared at the bottom of the crystallization vials, similar to observations in the $[(C_nH_{2n+1})_4N]_2[Au_2(i\text{-mnt})_2]$ series. Formation of this byproduct is believed to arise from either photo-induced or thermal oxidation during the crystal growth process to yield both gold(0), and gold(III)-containing structures of the form $[RMe_3N]_2[Au^{III}(i\text{-mnt})_2]$. Some of these $[RMe_3N]_2[Au^{III}(i\text{-mnt})_2]$ salts, including $[C_4Me_3N][Au^{III}(i\text{-mnt})_2]$, $[C_8Me_3N][Au^{III}(i\text{-mnt})_2]$, and $[C_{12}Me_3N][Au^{III}(i\text{-mnt})_2]$ were isolated and structurally determined by SC-XRD (Figure 2.12); the C_4Me_3 and C_8Me_3 versions are extremely poor-quality structures and are not included herein but their identity as Au(III)-based salts is clear. This oxidation event was not examined further, as it falls outside the scope of the current project. It is advised to cover or keep vials in the dark to minimize the $[RMe_3N]_2[Au^{III}(i\text{-mnt})_2]$ salts from forming.

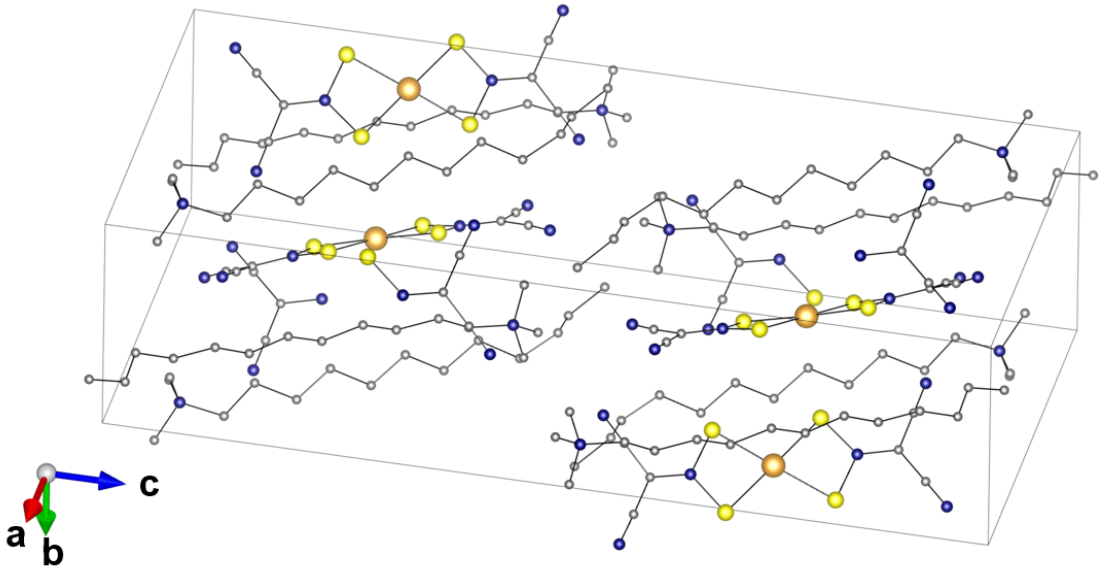

Figure 2.12: Crystal structure of representative gold(III) analog $[C_{12}Me_3N][Au^{III}(i\text{-mnt})_2]$ showing isolated gold(III)-containing anions with no presence of any aurophilicity. Colour scheme: Au, orange; S, yellow; C, grey; N, blue.

All of the reported solid-state structures of $[RMe_3N]_2[Au_2(i\text{-mnt})_2]$ in this chapter display aggregation between $[Au_2(i\text{-mnt})_2]^{2-}$ units, forming infinite 1-D aurophilic chains

with varying intermolecular Au(2) – Au(1)' distances of 2.8845(9) – 3.0095(7) Å and intramolecular Au(1) – Au(2) distances of 2.7827(9) – 2.8170(7) Å. In addition, these structures show the trimethyl headgroup of the $[RMe_3N]^+$ cation oriented near the $[Au_2(i\text{-}mnt)_2]^{2-}$ anion. As postulated, the shape of the cation strongly impacted the supramolecular arrangement of the 1-D chains; the conformation of the $[Au_2(i\text{-}mnt)_2]^{2-}$units both within the dimer and relative to each other along the anionic chain also varies depending on the incorporated cation. Each system is described in detail below.

For $[C_4Me_3N]_2[Au_2(i\text{-}mnt)_2]$, two structures were obtained: a solvent-included and a solvent-free system. The solvent-included structure has the same space group and similar unit cell parameters and aurophilic interactions compared to the solvent-free structure. Specifically, the crystal structure of the solvent-free $[C_4Me_3N]_2[Au_2(i\text{-}mnt)_2]$ system, obtained from the slow evaporation of a toluene and acetonitrile mixture, contains dinuclear $[Au_2(i\text{-}mnt)_2]^{2-}$ moieties with an intramolecular Au(I) – Au(I) distance of 2.8170(7) Å; the Au_2S_4 core adopts a highly twisted conformation, quantified by the C1–S1–S2–C2 and C1–S3–S4–C2 dihedral angles of 53.2(8)° and 44.4(8)°. Adjacent $[Au_2(i\text{-}mnt)_2]^{2-}$ units are orthogonal, forming a continuous 1-D aurophilic chain via an intermolecular Au(I) – Au(I) bond of 3.0095(7) Å (Figure 2.13a). The trimethyl headgroups of both $[C_4Me_3N]^+$ cations are positioned near the central Au(I) atoms while the butyl chain is oriented perpendicular to the 1-D gold(I) chain (Figure 2.13b). Moreover, the butyl chains on $[C_4Me_3N]^+$ that are located near each $[Au_2(i\text{-}mnt)_2]^{2-}$ unit are rotated by roughly 90° to its adjacent neighbour, while remaining perpendicular to the gold(I) chain. Viewing along the *c*-axis, the $[C_4Me_3N]^+$ cations surround the isolated 1-D aurophilic chains in a pseudo-hexagonal packing motif (Figure 2.14).

When $[C_4Me_3N]_2[Au_2(i\text{-}mnt)_2]$ was crystallized from vapour diffusion of methanol (MeOH) into an acetonitrile solution, the MeCN-solvated $[C_4Me_3N]_2[Au_2(i\text{-}mnt)_2]\cdot MeCN$ system was isolated; it is isomorphic to $[C_4Me_3N]_2[Au_2(i\text{-}mnt)_2]$, with one interstitial MeCN molecule that fills in the cavity between the columnar gold(I) chains. The aurophilic interactions remain similar to the non-solvated form (Figure 2.15). The intramolecular and intermolecular Au(I) – Au(I) distances are measured at 2.7992(7) and 2.9700(7) Å respectively; the Au_2S_4 core has C1–S1–S2–C2 and C1–S3–S4–C2 dihedral angles of 53.8(8)° and 47.2(8)° (Appendix A).

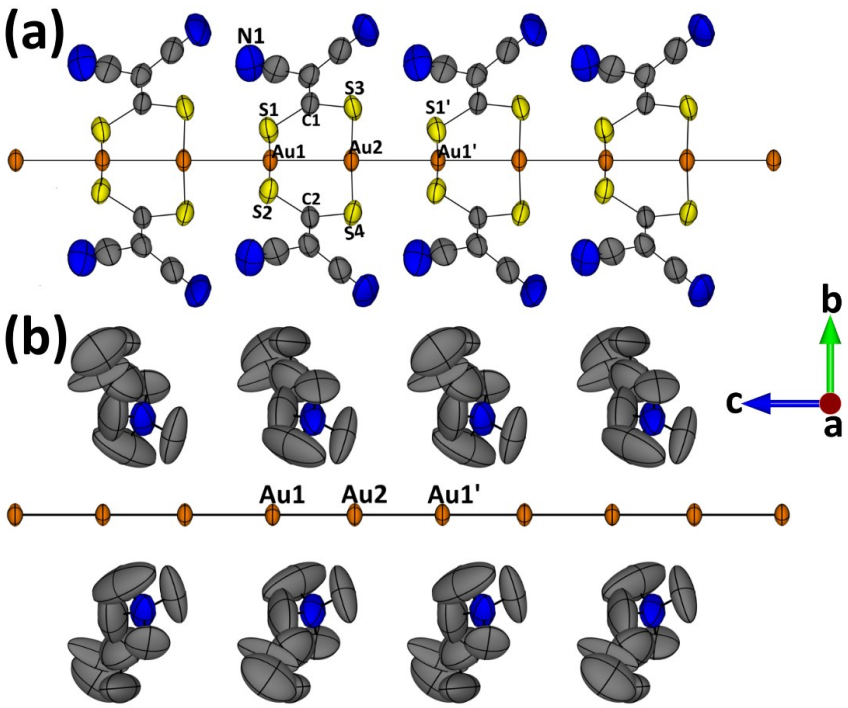

Figure 2.13: (a) Crystal structure illustrating the 1-D aurophilic chain in $[C_4Me_3N]_2[Au_2(i\text{-}mnt)_2]$. $[C_4Me_3N]^+$ cations are omitted for clarity. Au1–Au2 = 2.8170(7) Å, Au2–Au1' = 3.0095(7) Å. Au1–Au2–Au1' = 180.0˚ and (b) The relative orientation of $[C_4Me_3N]^+$ cations to the 1-D gold(I) chain; *i*-mnt ligand and hydrogen atoms omitted for clarity. Colour scheme: Au, orange; S, yellow; C, grey; N, blue.

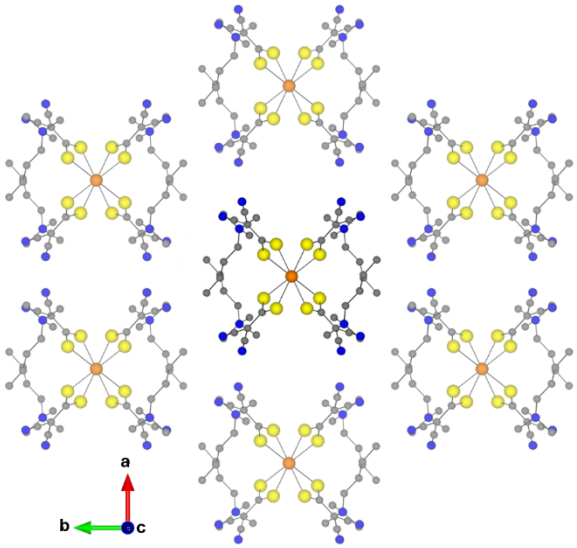

Figure 2.14: Pseudo-hexagonal crystal structure of arrangement of 1-D chains in $[C_4Me_3N]_2[Au_2(i\text{-}mnt)_2]$, viewed down the *c* axis. Hydrogen atoms are omitted for clarity. Colour scheme: Au, orange; S, yellow; C, grey; N, blue.

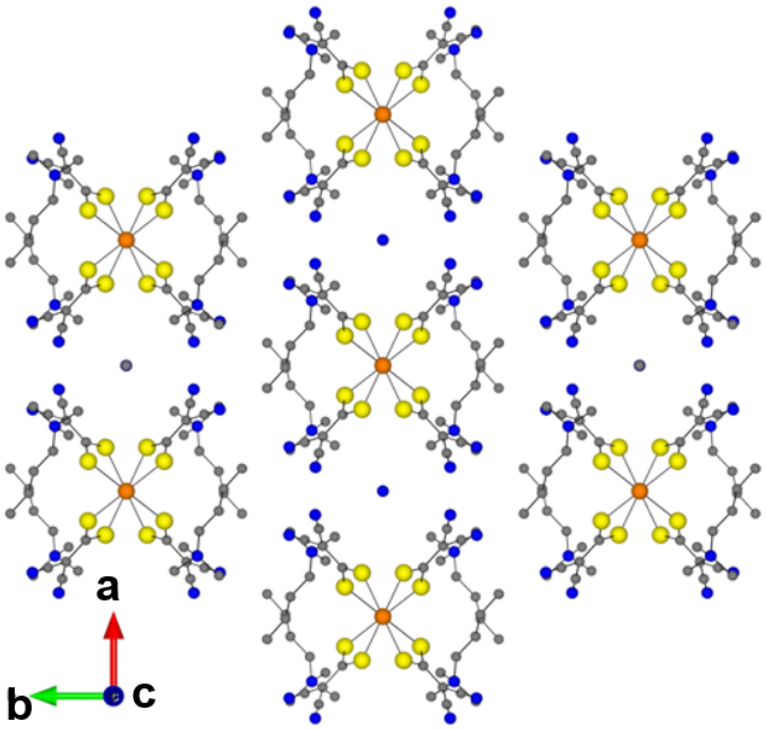

Figure 2.15: Supramolecular arrangement of $[C_4Me_3N]_2[Au_2(i\text{-mnt})_2]\cdot MeCN$ displaying pseudo-hexagonal packing, viewed along the *c*-axis. MeCN solvent molecules are filling in the cavity between the gold(I) chains. Hydrogen atoms are omitted for clarity. Colour scheme: Au, orange; S, yellow; C, grey; N, blue.

The $[C_8Me_3N]_2[Au_2(i\text{-mnt})_2]$ and $[C_{10}Me_3N]_2[Au_2(i\text{-mnt})_2]$ systems are isostructural and have some similarities in both structural and supramolecular packing to the crystal structure of $[C_4Me_3N]_2[Au_2(i\text{-mnt})_2]$. Both structures feature 1-D chains consisting of $[Au_2(i\text{-mnt})_2]^{2-}$ units, each of which exhibit a twisted configuration around the Au(I) core, where $[C_{10}Me_3N]_2[Au_2(i\text{-mnt})_2]$ displays a higher torsional angle at C1–S1–S2–C2 than $[C_8Me_3N]_2[Au_2(i\text{-mnt})_2]$ of 37.1(14)° (Figure 2.16a) and 22.8(8)° (Figure 2.17a) respectively; both dimers, however, are substantially less twisted than in the $[C_4Me_3N]_2[Au_2(i\text{-mnt})_2]$ structure. These structures display shorter intermolecular Au(I) – Au(I) distances of 2.9154(13) Å and 2.8845(9) Å compared to $[C_4Me_3N]_2[Au_2(i\text{-mnt})_2]$. Unlike in the $[C_4Me_3N]_2[Au_2(i\text{-mnt})_2]$ system, these alkyl chains all exhibit some positional disorder near the ammonium headgroup on the alkyl chain and are aligned approximately parallel to the 1–D gold(I) chain (Figure 2.16b, Figure 2.17b). These long alkyl chain cations together wrap around the 1-D gold(I) chain to construct a tetragonal supramolecular packing (Figure 2.18). It should be noted that the $[C_8Me_3N]_2[Au_2(i\text{-mnt})_2]$

structure contains an accessible void of 230 Å^3 which contains diffuse electron density consistent with disordered solvent. Attempts to model these potential solvent molecules in the void as either methanol or acetonitrile were not successful, but IR data shows the presence of both of these solvents in the crystal.

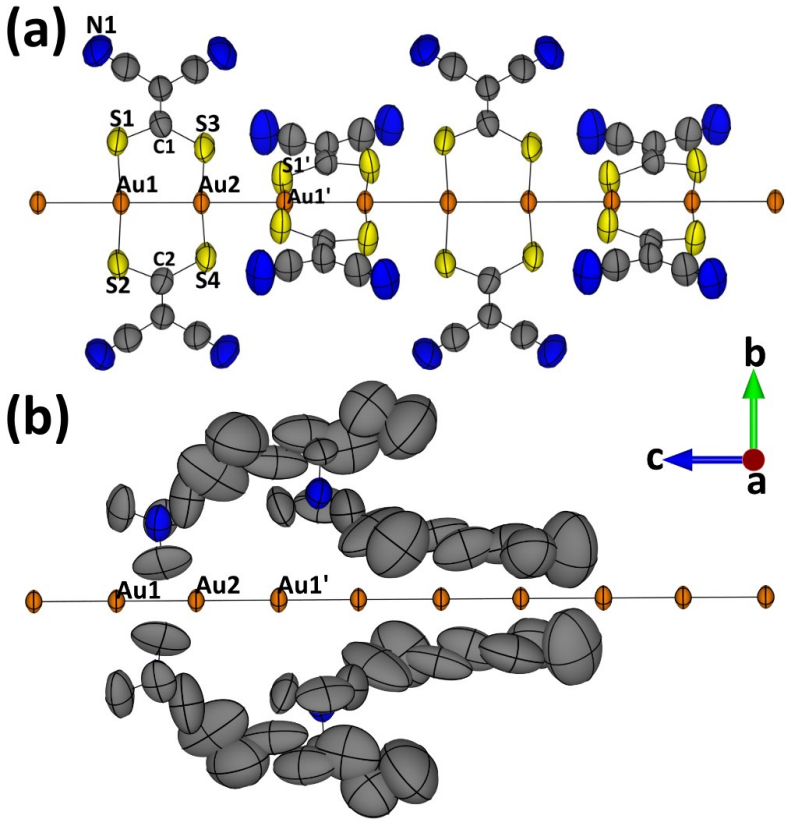

Figure 2.16: (a) Crystal structure illustrating the relative orientation of the 1-D aurophilic chain in $[C_8Me_3N]_2[Au_2(i\text{-mnt})_2]$. $[C_8Me_3N]^+$ cations are omitted for clarity. Au1–Au2 = 2.7827(9) Å, Au2–Au1' = 2.8845(9) Å. Au1– Au2– Au1' angle = 180.0˚. (b) The relative orientation of $[C_8Me_3N]^+$ cations to the 1-D gold(I) chain; *i*-mnt ligand and hydrogen atoms omitted for clarity. Colour scheme: Au, orange; S, yellow; C, grey; N, blue.

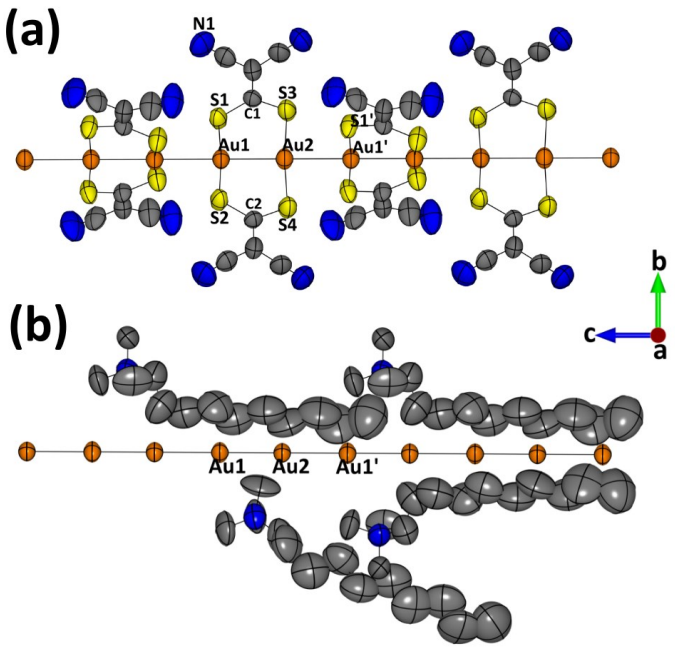

Figure 2.17: (a) Crystal structure illustrating the relative orientation of the 1-D aurophilic chain in $[C_{10}Me_3N]_2[Au_2(i\text{-mnt})_2]$. $[C_{10}Me_3N]^+$ cations are omitted for clarity. Au1–Au2 = 2.7836(13) Å, Au2–Au1' = 2.9154(13) Å. Au1– Au2–Au1' angle = 180.0˚. (b) The relative orientation of $[C_{10}Me_3N]^+$ cations to the 1-D gold(I) chain; *i*-mnt ligand and hydrogen atoms omitted for clarity. Colour scheme: Au, orange; S, yellow; C, grey; N, blue.

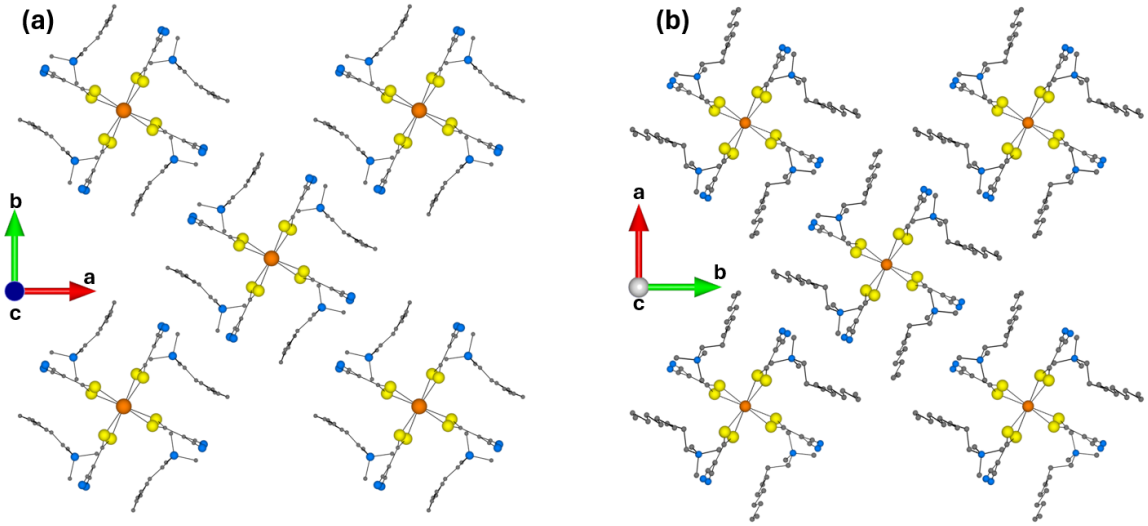

Figure 2.18: Tetragonal arrangement of 1-D aurophilic chains viewed along the *c* axis in (a) $[C_8Me_3N]_2[Au_2(i\text{-mnt})_2]$ and (b) $[C_{10}Me_3N]_2[Au_2(i\text{-mnt})_2]$. Hydrogen atoms are omitted for clarity. Colour scheme: Au, orange; S, yellow; C, grey; N, blue.

In the case of $[C_{16}Me_3N]_2[Au_2(i\text{-mnt})_2]$, the anionic 1-D chains of gold(I) dimers are still observed, with nearly identical intra- and intermolecular aurophilic distances of 2.8151(6) Å and 3.0090(5) Å, respectively, when compared to the $[C_4Me_3N]_2[Au_2(i\text{-mnt})_2]$ structure. However, each $[Au_2(i\text{-mnt})_2]^{2-}$ unit displays a planar conformation, having two very small C–S–S–C dihedral angles (0.9(6), 8.1(6)°), unlike the twisted conformations observed with smaller alkyl chain cation systems. The Au-Au-Au angle along the 1-D chain is more acute (172.1°) than in the other systems (180°), indicating a small but significant deviation from linearity (Figure 2.19). Interestingly, the adjacent 1-D gold(I) chains arrange together in parallel 2-D sheets that are separated by the long cetyl-chain cation (Figure 2.20a) with a distance between these 2-D sheets of 22.395(3) Å (Figure 2.20b). The cetyl chains adopt a zig-zag geometry, are more ordered, and are tilted by approximately 56˚ to the plane of the 2-D sheets (Figure 2.20c). These individual gold(I) chains within the 2-D sheet are separated by an orthogonal distance of 11.0193(17) Å (Figure 2.20d). Critically, when observing the structure along the *b*–axis, the supramolecular packing of $[C_{16}Me_3N]_2[Au_2(i\text{-mnt})_2]$ is completely different from the columnar-type packing as described previously - instead, it could be best described as lamellar. The ordering of multiple layers of cetyl chains cation tilted at an angle and sandwiched in between the planes containing 1-D gold(I) chains resembles the ordering in a smectic C liquid crystal phase (Figure 2.21).

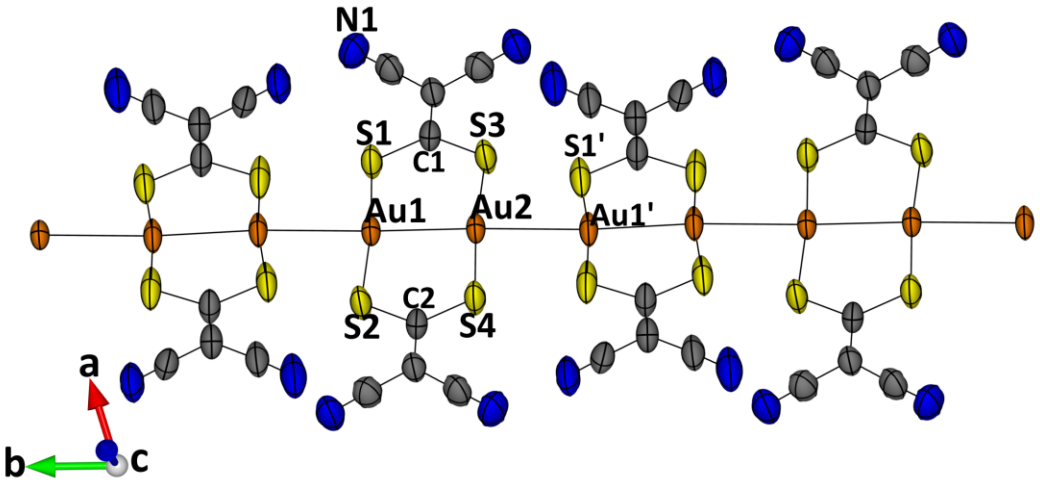

Figure 2.19: Crystal structure of $[C_{16}Me_3N]_2[Au_2(i\text{-mnt})_2]$, showing the 1-D aurophilic chain. Cetyltrimethylammonium cations are omitted for clarity. Au1–Au2 = 2.8151(6) Å, Au2–Au1' = 3.0090(5)Å. Au1–Au2–Au1' = 172.1˚. Colour scheme: Au, orange; S, yellow; C, grey; N, blue.

These observations of the $[C_{16}Me_3N]_2[Au_2(i\text{-mnt})_2]$ crystal structure showed that the supramolecular packing can be controlled by a variation of the alkyl chain length of the cations while still generating the 1-D gold(I) chains. In this case, the longer alkyl chains change the supramolecular assemblies from pseudo-hexagonal to tetragonal columnar to lamellar phases. Therefore, the alkyl chain length should be viewed as another key aspect that could affect the arrangement of the molecules when designing new coordination polymers.

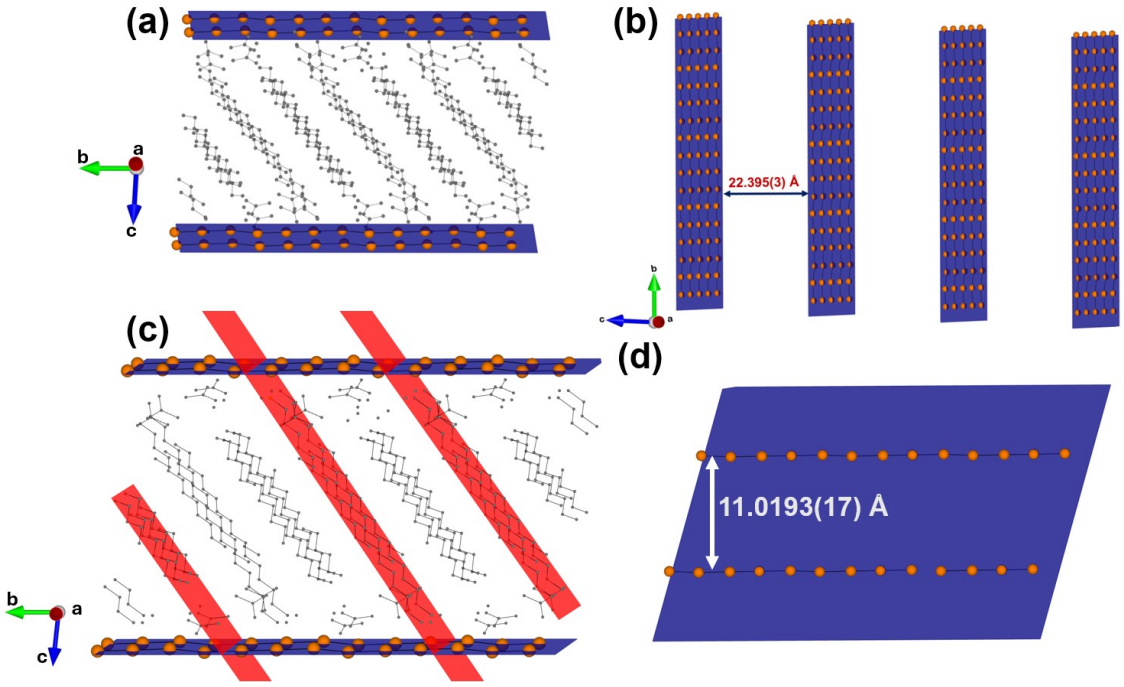

Figure 2.20: Crystal structure of $[C_{16}Me_3N]_2[Au_2(i\text{-mnt})_2]$ illustrates (a) the 1-D gold(I) chains are orientated in parallel sheets (blue plane) that sandwich cetyl chain cations; (b) the distance between individual 2-D sheets; (c) cetyl chains (red plane) are tilted by approximately 56˚ relative to the plane of the 2-D sheets; (d) the orthogonal distance between each gold(I) chain inside the 2-D sheet of 11.0193(17) Å. The *i*-mnt ligand, nitrogen and hydrogen atoms are omitted for clarity. Colour scheme: Au, orange; C, grey.

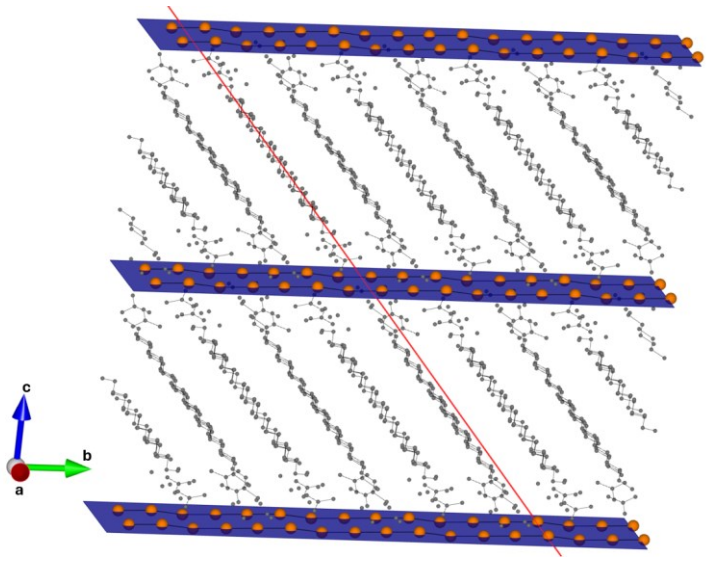

Figure 2.21: The supramolecular packing in the crystal structure of $[C_{16}Me_3N]_2[Au_2(i\text{-}mnt)_2]$ features multiple tilted cetyl chain cations versus the plane of 1-D gold(I) chains and share many similarities with smectic C liquid crystals. The red plane shows the direction of the alkyl chain cations. The *i*-mnt ligand, nitrogen and hydrogen atoms are omitted for clarity. Colour scheme: Au, orange; C, grey.

2.2.3. Photoluminescence properties of $[RMe_3N]_2[Au_2(i\text{-}mnt)_2]$

Due to the presence of both intra and intermolecular aurophilic interactions, all the materials herein exhibited photoluminescence in the solid-state. The luminescence data can be categorized into one set of similar data for the columnar-packed systems, including $[C_4Me_3N]^+$, $[C_8Me_3N]^+$, and $[C_{10}Me_3N]^+$ salts, and a distinctly separate observation for the lamellar structure $[C_{16}Me_3N]_2[Au_2(i\text{-}mnt)_2]$. The columnar systems in general feature broad excitation bands from ca. 400 to 600 nm and an orange – red emission at λ_{max} = 590 – 630 nm at room temperature, which are summarized in Table 2.2 and are described below.

$[C_4Me_3N]_2[Au_2(i\text{-}mnt)_2]$ shows one pronounced excitation peak centered around 515 nm with another somewhat conspicuous excitation band at 410 nm. The corresponding emission spectrum displays a single broad band at λ_{max} = 610 nm with quantum yield (Φ) = 5% (Figure 2.23). The solvated isostructural form, $[C_4Me_3N]_2[Au_2(i\text{-}mnt)_2]\cdot MeCN$, displays a single, broad excitation band between 400 nm to 580 nm that is also centered close to the excitation peak of its unsolvated structure at λ_{max} = 510 nm. However, the emission maximum of the solvated structure is blue-shifted by 21 nm with emission at λ_{max} = 591 nm (Figure 2.25).

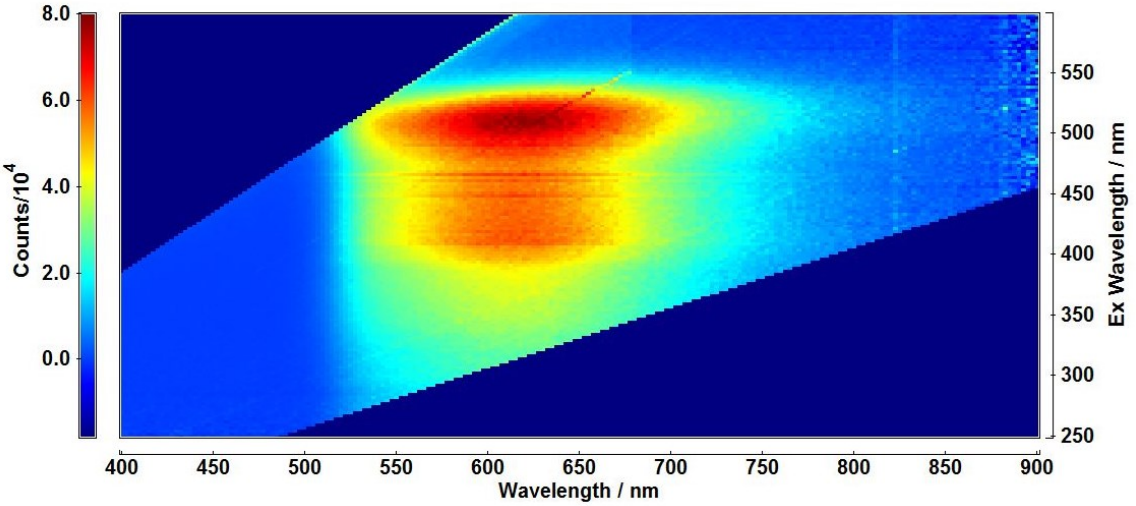

Figure 2.22: EEM spectrum of the non-solvated $[C_4Me_3N]_2[Au_2(i\text{-mnt})_2]$ structure illustrates the emissive region at ca. 610 nm.

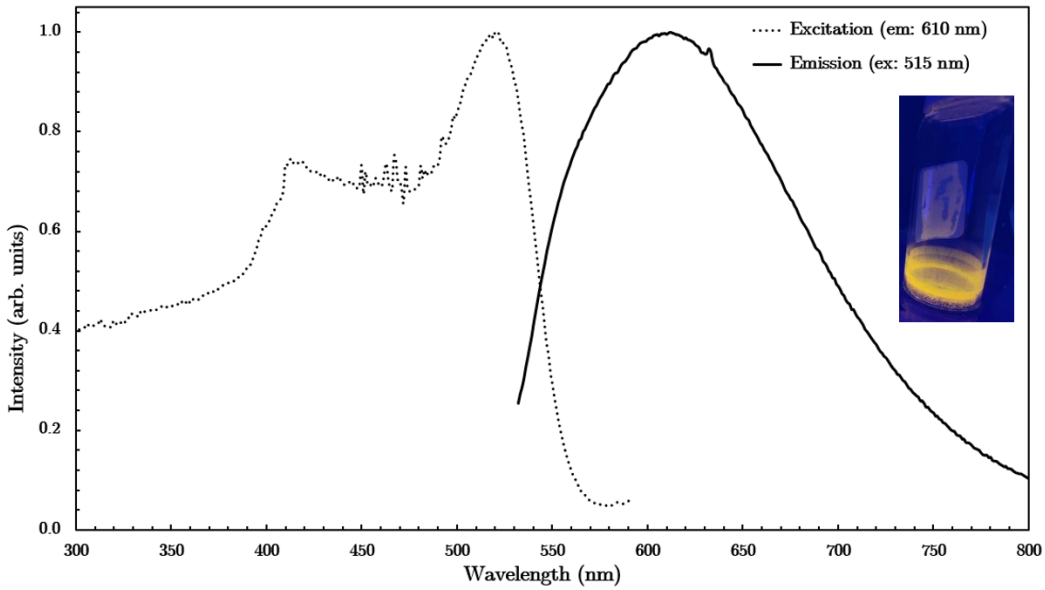

Figure 2.23: Excitation (dotted line) and emission (solid line) spectra of $[C_4Me_3N]_2[Au_2(i\text{-mnt})_2]$. The small sharp peak at 640 nm is an instrumental artifact.

Table 2.2: Summary of luminescence data for $[RMe_3N]_2[Au_2(i\text{-mnt})_2]$ structures at 296 K.

$[RMe_3N]^+$	Excitation λ_{max} (nm)	Emission λ_{max} (nm)
$[C_4Me_3N]$	515	610
$[C_4Me_3N]$ · MeCN	510	591
$[C_8Me_3N]$	585	630
$[C_{10}Me_3N]$	578	615
$[C_{16}Me_3N]$	510	550

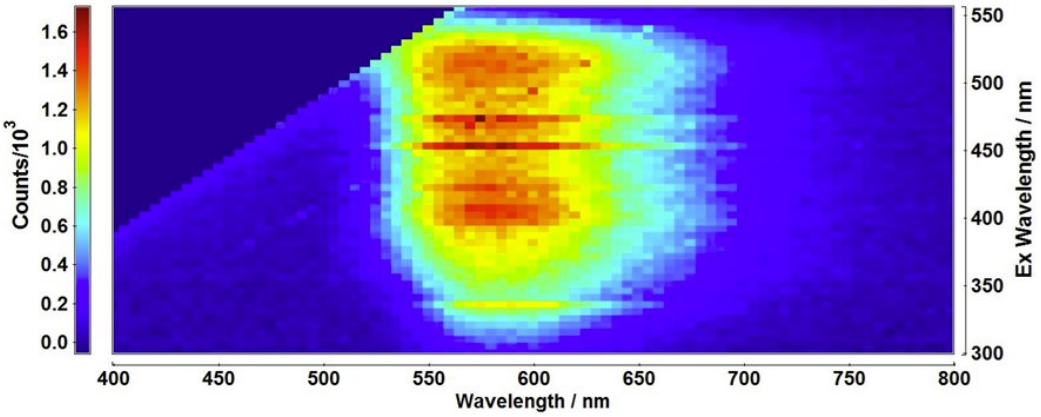

Figure 2.24: EEM spectrum of the solvated $[C_4Me_3N]_2[Au_2(i\text{-mnt})_2]$ ·MeCN structure illustrates the emissive region at ca. 590 nm.

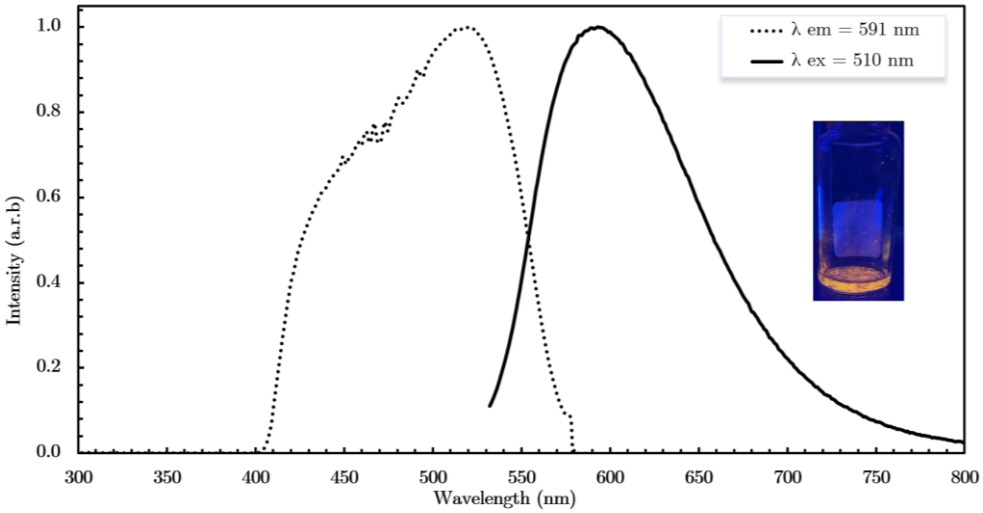

Figure 2.25: Excitation (dotted line) and emission (solid line) spectra of $[C_4Me_3N]_2[Au_2(i\text{-mnt})_2]$·MeCN.

Interestingly, when exposing the un-solvated crystals of $[C_4Me_3N]_2[Au_2(i\text{-mnt})_2]$ to MeCN vapor, the emission maximum is immediately blue-shifted to the same λ_{max} = 591 nm as the emission peak recorded for the $[C_4Me_3N]_2[Au_2(i\text{-mnt})_2]\cdot$MeCN structure. Leaving the $[C_4Me_3N]_2[Au_2(i\text{-mnt})_2]\cdot$MeCN crystals over time (20 minutes) for de-solvation to occur led to a similar emission spectrum of $[C_4Me_3N]_2[Au_2(i\text{-mnt})_2]$ (Figure 2.26), thus the conversion and the associated emission spectra that are observed is reversible. The mechanism of this conversion remains unclear.

The excitation spectra of both $[C_8Me_3N]_2[Au_2(i\text{-mnt})_2]$ and $[C_{10}Me_3N]_2[Au_2(i\text{-mnt})_2]$ are both alike with a more red-shifted excitation compared to the $[C_4Me_3N]^+$ systems and showing a wide excitation band with a range from ≈ 400 nm to 600 nm. It should be noted that the sharp signals in the excitation spectra are instrumental artifacts. The emission spectra of both structures exhibit a prominent and broad emission band with a slight variance in the emission maxima of $[C_8Me_3N]_2[Au_2(i\text{-mnt})_2]$ (Figure 2.28) and $[C_{10}Me_3N]_2[Au_2(i\text{-mnt})_2]$ (Figure 2.30) at λ_{max} = 630 nm and λ_{max} = 615 nm respectively.

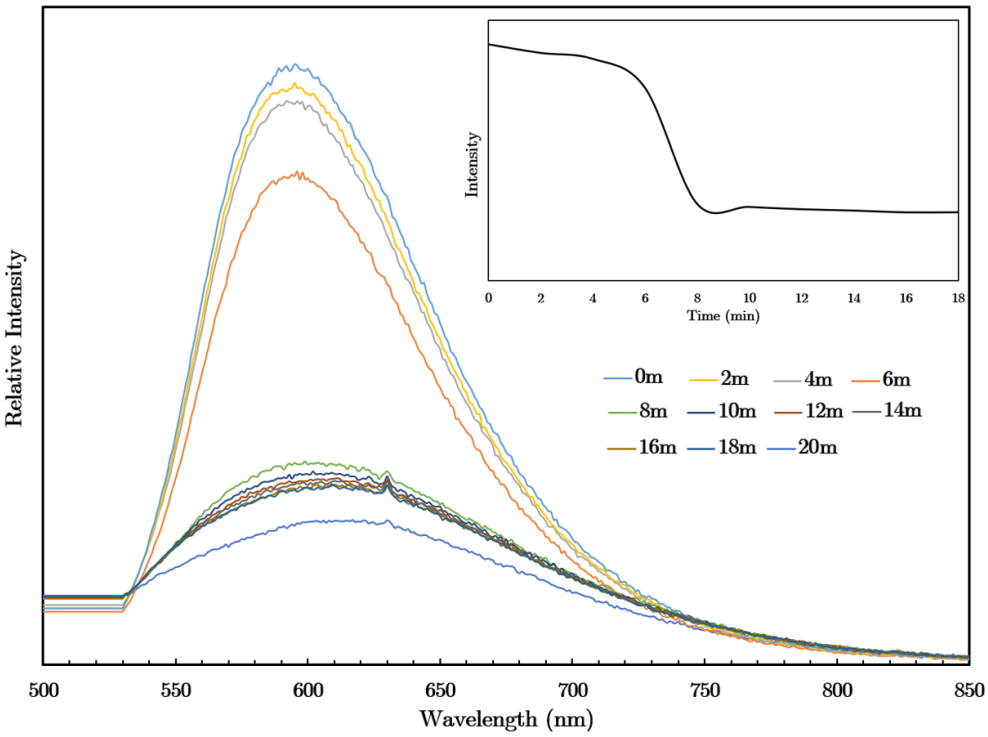

Figure 2.26: Monitoring solid-state emission spectra of $[C_4Me_3N]_2[Au_2(i\text{-mnt})_2]\cdot$MeCN ($\lambda_{ex}$ = 490 nm) upon de-solvation of MeCN over 20 min at 2 min intervals. Relative intensity of emission at 591 nm over time (inset). The letter "m" noted in legends is short form for minute with 0m when the experiment started.

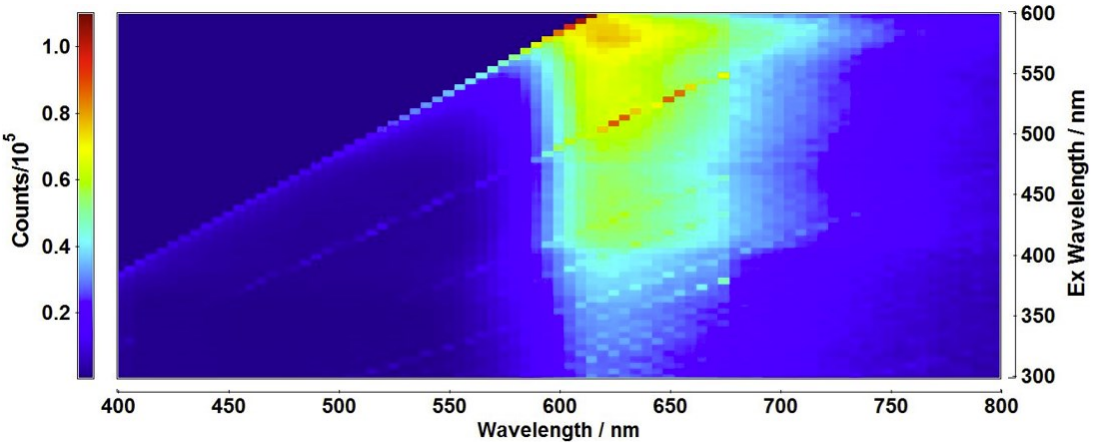

Figure 2.27: EEM spectrum of the $[C_8Me_3N]_2[Au_2(i\text{-mnt})_2]$ structure illustrates the emissive region at ca. 625 nm.

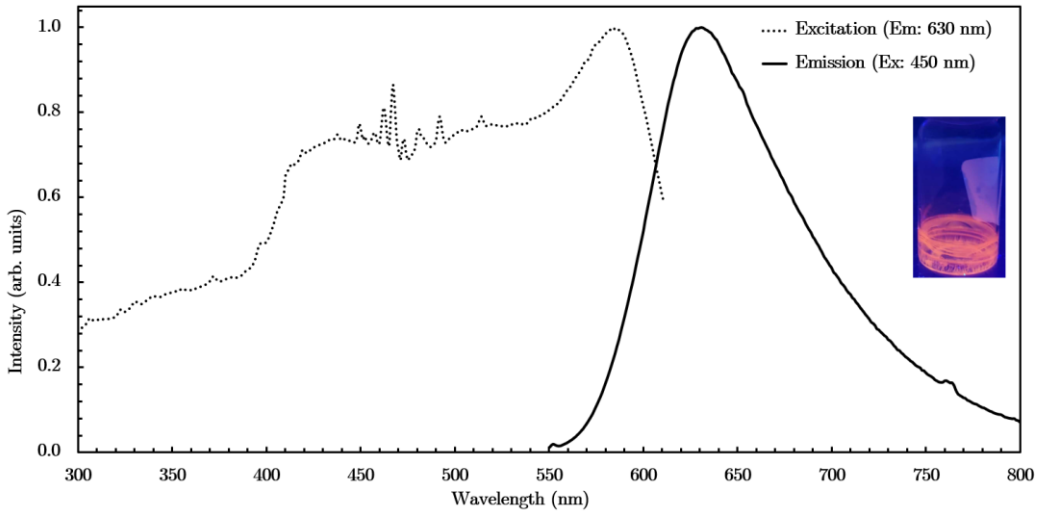

Figure 2.28: Excitation (dotted line) and emission (solid line) spectra of $[C_8Me_3N]_2[Au_2(i\text{-mnt})_2]$.

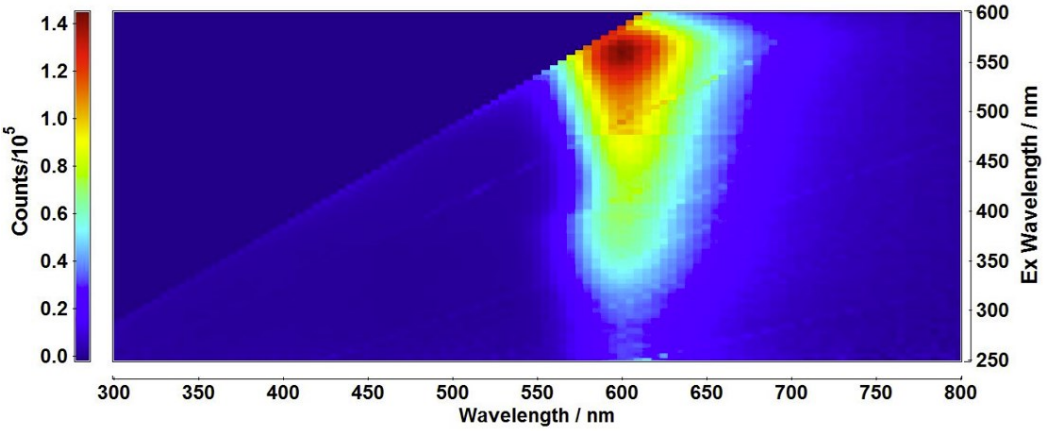

Figure 2.29: EEM spectrum of the $[C_{10}Me_3N]_2[Au_2(i\text{-mnt})_2]$ structure illustrates the emissive region at ca. 605 nm.

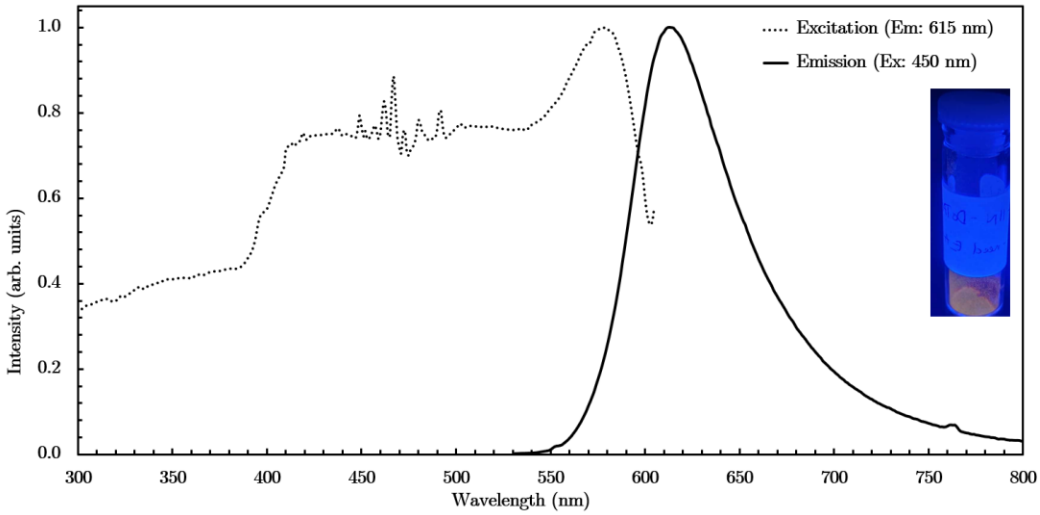

Figure 2.30: Excitation (dotted line) and emission (solid line) spectra of $[C_{10}Me_3N]_2[Au_2(i\text{-mnt})_2]$.

The anomaly regarding the luminescent properties among the $[RMe_3N]_2[Au_2(i\text{-mnt})_2]$ series appears in the smectic-like structure $[C_{16}Me_3N]_2[Au_2(i\text{-mnt})_2]$ (Figure 2.32). The pronounced excitation band is narrow with a range of ≈ 400 nm to 520 nm with the excitation maxima centered at λ_{max} = 510 nm, similar to the excitation spectrum of $[C_4Me_3N]_2[Au_2(i\text{-mnt})_2]$ (Figure 2.23). However, the emission spectrum of $[C_{16}Me_3N]_2[Au_2(i\text{-mnt})_2]$ features an emission band that is half the width compared to the columnar-packed systems. In addition, the emission maximum of $[C_{16}Me_3N]_2[Au_2(i\text{-mnt})_2]$ strongly deviates

from the typical orange – red emission of the columnar-packed structures $[RMe_3N]_2[Au_2(i\text{-}mnt)_2]$, instead shifting to a higher-energy green emission centred at λ_{max} = 550 nm.

The emission maxima of all structures in the $[RMe_3N]_2[Au_2(i\text{-}mnt)_2]$ series, which all contain intermolecular aurophilic interaction between anions, are very red-shifted as compared to the isolated gold(I) dimers in $[n\text{-}Bu_4N]_2[Au_2(i\text{-}mnt)_2]$ (λ_{max} = 515 nm; Table 2.1). The origin of the photoluminescent properties for the $[RMe_3N]_2[Au_2(i\text{-}mnt)_2]$ series is discussed more extensively in Section 2.2.4. It is worth pointing out that aurophilicity and its emission mechanism is a complex topic with many on-going discussions in current literature.[35, 37, 39, 95, 108, 111,112]

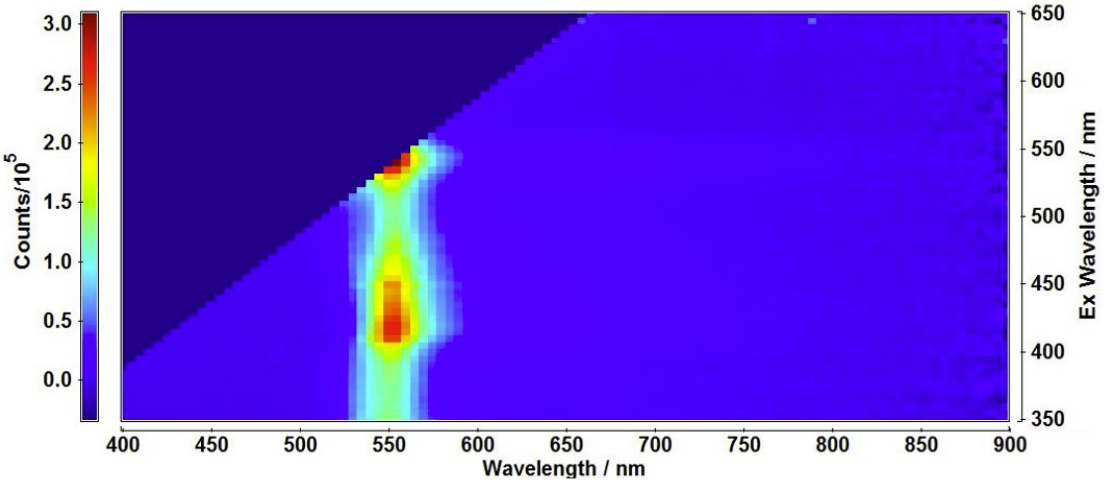

Figure 2.31: EEM spectrum of the $[C_{16}Me_3N]_2[Au_2(i\text{-}mnt)_2]$ structure illustrates the emissive region at ca. 550 nm.

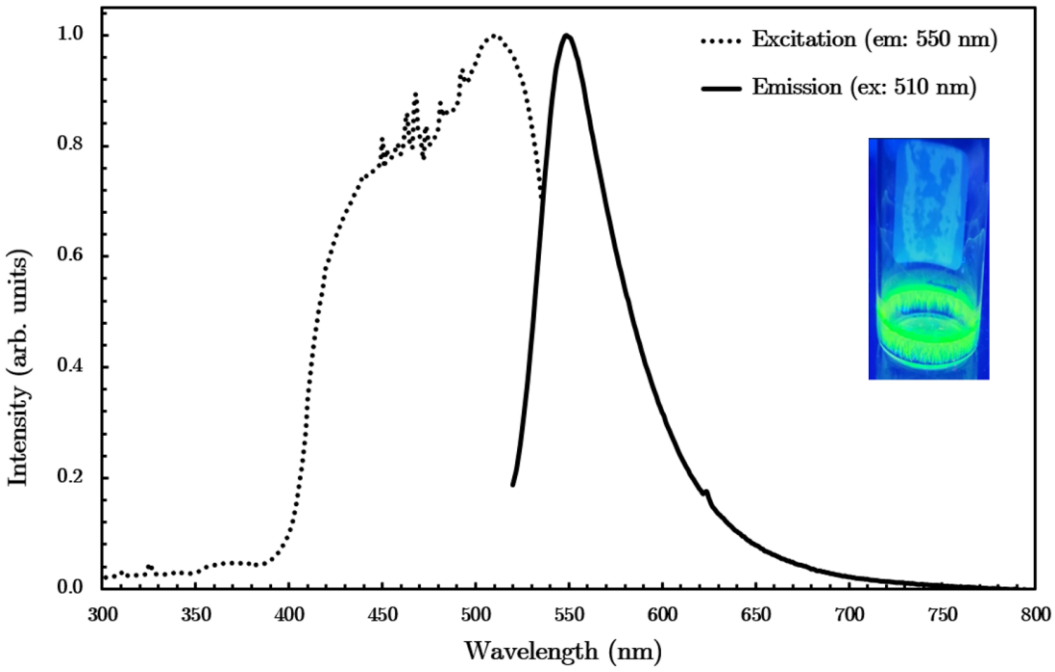

Figure 2.32: Excitation (dotted line) and emission (solid line) spectra of $[C_{16}Me_3N]_2[Au_2(i\text{-}mnt)_2]$.

2.2.4. Relationship between Crystal Structures and their Luminescent Properties

Aurophilic-containing structures are often emissive. The emission from a simple linear, monometallic coordination polymer species as $[Au(CN)_2]^-$ is generally assumed to primarily arise from metal-to-metal charge transfer between aggregated aurophilic $[Au(CN)_2]^{2-}$ anions. In particular, the Au(I) – Au(I) distance is first thought to be directly proportional to the energy gap (ΔE) between the bonding and antibonding orbitals of the aurophilic interaction between gold(I) atoms, in which a shorter aurophilic bond would lead to a larger energy gap between HOMO and LUMO and therefore, result in an overall red-shift of luminescence.[107]

The photoluminescence in dinuclear gold(I) coordination polymers however is more difficult to interpret due to many dynamic variables that interplay and contribute toward determining the emission energy. Recent work in the Leznoff group with a series of gold(I) dithiocarbamate complexes showed that they can display very different emission energies while retaining nearly identical Au – Au distances but differing in the Au-Au-Au angle, which can influence the overlap of the Au(I) orbitals that normally contribute to aurophilic interactions.[86] It has also been shown that the emission spectra of gold(I) thiol-

based dimers are likely assignable as ligand-to-metal-metal charge transfer (LMMCT) [S → Au – Au], and this is likely also the case for an infinite gold(I) chain of gold-thiolate dimers.[108] However, structural flexibility of the chelating dithiolate ligands around the dinuclear Au(I) core, in this case in $[Au_2(i\text{-mnt})_2]^{2-}$, is another important factor worth considering as a more rigid structure could prevent the dissipation of energy through the nonradiative relaxation process;[109] depending on the amount of twist, the LMMCT assignment could also change, as was observed in a series of related $Au_2(\text{dithiolate})_2$ systems.[110] On the other hand, a more flexible framework (decreased molecular rigidity) could be susceptible to external physical or chemical stimuli.[95,111] In other words, the structural properties of the chelating dithiolate ligand could affect how energy is being transferred from the ligand to the aurophilic bonding network. Aurophilic bonds that are sensitive to any structural modification could therefore result in a change in emission energy.

In an attempt to correlate the photoluminescence properties of $[RMe_3N]_2[Au_2(i\text{-mnt})_2]$ systems with their corresponding structural arrangements, four parameters that could potentially impact the emission energy from the aurophilic gold(I) chain were examined: (1) the inter-molecular aurophilic distance (Au2-Au1'); (2) the average intra-torsional angle around Au(I) atoms (measured as C-S-S-C, the α torsional angle; Figure 2.33) in the $[Au_2(i\text{-mnt})_2]^{2-}$ anion, which is calculated by taking the average angle of the (C1-S1-S2-C2) and (C1-S3-S4-C2) torsional angles; (3) the smallest inter-torsional angle around Au(I) atoms that represents the conformation between gold(I) dimer units (S3-Au2-Au1'-S1', the β angle; Figure 2.33) between $[Au_2(i\text{-mnt})_2]^{2-}$ anions; and (4) the angle along the gold(I) chains (Au1-Au2-Au1') (Figure 2.33). The molecular torsional angles, α and β, in the $[Au_2(i\text{-mnt})_2]^{2-}$ anion were chosen in addition to the Au-Au-Au angle and aurophilic distance, as it provides insights into structural flexibility and conformation of the framework, and was a key factor in the related $Au_2(\text{dopdtc})_2$ system where a high twist generated a change in the ordering of the orbitals and the associated emission energy assignment.[110] The intra-molecular aurophilic distance in the $[Au_2(i\text{-mnt})_2]^{2-}$ units across the $[RMe_3N]_2[Au_2(i\text{-mnt})_2]$ series was noted but was not considered as a factor contributing to the changes in emission energies because these distances were very similar across the series. The solvated structure $[C_4Me_3N]_2[Au_2(i\text{-mnt})_2] \cdot MeCN$ is also included herein.

The Au-Au-Au angle of each $[RMe_3N]_2[Au_2(i\text{-mnt})_2]$ structure is summarized in Table 2.3, highlighting the presence of linear 1-D gold(I) chains with shorter alkyl chain

cations, with the exception of the 172.1° angle in $[C_{16}Me_3N]_2[Au_2(i\text{-mnt})_2]$. For the other three factors, correlation graphs for the intermolecular aurophilic distance (Figure 2.34), intra-torsional angle (Figure 2.35) and inter-torsional angle (Figure 2.36) are outlined below.

Table 2.3: Summary of the Au – Au – Au angle values of each structure in $[RMe_3N]_2[Au_2(i\text{-mnt})_2]$.

$[RMe_3N]^+$	$[C_4Me_3N]^+$	$[C_4Me_3N]\cdot MeCN$	$[C_8Me_3N]^+$	$[C_{10}Me_3N]^+$	$[C_{16}Me_3N]^+$
Angle (°)	180	180	180	180	172.1

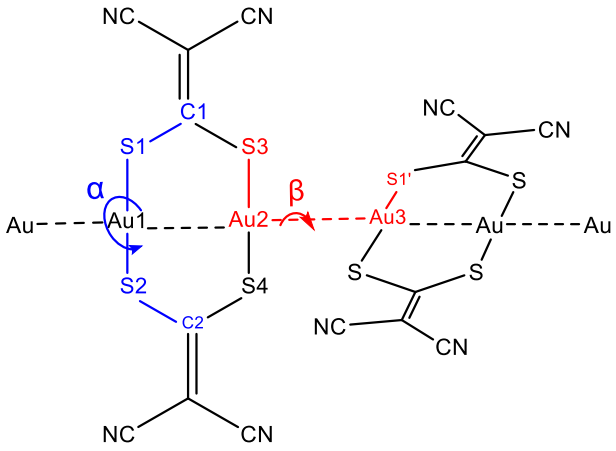

Figure 2.33: Labelling on each atom of the $[Au_2(i\text{-mnt})_2]^{2-}$ core, used for structure-property correlation discussion. The atoms that comprise the α and β torsional angles are highlighted in blue and red respectively.

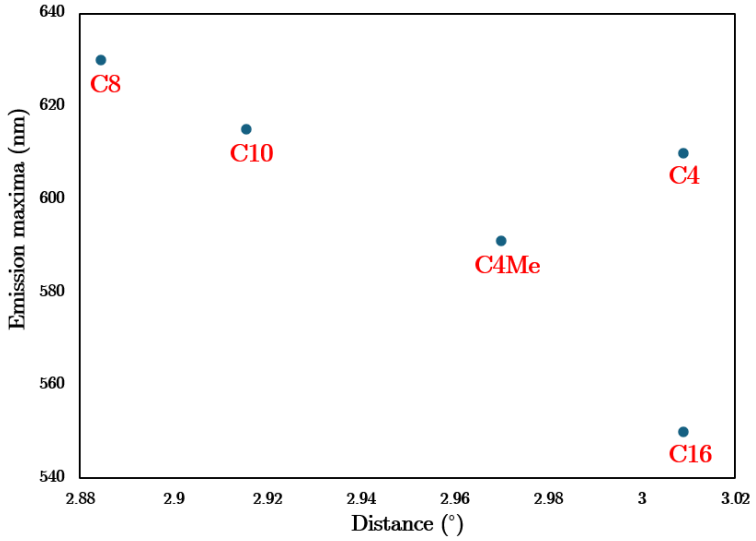

Figure 2.34: Plot of the intermolecular aurophilic distance between the anions and emission maximum (in nm) for each structure in the $[RMe_3N]_2[Au_2(i\text{-mnt})_2]$ series, where R = C_4, C_8, C_{10}, C_{16} represents the length of the alkyl chain in the cation. C_4Me represents the solvated structure $[C_4Me_3N]_2[Au_2(i\text{-mnt})_2]\cdot MeCN$.

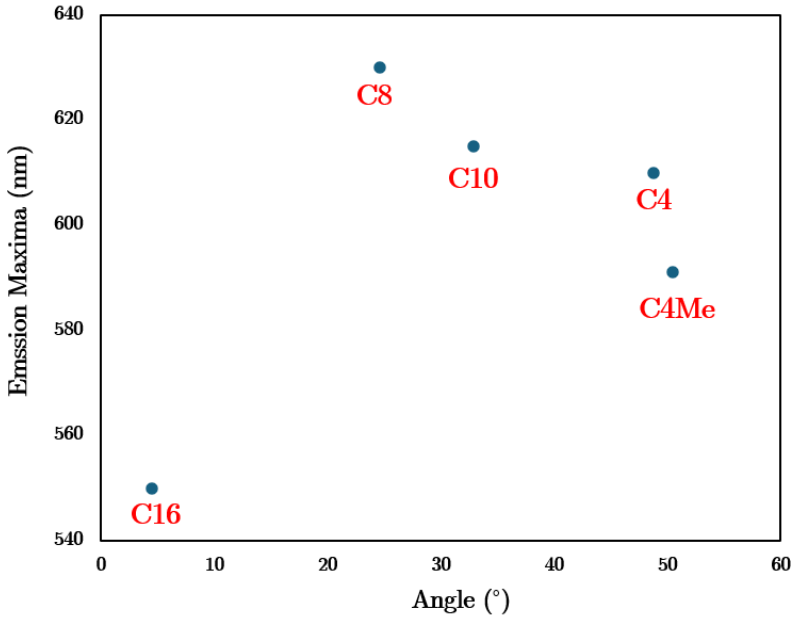

Figure 2.35: Plot of average intra-torsional angle of C-S-S-C (α) within the anion and emission maximum (in nm) for each structure in the $[RMe_3N]_2[Au_2(i\text{-mnt})_2]$ series, where R = C_4, C_8, C_{10}, C_{16} represents the length of the alkyl chain in the cation. C_4Me represents the solvated structure $[C_4Me_3N]_2[Au_2(i\text{-mnt})_2]\cdot MeCN$.

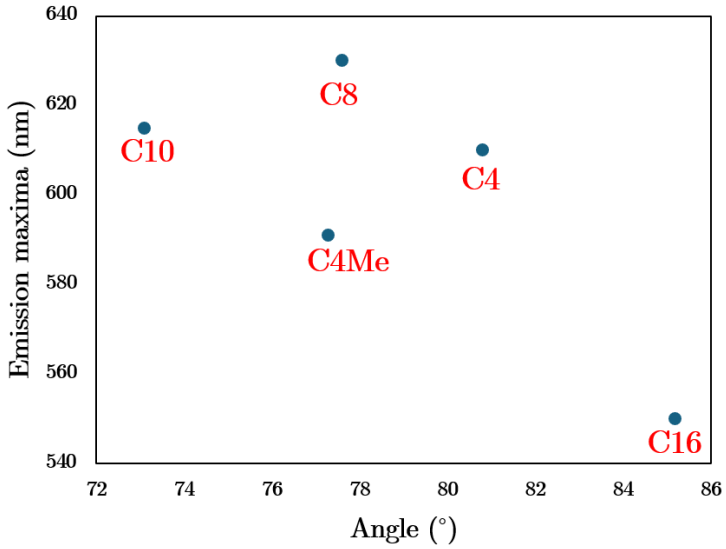

Figure 2.36: Plot of the inter-torsional angle of S-Au-Au-S (β), which represents the conformation between gold(I) dimers, vs. emission maxima (in nm).

In general, there is a weak correlation between both the interaurophilic distance and the intra-torsional angle versus emission maxima, with the exception of $[C_{16}Me_3N]^+$ as an outlier. There is no correlation between the inter-torsional angle and emission maxima. Further examining these parameters, it can be seen that both $[C_4Me_3N]^+$ and $[C_{16}Me_3N]^+$ species have nearly identical intermolecular aurophilic distances but the linearity of Au – Au – Au angle and large intra-torsional angle with $[C_4Me_3N]^+$, which thus adopts a twisted conformation, whereas $[C_{16}Me_3N]^+$ is flatter and has a smaller Au – Au – Au angle of 172˚, results in a unique emission energy. It is possible that some or all of these individual components contribute to some degree toward the overall emission properties of $[RMe_3N]_2[Au_2(i\text{-mnt})_2]$ and not solely be attributed to only one parameter. More importantly, the supramolecular packing is not the only thing that changes as the cation alkyl chain length increases. Incorporating these cations was hypothesized to make the materials mechanically softer, thus opening the potential for designing new mechanoresponsive aurophilic-based materials.

2.2.5. Examining Mechanochromic Behaviour of $[RMe_3N]_2[Au_2(i\text{-mnt})_2]_2$

Given the flexible structural parameters in the aurophilic 1-D chains and their supramolecular arrangements, which are clearly sensitive to small changes in cation, the responses to mechanical stimuli for all solids of $[RMe_3N]_2[Au_2(i\text{-mnt})_2]$ were examined. All

powdered materials were ground from crystals of $[RMe_3N]_2[Au_2(i\text{-mnt})_2]$ using a mortar and pestle for 5 to 30 minutes at room temperature and any changes to their colour or emissive properties were noted.

Upon grinding crystals of $[C_4Me_3N]_2[Au_2(i\text{-mnt})_2]$, they undergo a colour change from light orange crystals to dark red powder. The powdered materials emit red light (details below), are stable at room temperature and did not convert back to the original colour even after 3 months. The IR spectra before and after grinding are nearly identical, suggesting that no reaction occurs that altered the chemical composition of the material. However, these changes in colour and emission for $[C_4Me_3N]_2[Au_2(i\text{-mnt})_2]$ only occur after constant grinding for at least 2 min.

X-ray powder diffraction data was collected from the ground powder and compared with the powder diffractogram generated from the single-crystal data of $[C_4Me_3N]_2[Au_2(i\text{-mnt})_2]$. From these powder diffractograms, it is clear that the ground material is not isostructural to its crystalline form, as evidenced by the major peaks become broader and a peak disappearing at 13° (Figure 2.37). The two major peaks at 7° and 8° shifted by 0.8° after grinding, which suggests that the crystals undergo a structural change when experiencing pressure. We were unable to obtain more detailed structural information from this data. The emission maxima of ground $[C_4Me_3N]_2[Au_2(i\text{-mnt})_2]$ experienced a red-shift of 55 nm to a red emission at λ_{max} = 665 nm (Figure 2.38).

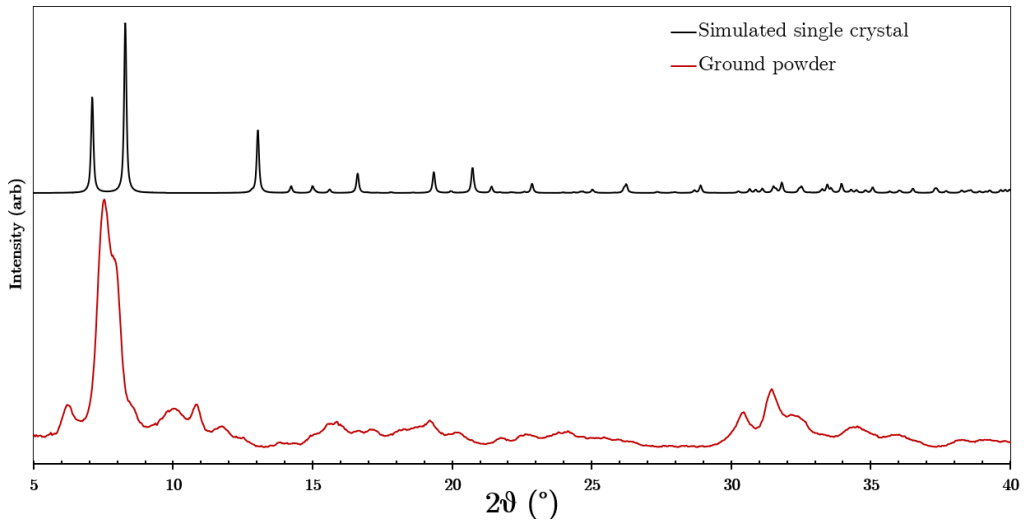

Figure 2.37: Powder X-Ray diffractograms of $[C_4Me_3N]_2[Au_2(i\text{-mnt})_2]$. Diffractogram generated from single crystal data (black), and collected after grinding with mortar and pestle for 5 min (red).

The diffractogram of $[C_8Me_3N]_2[Au_2(i\text{-mnt})_2]$ revealed a substantial change after grinding, with multiple peaks splitting at approximately 6° and most peaks becoming broader (Figure 2.39). As previously mentioned, the crystal structure of $[C_8Me_3N]_2[Au_2(i\text{-mnt})_2]$ has a sizable void between the gold(I) chains that contains trapped solvent molecules of MeOH and MeCN. The FT-IR spectrum of $[C_8Me_3N]_2[Au_2(i\text{-mnt})_2]$ indicated the presence of both MeOH and MeCN and these solvent peaks immediately disappeared after grinding. Therefore, this dissimilarity in PXRD data before and after grinding in the structure could be driven by the loss of solvent from the crystal, but the framework also undergoes structural change that accompanies the solvent loss. Interestingly, the luminescence spectra of $[C_8Me_3N]_2[Au_2(i\text{-mnt})_2]$ crystals and the ground form (Figure 2.40) exhibited no change; they are nearly identical in both excitation and emission spectra, which shows that loss of solvent (and any resulting structural change) does not alter the emission maxima in $[C_8Me_3N]_2[Au_2(i\text{-mnt})_2]$.

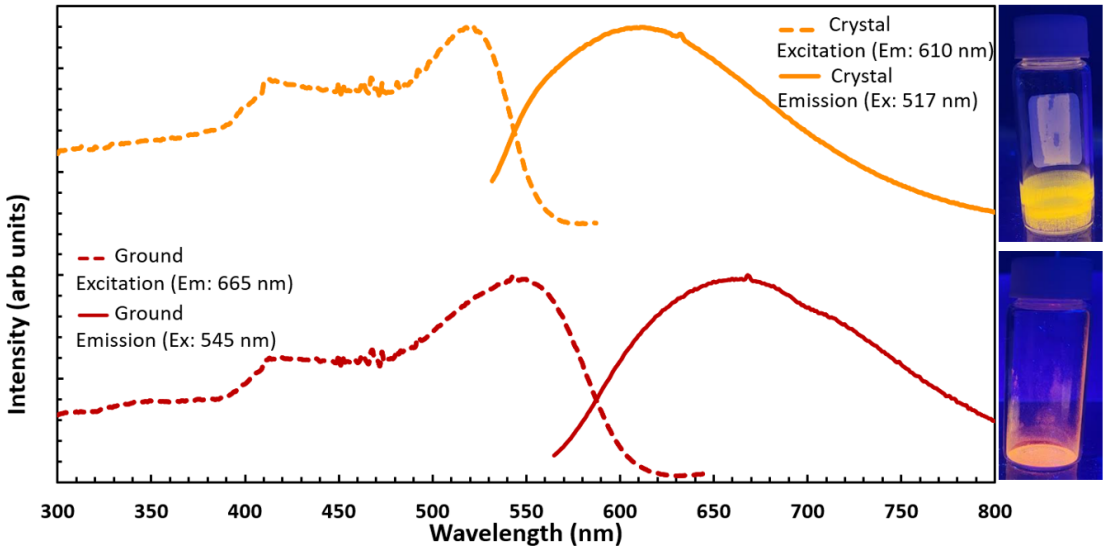

Figure 2.38: Excitation (dashed lines) and emission (solid lines) spectra of crystals of $[C_4Me_3N]_2[Au_2(i\text{-mnt})_2]$ (orange), and ground $[C_4Me_3N]_2[Au_2(i\text{-mnt})_2]$ (red) at room temperature. The small sharp spikes in the spectra are instrumental artifacts.

From the PXRD diffractogram of $[C_{10}Me_3N]_2[Au_2(i\text{-mnt})_2]$ it is evident that the ground structure has an identical pattern to the crystal form, albeit having slightly broader peaks, which suggests that in this case the structure did not undergo any appreciable structural changes or phase transitions upon applying pressure, but at most only generated a decrease in domain size (Figure 2.41). Infrared spectra are also identical

before and after grinding. The photoluminescent properties of the ground material exhibited a small, red-shifted emission of 15 nm, which is unexplained.

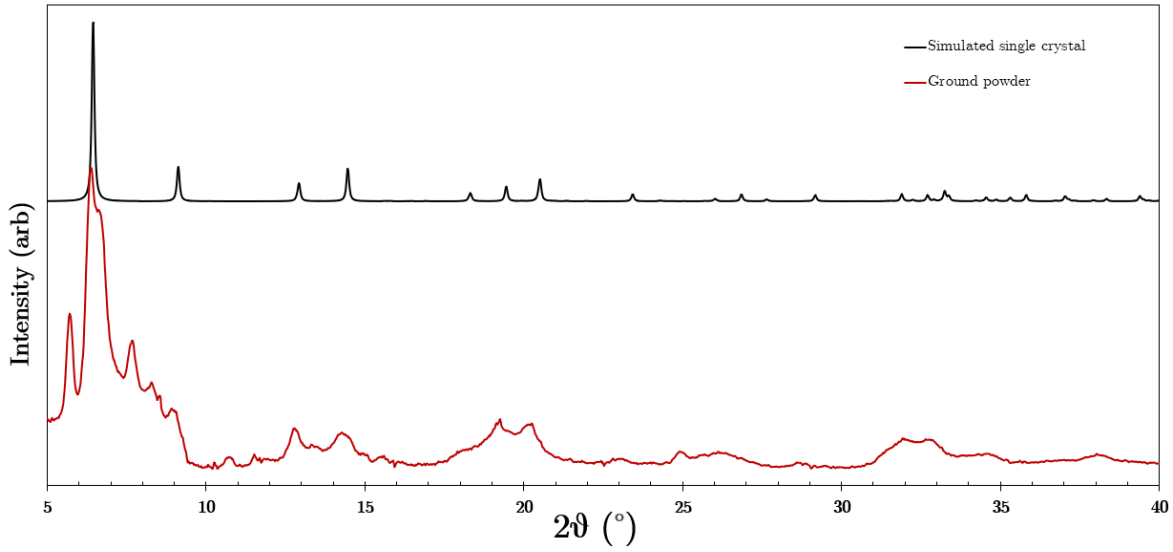

Figure 2.39: Powder X-Ray diffractograms of $[C_8Me_3N]_2[Au_2(i\text{-mnt})_2]$. Diffractogram generated from single crystal data (black), and collected after grinding with mortar and pestle for 5 min (red).

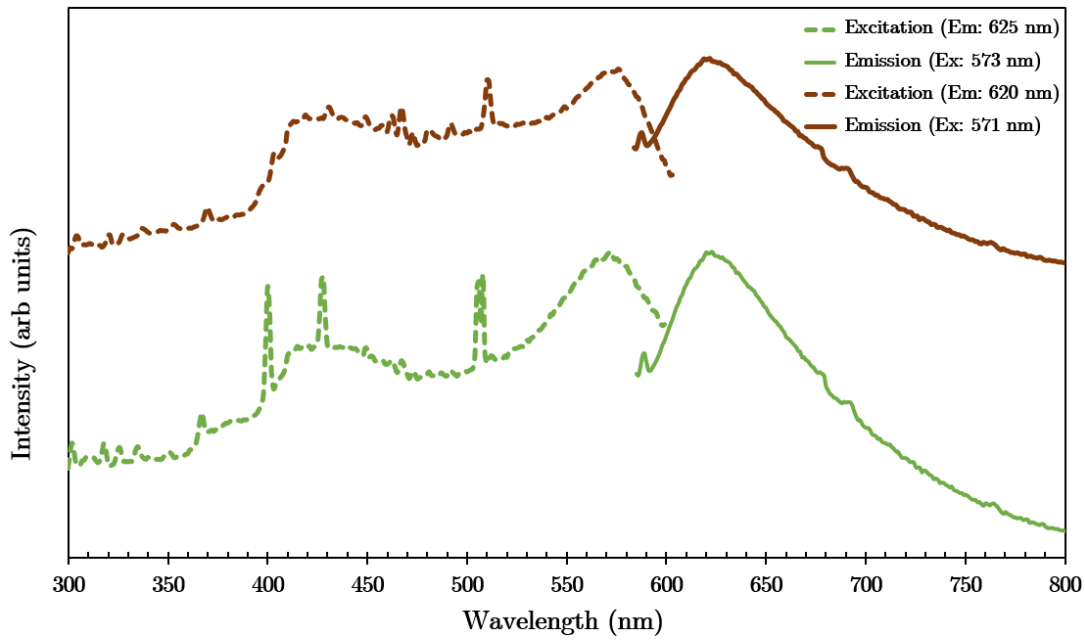

Figure 2.40: Excitation (dashed lines) and emission (solid lines) spectra of crystals of $[C_8Me_3N]_2[Au_2(i\text{-mnt})_2]$ (green), and ground $[C_8Me_3N]_2[Au_2(i\text{-mnt})_2]$ (red) at room temperature. The sharp spikes in the spectra are instrumental artifacts.

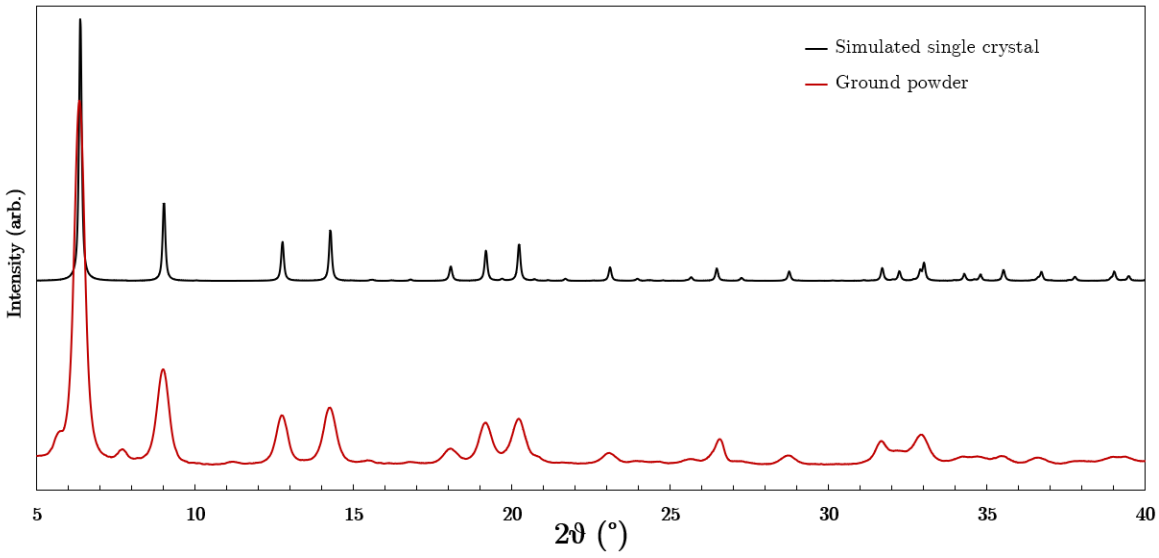

Figure 2.41: Powder X-Ray diffractograms of $[C_{10}Me_3N]_2[Au_2(i\text{-mnt})_2]$. Diffractogram generated from single crystal data (black), collected after grinding with mortar and pestle for 5 min (red).

More dramatically, the lamellar structure $[C_{16}Me_3N]_2[Au_2(i\text{-mnt})_2]$ undergoes a drastic change in emission upon applying very mild pressure (e.g. from the pressure exerted by a spatula tip), with a red-shift in emission maximum to 660 nm from 550 nm visually observable as a green to red-colored emission under a broadband UV-lamp (Figure 2.42). Further substantial grinding (e.g. with a mortar/pestle) induces a further red-shift in the emission, to λ_{max} = 670 nm after 5 min and λ_{max} = 680 nm after 30 min. Interestingly, the emission band of the ground form is three times broader compared to the narrow band of the crystalline form, with a significant red-shift of emission λ_{max} of 120 nm (Figure 2.43).

The PXRD diffractogram data indicates that a structural change occurred after each stage of grinding (Figure 2.45). When pressure is slightly applied using the tip of a spatula to crystals, the powder diffractogram displayed a new and unique 2θ peak at approximately 6.3° in which this intermediate can be attributed to a new crystalline phase. This critical observation indicates that scratching crystals generates a mixture containing a new intermediate crystalline phase transition; some starting material also remains. Substantial grinding past 5 min removes the unique peak, widens all peaks, and all traces of the starting material disappears; this represents full conversion to a new phase that is more amorphous than the original crystals. The unit cell was also enlarged after grinding,

as evidenced by a minor shift of the lowest-angle diffraction peak to a lower 2θ angle (4° to 3°), but no further structural elucidations of these materials were pursued.

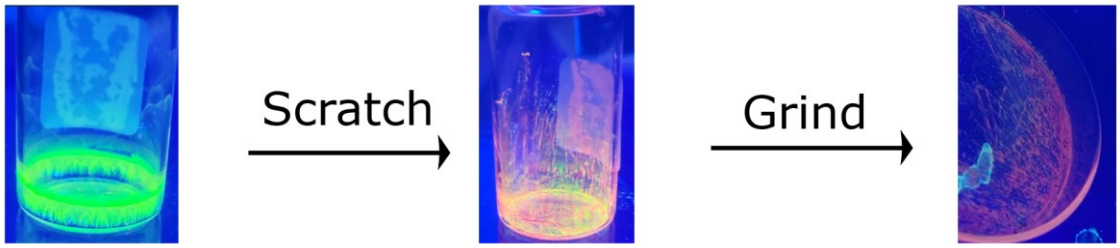

Figure 2.42: Emission change from green to orange when scratching $[C_{16}Me_3N]_2[Au_2(i\text{-}mnt)_2]$ crystals with the tip of a spatula; further grinding converts the material to a powder with a dark red emission at room temperature.

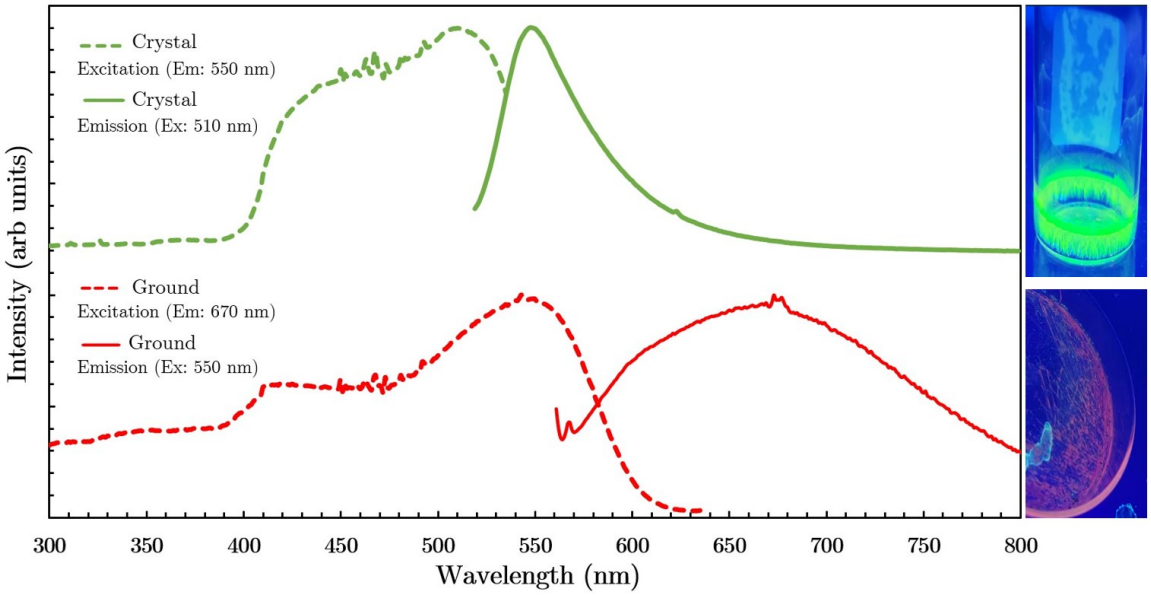

Figure 2.43: Excitation (dashed lines) and emission (solid lines) spectra of crystals $[C_{16}Me_3N]_2[Au_2(i\text{-}mnt)_2]$ (green), and ground $[C_{16}Me_3N]_2[Au_2(i\text{-}mnt)_2]$ (orange) at room temperature.

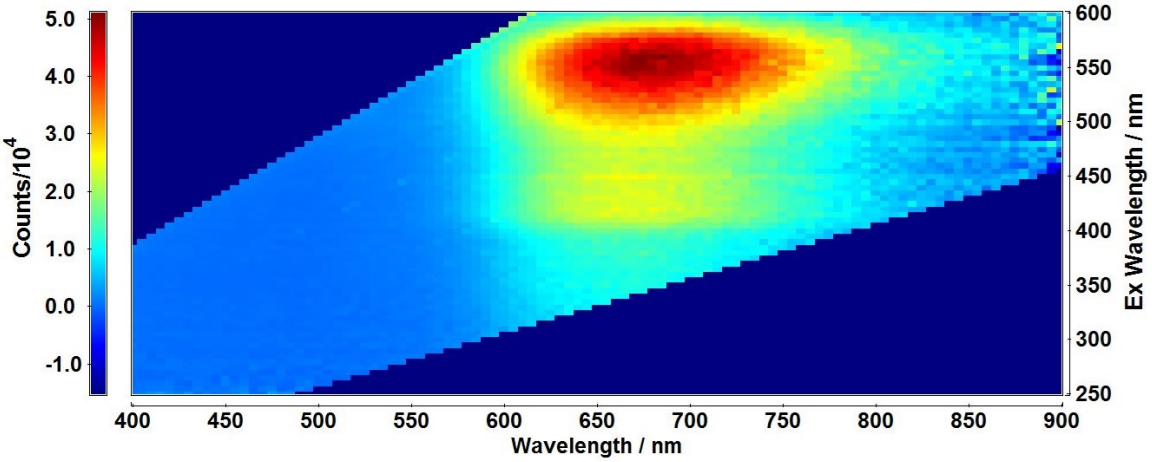

Figure 2.44. EEM spectrum of the ground $[C_{16}Me_3N]_2[Au_2(i\text{-mnt})_2]$ structure illustrates the broad emissive region at ca. 660 nm.

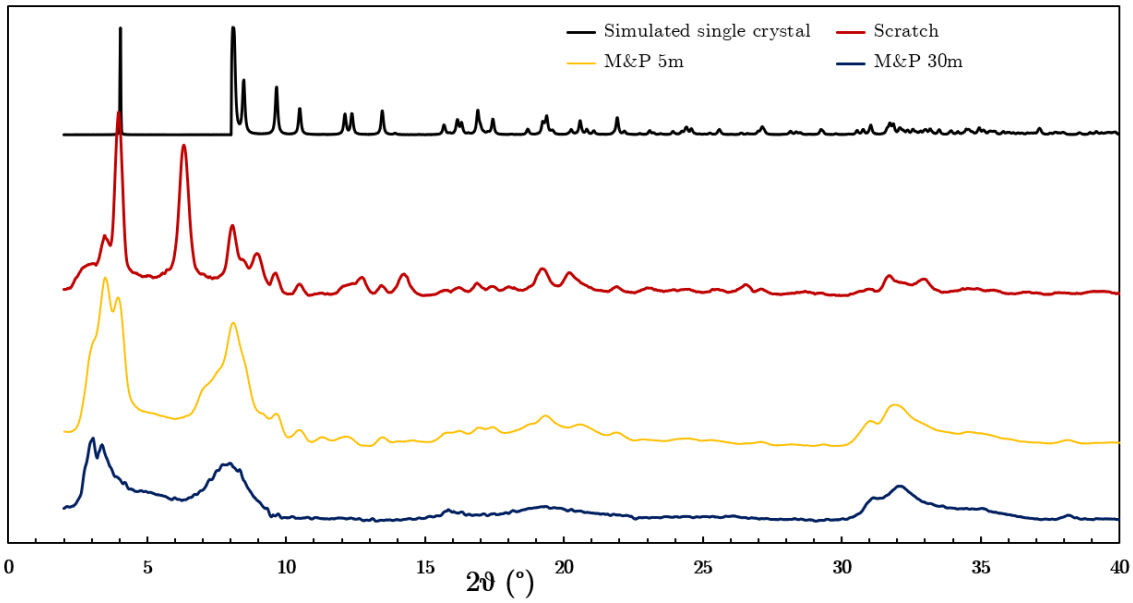

Figure 2.45: Powder X-Ray diffractograms of $[C_{16}Me_3N]_2[Au_2(i\text{-mnt})_2]$. Diffractogram generated from single crystal data (black), collected after applying mild pressure of a spatula tip (red), collected after grinding with mortar and pestle for 5 min (yellow), and after grinding for 30 min (blue).

The observed broadening of the peaks can be understood in term of the Scherrer formula, which can be employed to estimate the crystalline size of materials from the peak width in a diffraction pattern. The Scherrer formula can be summarized as $L = (K * \lambda) / (\beta * \cos(\theta))$ where L is average crystallite size, K is constant related to crystallite size, taken as 0.9, λ is the X – ray wavelength in nanometer, β is the full width at half maximum in

radians, and θ is Bragg's angle in radians. After grinding the crystals of $[C_{16}Me_3N]_2[Au_2(i\text{-}mnt)_2]$, peaks become broader and the crystalline size decreases.

In summary, grinding crystals of $[C_8Me_3N]_2[Au_2(i\text{-}mnt)_2]$ removes solvent that was trapped in the crystal lattice. Although it is still unclear why the $[C_{10}Me_3N]_2[Au_2(i\text{-}mnt)_2]$ system does not exhibit any change upon grinding, the consequence of grinding in general for $[C_4Me_3N]_2[Au_2(i\text{-}mnt)_2]$ and $[C_{16}Me_3N]_2[Au_2(i\text{-}mnt)_2]$ is to induce structural changes and a red-shift of the emission maxima, which can be related to applying pressure to aurophilic-containing systems.[99] Notably, the $[C_{16}Me_3N]_2[Au_2(i\text{-}mnt)_2]$ structure displays a high level of softness and a significant change in emission when applying mild pressure from a spatula tip, creating a new intermediate phase that exhibits red emission instead of the parent green-emission. This result is consistent with the hypothesis that the softness of materials could be further increased when combining softer cations, in this case a surfactant, to the already structurally-sensitive aurophilic-containing framework $[Au_2(i\text{-}mnt)_2]^{2-}$.

2.2.6. Conclusion

This chapter first explored how tetraalkylammonium cations further reinforced the idea that steric hindrance of the cations could disturb *inter*-aurophilic bond formation, whereby the $[Au_2(i\text{-}mnt)_2]^{2-}$ units would remain as structurally isolated gold(I) dimers. In addition, alkyl-trimethyl ammonium cations of the form $[RMe_3N]^+$ were utilized with the $[Au_2(i\text{-}mnt)_2]^{2-}$ building blocks, in order to examine their use as a tool to induce intermolecular aurophilic interactions between the dimers, impact the supramolecular structural morphology, and manifest mechanochromic behaviour as part of the investigation of using "soft" surfactant-style cations.

All $[Au_2(i\text{-}mnt)_2]^{2-}$ salts of the investigated $[RMe_3N]^+$ series formed intermolecular aurophilic interactions between anions to create 1D gold(I) chains. These cations are less bulky than the tetraalkylammonium cations, thus allowing propagation of the intermolecular aurophilic network. When looking beyond the 1-D gold(I) chains, they also assisted in the self-assembly of supramolecular packing structures. The resulting structures demonstrated intriguing differences of supramolecular packing and different luminescent profiles from only small changes in the length of alkyl chain C_n on $[RMe_3N]^+$

cations, suggesting that the system is indeed very responsive to small changes in the cation.

The idea that materials can be further mechanically softened using soft surfactant-type cations, specifically $[C_{16}Me_3N]^+$ in this case, was explored via mechanochromic properties. This combination of a surfactant-type cation and the sensitive Au-containing framework $[Au_2(i\text{-mnt})_2]^{2-}$ led to a more flexible structure, which in this case gave rise to a change from columnar to smectic C-like structures as the alkyl chain-length increased. The pronounced softness of $[C_{16}Me_3N]_2[Au_2(i\text{-mnt})_2]$ is also evident from a structural change, as applied pressure led to red-shifted emission. While there is no evidence of phase transition upon heating, we have displayed an example for enhancing the softness properties of coordination polymeric materials while maintaining the emissive properties inherent in the aurophilic interactions, by the incorporation of soft surfactant cations.

2.2.7. Experimental

2.2.7.1. General Procedures and Physical Measurements

All reactions were conducted under ambient atmospheric conditions. The synthesis of potassium iso-maleonitriledithiolate, $K_2(i\text{-mnt})$,[122] chloro(tetrahydrothiophene) gold(I), AuCl(tht),[123] and potassium gold(I) iso-maleonitriledithiolate, $K_2[Au_2(i\text{-mnt})_2]$,[106] were carried out according to literature procedures. All other reagents were purchased from commercial chemical vendors and used as received. Infrared spectra were measured on a Thermo Nicolet Nexus 670 FTIR equipped with a Pike MIRacle attenuated total reflection (ATR) sampling accessory (equipped with a germanium crystal, range 4000 – 700 cm^{-1}). Elemental microanalyses (% C, H, N, S) were performed by Dr. Wen Zhou and Carol Wu at Simon Fraser University on a Carlo Erba EA 1110 CHN elemental analyzer or a Thermo Fisher Scientific Flash*Smart* CHNS elemental analyzer respectively. Solid-state luminescence spectra were obtained on an Edinburgh FS5 Spectrofluorometer in a solid sample holder SC-15 (horizontal sample) using a xenon arc lamp. Experimental specifications were 1 nm excitation and 2 nm emission slit widths, 1 second dwell times, and 3 averaged scans per spectra. Solid-state quantum yield spectra were collected with the same instrument using the integrating sphere solid sample holder SC–30. Thermogravimetric analyses were performed by Dr. Wen Zhou on a PerkinElmer TGA 4000 using a heating rate of 2 °C min^{-1}. Phase transition temperatures and enthalpies

were probed using differential scanning calorimetry (DSC) on a DSC Q2000 instrument (TA Instruments) with a Refrigerated Cooling System 90 (TA Instruments). The rate of heating and cooling measurements was carried out at a rate of 10 °C/min. Optical microscopy experiments were carried out on an Olympus BX50 microscope equipped with a Linkam LTS350 heating stage.

2.2.7.2. X-Ray Crystallography

Single crystal and powder samples were secured to MiTeGen MicroMounts using paratone oil. All crystallographic data were obtained on a Bruker SMART Apex II Duo CCD diffractometer with TRIUMPH graphite-monochromated Mo Kα (λ= 0.71073 Å) radiation or a Cu Kα (λ = 1.54184 Å) Incoatec microsource. An Oxford Cryosystems Cryostream was used to cool and maintain a temperature of 220 K for $(C_4Me_3N)_2[Au_2(i\text{-mnt})_2]\cdot(MeCN)$, $(C_6Me_3N)_2[Au_2(i\text{-mnt})_2]$, and $(C_8Me_3N)_2[Au_2(i\text{-mnt})_2]$ crystals during data collection, while others were collected at room temperature. Power X-Ray diffraction data (PXRD) were recorded by performing data collection frames of total 3 individual φ 360° scans with a maximum 2θ value of approximately 60°.

All structures were solved using intrinsic phasing in APEX III[113] and subsequent refinements were performed in ShelxLe[114] and Olex2.[115] Diagrams were prepared using VESTA[116] showing isotropic and thermal ellipsoids drawn at 50% probability. Attempts to model disorder in the butyl chains of $(C_4Me_3N)_2[Au_2(i\text{-mnt})_2]$ could not completely resolve the chains, with many positional disorders present along the butyl chains, whereas the solvated analog $(C_4Me_3N)_2[Au_2(i\text{-mnt})_2]\cdot(MeCN)$ display nearly identical structural properties and crystallographic parameters, but without the disorder in the butyl chains. In addition, the crystal structure of $(C_6Me_3N)_2[Au_2(i\text{-mnt})_2]$ shows multiple disorder along the hexyl chains, was weakly diffracting even at low temperature and the crystals were twinned, hence the data quality was low. However, the crystallographic parameters of $(C_6Me_3N)_2[Au_2(i\text{-mnt})_2]$ salts were nearly identical through multiple different collections.

2.2.7.3. Syntheses

$[(C_7H_{15})_4N]_2[Au_2(i\text{-mnt})_2]$.

To a gently heated 10 mL solution of 1:1 H_2O:acetone of pre-dissolved $K_2[Au_2(i\text{-mnt})_2]$, (100 mg, 0.133 mmol), tetraheptylammonium iodide ($(C_7H_{15})_4NI$); (144 mg, 0.268 mmol) in 5 mL of acetone was added in one portion to form oily particles. The mixture was then

further concentrated until an orange solid formed, which was then washed 3 times with 5 mL of 1:1 EtOH:H_2O to remove KI and dried under vacuum overnight to obtain a bright orange powder. Yield: 128 mg (65%). Anal. Calcd. for $C_{64}H_{120}N_6S_4Au_2$: C 51.39%, H 8.09%, N 5.62%, S 8.57%. Found: C 50.92 %, H 8.15 %, N 5.70%, S 9.35 %. IR (ATR, cm^{-1}): 2955 (m), 2926 (s), 2857 (m), 2195 ($\nu_{C\equiv N}$, s), 1467 (m), 1354 (s), 1223 (m), 949 (w), 855 (w).

$[(C_8H_{17})_4N]_2[Au_2(i\text{-mnt})_2]$.

The synthesis of $[(C_8H_{17})_4N]_2[Au_2(i\text{-mnt})_2]$ was performed similarly to $[(C_7H_{15})_4N]_2[Au_2(i\text{-mnt})_2]$ but using tetra-octylammonium chloride. Yield: 118 mg (57%). Anal. Calcd. for $C_{72}H_{136}N_6S_4Au_2$: C 53.78 %, H 8.52 %, N 5.23 %, S 7.98 %. Found C 54.1 %, H 8.32 %, N 5.03 % , S 7.49 %. IR (ATR, cm^{-1}): 2955 (m), 2926 (s), 2855 (m), 2195 ($\nu_{C\equiv N}$, s), 1467 4(m), 1353 (s), 1223 (w), 949 (w), 855 (w).

$[(C_5H_{11})_4N]_2[Au_2(i\text{-mnt})_2]$.

The synthesis of $[(C_5H_{11})_4N]$ was performed similarly to $[(C_7H_{15})_4N]_2[Au_2(i\text{-mnt})_2]$ using tetra-pentylammonium chloride. Yield: 103 mg (54 %). Anal. Calcd. for $C_{48}H_{88}N_6S_4Au_2$: C 45.34 %, H 6.98 %, N 6.61% , S 10.09 %. Found C 44.83 %, H 7.15 %, N 6.83 % , S 10.53 %. Anal. Calcd. for $C_{48}H_{88}N_6S_4Au_2$ + 5% $K_2[Au_2(i\text{-mnt})_2]$: C 44.40 %, H 6.67 %, N 6.67%, S 10.35 %. IR (ATR, cm^{-1}): 2959 (m), 2931 (s), 2872 (m), 2190 ($\nu_{C\equiv N}$, s), 1468 (m), 1347 (s), 1222 (w), 949 (w), 856 (w).

$[C_4Me_3N]_2[Au_2(i\text{-mnt})_2]$.

To a gently heated 20 mL solution of 1:1 EtOH:H_2O of $K_2[Au_2(i\text{-mnt})_2]$ (100 mg, 0.133 mmol), butyltrimethylammonium chloride (C_4Me_3NCl) (45 mg, 0.297 mmol) in 5 mL of water was added in one portion. From the initial light orange solution, a bright yellow precipitate formed immediately, which was collected, washed with H_2O, and air-dried via vacuum filtration. Yield: 105 mg, 87%. This crude material was dissolved in a slightly heated solution of 1:2 toluene and acetonitrile and the solution was slowly evaporated under ambient conditions overnight to yield light orange needles of $[C_4Me_3N]_2[Au_2(i\text{-mnt})_2]$. Anal. Calcd. for $C_{22}H_{36}S_4N_6Au_2$: C 29.14 %, H 4.00 %, N 9.27 %, S 14.15%. Found: C 28.92 %, H 4.05 %, N 9.49 %, S 13.76%. IR (ATR, cm^{-1}): 2961 (m), 2873 (w), 2195 ($\nu_{C\equiv N}$, s), 1467 (m), 1357 ($\nu_{C=C}$, s), 1224 (w), 969 (w), 856 (w). $(C_4Me_3N)_2[Au_2(i\text{-mnt})_2]$ was

ground using mortar and pestle for 10 min. IR (ATR, cm^{-1}): 2961 (m), 2874 (w), 2195 ($\nu_{C\equiv N}$, s), 1462 (m), 1357 ($\nu_{C=C}$, s), 1224 (w), 969 (w), 857 (w).

$[C_4Me_3N]_2[Au_2(i\text{-}mnt)_2] \cdot (MeCN)$.

Crystals of $(C_4Me_3N)_2[Au_2(i\text{-}mnt)_2] \cdot (MeCN)$ suitable for single crystal X-ray diffraction were grown *via* vapour diffusion of MeOH into a saturated MeCN solution of $(C_4Me_3N)_2[Au_2(i\text{-}mnt)_2]$. IR (ATR, cm^{-1}): 2945 (m), 2883 (m), 2261 (w), 2198 ($\nu_{C\equiv N}$, w), 1451 (w), 1369 ($\nu_{C=C}$, w), 1026 (s), 971 (w). Elemental analysis could not be obtained due to the rapid desolvation of the crystals back to $(C_4Me_3N)_2[Au_2(i\text{-}mnt)_2]$.

$[C_8Me_3N]_2[Au_2(i\text{-}mnt)_2]$.

To a gently heated 20 mL solution of 1:1 EtOH:H_2O of $K_2[Au_2(i\text{-}mnt)_2]$ (100 mg, 0.133 mmol), octyltrimethylammonium chloride (C_8Me_3NCl) (62 mg, 0.298 mmol) in 5 mL of H_2O was added in one portion. From the initially light orange solution a dark red precipitate formed immediately, which was collected and washed thoroughly with 15 mL of cold 1:1 EtOH:H_2O and air-dried overnight via vacuum filtration. Yield: 101 mg, 74 %. Crystals of $[C_8Me_3N]_2[Au_2(i\text{-}mnt)_2]$ suitable for single crystal X-ray diffraction were grown *via* vapour diffusion of MeOH into a $[C_8Me_3N]_2[Au_2(i\text{-}mnt)_2]$ saturated MeCN solution. Anal. Calcd. for $C_{30}H_{52}S_4N_6Au_2$: C 35.36 %, H 5.14 %, N 8.25 %, S 12.59 %. Found: C 35.01 %, H 5.16 %, N 8.35 %, S 12.10 %. IR (ATR, cm^{-1}): 3222 (s), 2923 (m), 2856 (w), 2230 (s), 2193 ($\nu_{C\equiv N}$, s), 1469 (m), 1354 ($\nu_{C=C}$, s), 1223 (w), 968 (w), 857 (w). $(C_8Me_3N)_2[Au_2(i\text{-}mnt)_2]$ was ground using mortar and pestle for 10 min. IR (ATR, cm^{-1}): 2923 (m), 2856 (w), 2194 ($\nu_{C\equiv N}$, m), 1469 (m), 1354 ($\nu_{C=C}$, s), 1223 (w), 968 (w), 857 (w).

$[C_{10}Me_3N]_2[Au_2(i\text{-}mnt)_2]$.

To a gently heated 20 mL solution of 1:1 EtOH:H_2O of $K_2[Au_2(i\text{-}mnt)_2]$(100 mg, 0.133 mmol), decyltrimethylammonium bromide ($C_{10}Me_3NBr$) (76 mg, 0.271mmol) in 5 mL of EtOH was added in one portion. A dark red precipitate formed immediately, which was collected, washed thoroughly with 15 mL of cold 1:1 EtOH:H_2O and air-dried overnight in vacuum filtration. Yield: 119 mg, 84 %. The material was then dissolved in a slightly heated solution of 2 : 1 acetonitrile and acetone and the solution was slow evaporated under ambient conditions overnight to yield red needles of $[C_{10}Me_3N]_2[Au_2(i\text{-}mnt)_2]$. Anal. Calcd. for $C_{34}H_{60}S_4N_6Au_2$: C 37.98 %, H 5.63 %, N 7.82 %, S 11.93 %. Found: C 37.84 %, H 5.71

%, N 7.45 %, S 12.61%. IR (ATR, cm^{-1}): 2956 (w), 2921 (m), 2850 (w), 2193 ($\nu_{C\equiv N}$, s), 1475 (w), 1352 ($\nu_{C=C}$, s), 1224 (w), 958 (w), 858 (w).

$[C_{16}Me_3N]_2[Au_2(i\text{-mnt})_2]$.

To a gently heated 20 mL solution of 1:1 EtOH:H_2O of $K_2[Au_2(i\text{-mnt})_2]$ (100 mg, 0.133 mmol), cetyltrimethylammonium bromide ($C_{16}Me_3NBr$) (100 mg, 0.274 mmol) in 5 mL of EtOH was added. From the initially light orange solution a green precipitate formed immediately, which was collected and washed thoroughly with 15 mL of cold 1:1 EtOH:H_2O and air-dried via vacuum filtration. Yield: 126 mg, 76 %. The material was then dissolved in a slightly heated solution of 1 : 1 of acetonitrile and acetone and this solution was slow evaporated under ambient conditions overnight to yield green needles of $[C_{16}Me_3N]_2[Au_2(i\text{-mnt})_2]$. Anal. Calcd. for $C_{46}H_{84}N_6S_4Au_2$: C 44.43 %, H 6.81 %, N 6.76 %, S 10.32 %. Found: C 44.78 %, H 6.86 %, N 6.82 %, S 10.70 %. IR (ATR, cm^{-1}): 2919 (s), 2851 (m), 2197 ($\nu_{C\equiv N}$, s), 1468 (w), 1356 ($\nu_{C=C}$, s), 1226 (w), 960 (w), 857 (w). $(C_{16}Me_3N)_2[Au_2(i\text{-mnt})_2]$ was ground using mortar and pestle for 30 minutes, generating a red emissive material. IR (ATR, cm^{-1}): 2921 (s), 2852 (m), 2197 ($\nu_{C\equiv N}$, s), 1468 (m), 1353 ($\nu_{C=C}$, s), 1226 (w), 959 (w), 857 (w).

$[(C_6H_{13})_4N][Au^{III}(i\text{-mnt})_2]$

A few crystals of the gold(III) analog $[(C_6H_{13})_4N][Au^{III}(i\text{-mnt})_2]$ were collected through an attempt to grow $[(C_6H_{13})_4N]_2[Au^{I}_2(i\text{-mnt})_2]$ crystals via slow evaporation of an *i*-PrOH:MeCN mixture containing pre-dissolved $[(C_6H_{13})_4N]_2[Au_2(i\text{-mnt})_2]$. No other analytical data was obtained.

$[C_{12}Me_3N][Au^{III}(i\text{-mnt})_2]$

A few crystals of the gold(III) analog were collected through an attempt to grow $[C_{12}Me_3N]_2[Au^{I}_2(i\text{-mnt})_2]$ crystals via slow evaporation of a MeCN:EtOH mixture containing pre-dissolved $[C_{12}Me_3N]_2[Au^{I}_2(i\text{-mnt})_2]$. No other analytical data was obtained.

Chapter 3. Future Project and Conclusion

The goal of this thesis was primarily to explore and design tunable photoluminescent properties by utilizing aurophilicity in gold(I) coordination polymers and alkyl trimethylammonium cations $[RMe_3N]^+$ and how a simple change in R-alkyl length could alter the overall supramolecular packing and photoluminescence. In addition, we also explored if the softness of surfactant cations could be translated to induce external stimuli-responsive properties, in this case in the form of mechanochromism. This final chapter gives an overall outlook from the work in Chapter 2 and suggests potential future projects with some preliminary results to that end.

3.1. Branched Long Alkyl Chains as Next Generation Cations for Improved Mechanical Softness

The next step for this project is to examine whether improved morphological softness can be created by combining even softer, long-alkyl chain cations: the most straightforward alteration to this end is using branched alkyl chain structures. While these cations are harder to access commercially and might require another synthetic step, the idea is to incorporate a branched alkyl chain instead of the already utilized linear alkyl chains, which in theory should make the cations even softer by impeding close packing between molecules. An example of one potential cation is shown in Figure 3.1.

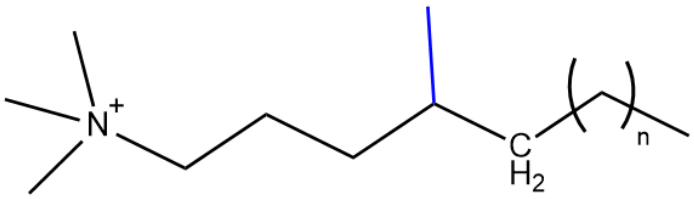

Figure 3.1: Long alkyl chain with a methyl branch on a trimethylammonium cation.

Other cations that we could investigate that might yield similar results as described previously are the dialkyl dimethylammonium cation family, i.e., $[R_2Me_2N]^+$, where the alkyl groups are long chains (Figure 3.2). Some preliminary results using the didecyl dimethylammonium cation with $[Au_2(i\text{-mnt})_2]^{2-}$ show that this material has the tendency to form fiber-like textures during crystal-growth, and these fiber-like crystals emit a bright red

colour under a UV lamp. No structural information has been obtained to date on this new series of materials.

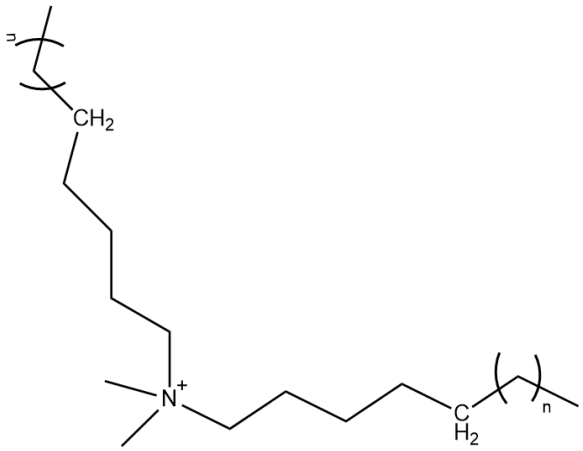

Figure 3.2**:** Dialkyl dimethylammonium cations as another example for engineering emissive and soft frameworks.

3.2. Quaternary Alkyl Pyridinium Units as Soft Self-Assembling Cations

To better understand how long aromatic systems containing long alkyl chains would influence the framework compared to the alkylammonium series, quaternary ammonium like alkylpyridinium cations that possess long alkyl chains could be employed to promote structural changes under external stimuli (Figure 3.3). By nature, many of these cations are components of ionic liquids, similar to the imidazolium series of cations (see below), which suggests that they could also be harnessed to soften materials to induce phase transitions. Furthermore, given the possibility of π interactions in the cationic aromatic system that could modulate the formation of aurophilic bonds between anions and tunability of luminescence that could occur from a small change in the length of the alkyl chain, alkylpyridinium cations are also a promising building block for exploration.

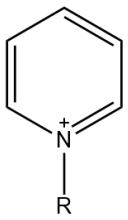

Figure 3.3: Alkylpyridinium cations where R is the long alkyl chains.

3.3. Symmetrical Alkyl Imidazolium Units as Ionic Liquid Cations

Similarly to the alkyl pyridinium, alkyl imidazolium cation families are often key components of ionic liquids, which are salts that exist in the liquid state at low temperature depending on the anion that the imidazolium cation is paired with. These ionic liquids are less organized compared to more orderly crystalline solids and have been widely used in soft functional materials. An example of an imidazolium cation is the symmetrical imidazolium $[R_2(imi)]^+$, where the R group is an alkyl chain that bonds directly to the nitrogen atoms; these symmetric versions are more commercially accessible than the unsymmetrical form. In addition, given the small size and less steric hindrance than the $[n\text{-}Bu_4N]^+$ cation, it can also support the generation of a 1-D aurophilic network of $[Au_2(i\text{-}mnt)_2]^{2-}$ units, as seen in the crystal structures of $[Me_2(imi)]_2[Au_2(i\text{-}mnt)_2]$ (Figure 3.4) and $[i\text{-}Pr_2(imi)]_2[Au_2(i\text{-}mnt)_2]$ (Figure 3.5), both of which are preliminary results from this series that are reported herein as guides for future work.

The structure of $[Me_2(imi)]_2[Au_2(i\text{-}mnt)_2]$ displays a kinked 1-D gold(I) chain with a Au-Au-Au angle of 168° and adopts a highly twisted conformation around the *i*-mnt ligand, with C-S-S-C torsional angles of 40.3(14)° and 25.9(15)°. Similarly, the structure of $[i\text{-}Pr_2(imi)]_2[Au_2(i\text{-}mnt)_2]$ also prompts intermolecular aurophilic interactions between $[Au_2(i\text{-}mnt)_2]^{2-}$ anions to produce a 1-D gold(I) chain and also exhibits a highly twisted i-mnt conformation, with C-S-S-C torsional angles of 18.8(7) and 60.3(13)°. The supramolecular packing of $[i\text{-}Pr_2(imi)]_2[Au_2(i\text{-}mnt)_2]$ resembles more of a pseudo-hexagonal structure when observed along the *c*-axis, whereas due to the kinked 1-D gold(I) chain, the $[Me_2(imi)]_2[Au_2(i\text{-}mnt)_2]$ represents a distorted view of a more tetragonal columnar packing.

Interestingly, when examining a bulkier aromatic imidazolium cation, in this case the 1,3,5-bis(trimethyl)diphenyl imidazolium,$[(Me_3Ph)_2(imi)]^+$ system, the crystal-growth process yields particularly well-formed crystals. SC-XRD reveals the presence of a 1-D aurophilic chain with an Au-Au-Au angle of 175.4(2)°, a flatter conformation of the *i*-mnt ligand more similar to the structure of $[C_{16}Me_3N]_2[Au_2(i\text{-}mnt)_2]$, with a C-S-S-C angle of 4.2(4)° and an intermolecular Au(I) – Au(I) distance of 3.0677(6) Å (Figure 3.6a), which is similar to the distances of 2.9431(18) and 2.9481(4) Å in $[Me_2(imi)]_2[Au_2(i\text{-}mnt)_2]$ and $[i\text{-}Pr_2(imi)]_2[Au_2(i\text{-}mnt)_2]$ respectively. The supramolecular structure shows a pseudo-hexagonal packing with the cations filling up the space between each column of gold(I)

chains (Figure 3.6b). Photoluminescent properties indicate a similar green emission to $[C_{16}Me_3N]_2[Au_2(i\text{-mnt})_2]$ at λ_{max} = 560 nm. These preliminary results show that when working with the $[Au_2(i\text{-mnt})_2]^{2-}$ unit using small cations, which include the $[C_4Me_3N]^+$, $[Me_2(imi)]^+$ and $[i\text{-}Pr_2(imi)]^+$ cations, the $[Au_2(i\text{-mnt})_2]^{2-}$ unit typically adopts a twisted conformation and as the cations get bulkier with $[C_{16}Me_3N]^+$ and $[(Me_3Ph)_2(imi)]^+$ units as examples, the $[Au_2(i\text{-mnt})_2]^{2-}$ unit exhibits a flatter conformation, as indicated by smaller C-S-S-C torsional angles. These flatter conformations also share a similar green emission compared to the orange-red colour shown with other cations. While this is only based off observations of limited structural profiles, it is worthwhile to keep this in mind when working with other series of cations on $[Au_2(i\text{-mnt})_2]^{2-}$ anions.

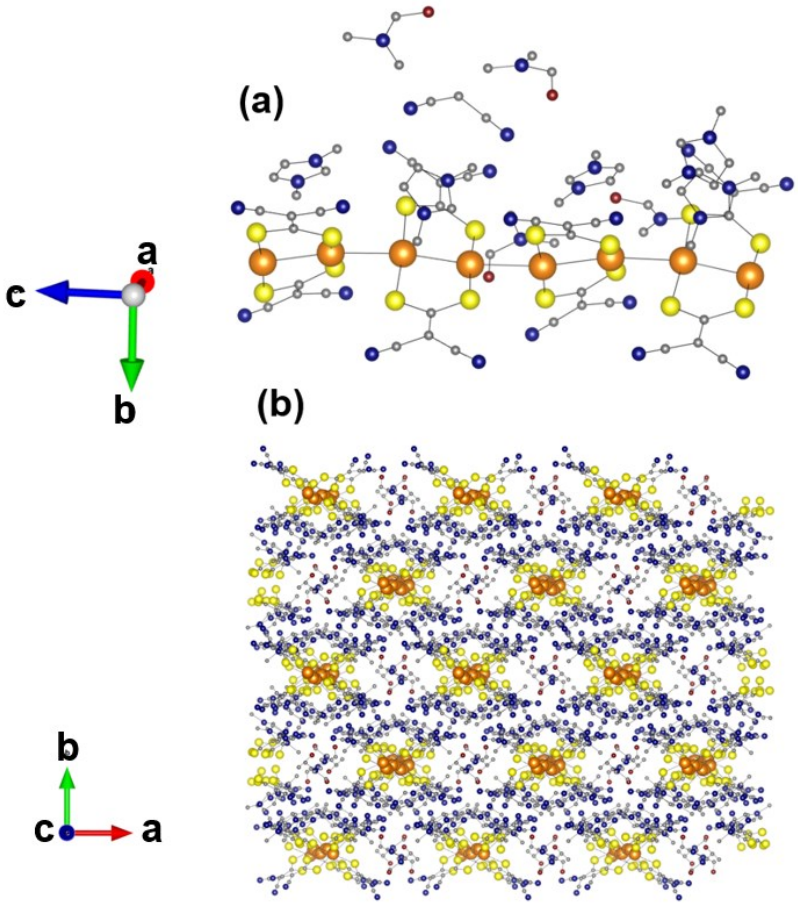

Figure 3.4: Crystal structure of $[Me_2(imi)]_2[Au_2(i\text{-mnt})_2]$ (a) solvated form with dimethylformamide (DMF) and a kinked 1-D gold(I) chain with intermolecular Au(I) – Au(I) distance of 2.9431(18) Å and a Au – Au – Au angle of 168° and (b) supramolecular packing when viewed down the *c*-axis.

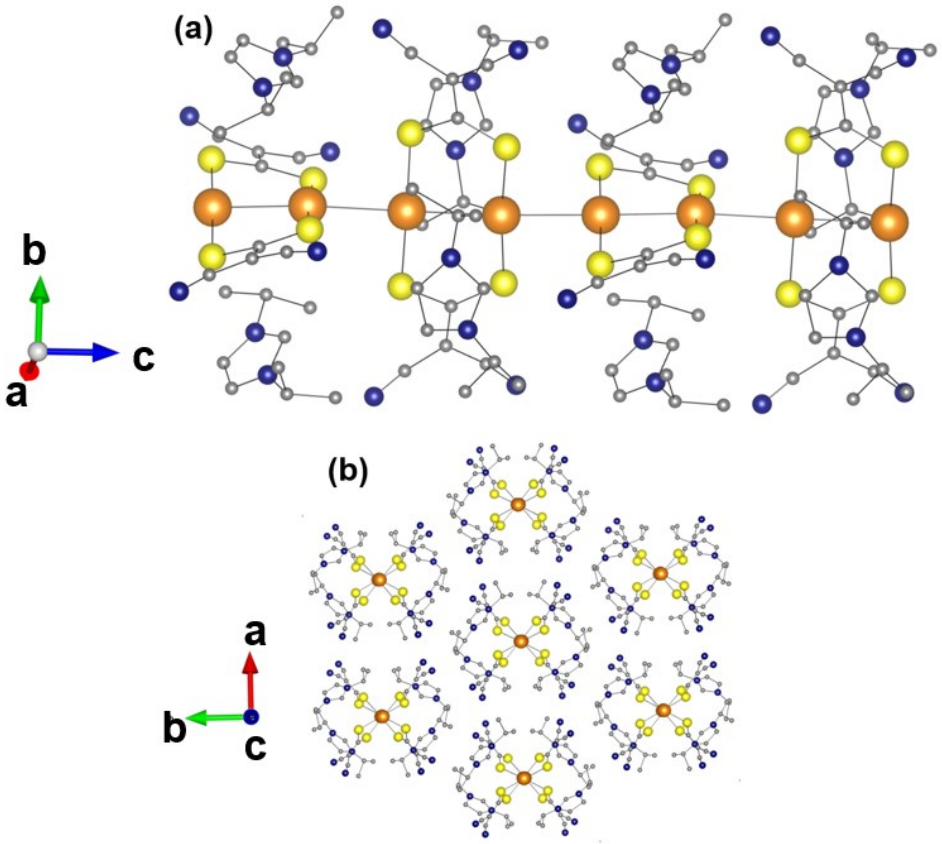

Figure 3.5: Crystal structure of [*i*-Pr_2(*imi*)]$_2$[Au_2(*i*-mnt)$_2$] illustrates (a) a 1-D gold(I) chain with an intermolecular Au(I) – Au(I) distance of 2.9481(4) Å and a Au – Au – Au angle of 175.8° and (b) pseudo-hexagonal closed packing when looking down the gold(I) chain.

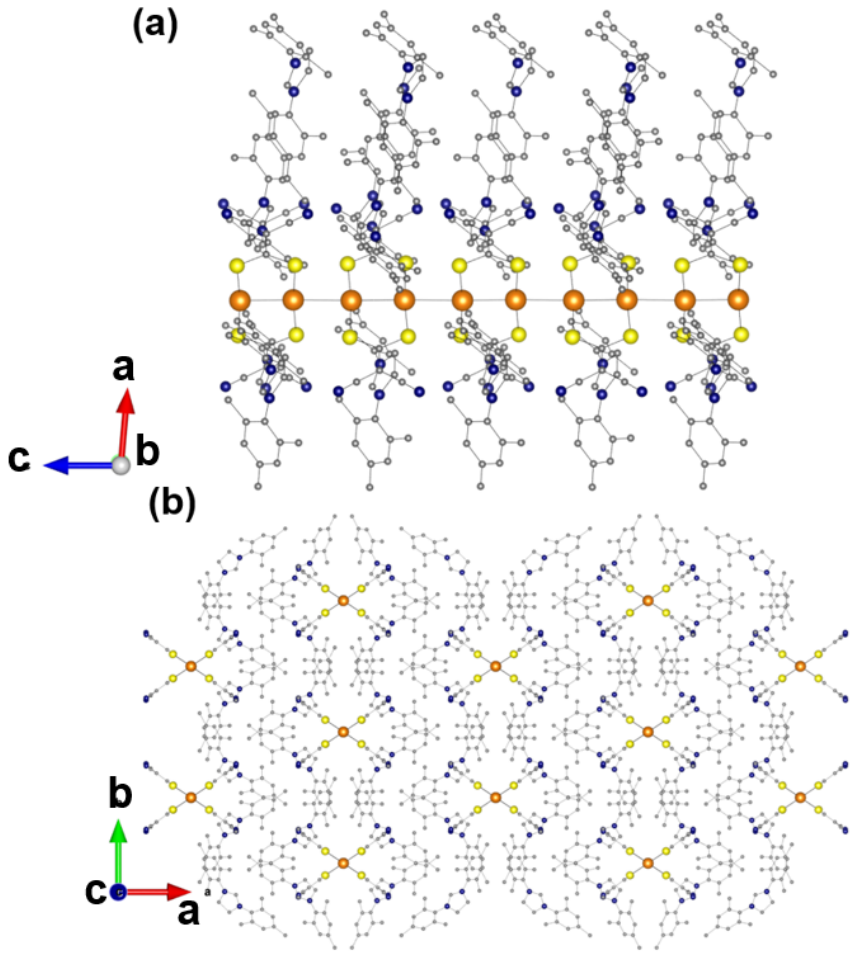

Figure 3.6: Crystal structure of $[(Me_3Ph)_2(imi)]_2[Au_2(i\text{-}mnt)_2]$ (a) 1-D gold(I) chain with an intermolecular Au(I) – Au(I) distance of 3.0677(6) Å and a Au – Au – Au angle of 175.4(2)° and (b) pseudo-hexagonal packing with the cations filled in between the cavity of the gold(I) column when looking down the gold(I) chain.

3.4. Global conclusion

What is the future for the $[Au_2(i\text{-}mnt)_2]^{2-}$ building block? All suggested projects above are only among the very few lists of potential avenues that researchers could utilize with emissive aurophilic-based materials in general and gold(I) dimers such as $[Au_2(i\text{-}mnt)_2]^{2-}$ in particular. In Chapter 2, we have shown a strategy that cations containing long alkyl chain $[RMe_3N]^+$ could assist in the self-assembling of supramolecular architectures and induce mechanochromic properties in addition to its tunable photoluminescent profile. State-of-the-art computational chemistry can be accompanied in addition to experimental data to further dissect the complicated nature of aurophilicity. There are many transition

metal cations and ‘soft’ organic cations (e.g., surfactants, ionic liquid cations, etc.) that can be incorporated into $[Au_2(i\text{-mnt})_2]^{2-}$ and other gold(I) dithiolate-type coordination polymers to construct emissive materials with useful chemosensing and other stimuli-responsive applications toward pressure, solvents or metal ion detection, and temperature.

References

1. Braga, D.; Grepioni, F.; Making crystals by design: methods, techniques and applications, ed. Wiley-VCH: Weinheim, **2007**.

2. Mukherjee, S.; Zaworotko, M. J. Crystal Engineering of Hybrid Coordination Networks: From Form to Function. Trends Chem. **2020**, 2 (6), 506–518. DOI: 10.1016/j.trechm.2020.02.013.

3. Perry Iv, J. J.; Perman, J. A.; Zaworotko, M. J. Design and Synthesis of Metal–Organic Frameworks Using Metal–Organic Polyhedra as Supermolecular Building Blocks. Chem. Soc. Rev. **2009**, 38 (5), 1400. DOI: 10.1039/b807086p.

4. Batten, S. R.; Champness, N. R.; Chen, X.-M.; Garcia-Martinez, J.; Kitagawa, S.; Öhrström, L.; O'Keeffe, M.; Paik Suh, M.; Reedijk, J. Terminology of Metal–Organic Frameworks and Coordination Polymers (IUPAC Recommendations 2013). Pure Appl. Chem. **2013**, 85 (8), 1715–1724. DOI: 10.1351/PAC-REC-12-11-20.

5. Thompson, J. R. Designing Birefringent Materials: A Crystal Engineering Approach. Ph.D. Dissertation, Simon Fraser University, 8888 University Drive, Burnaby, B.C. Canada, V5A 1S6, **2017**.

6. Li, B.; Wen, H.-M.; Cui, Y.; Qian, G.; Chen, B. Multifunctional Lanthanide Coordination Polymers. Prog. Polym. Sci. **2015**, 48, 40–84. DOI: 10.1016/j.progpolymsci.2015.04.008.

7. Bünzli, J.-C. G. Review: Lanthanide Coordination Chemistry: From Old Concepts to Coordination Polymers. J. Coord. Chem. **2014**, 67 (23–24), 3706–3733. DOI: 10.1080/00958972.2014.957201.

8. Loukopoulos, E.; Kostakis, G. E. Review: Recent Advances of One-Dimensional Coordination Polymers as Catalysts. J. Coord. Chem. **2018**, 71 (3), 371–410. DOI: 10.1080/00958972.2018.1439163.

9. Bu, F.-X.; Hu, M.; Xu, L.; Meng, Q.; Mao, G.-Y.; Jiang, D.-M.; Jiang, J.-S. Coordination Polymers for Catalysis: Enhancement of Catalytic Activity through Hierarchical Structuring. Chem. Commun. **2014**, 50 (62), 8543–8546. DOI: 10.1039/C4CC02909G.

10. Gu, Y.; Zheng, J.; Otake, K.; Shivanna, M.; Sakaki, S.; Yoshino, H.; Ohba, M.; Kawaguchi, S.; Wang, Y.; Li, F.; Kitagawa, S. Host–Guest Interaction Modulation in Porous Coordination Polymers for Inverse Selective CO_2/C_2H_2 Separation. Angew. Chem. Int. Ed. **2021**, 60 (21), 11688–11694. DOI: 10.1002/anie.202016673.

11. Wu, P.; Li, Y.; Zheng, J.-J.; Hosono, N.; Otake, K.; Wang, J.; Liu, Y.; Xia, L.; Jiang, M.; Sakaki, S.; Kitagawa, S. Carbon Dioxide Capture and Efficient Fixation in a Dynamic Porous Coordination Polymer. Nat. Commun. **2019**, 10 (1), 4362. DOI: 10.1038/s41467-019-12414-z.

12. Qin, T.; Zhang, X.; Li, D.; Dong, X.; Qi, N.; Shang, Y.; Sakiyamad, H.; Afzal, M.; Alarifi, A. Temperature Modulation on Functional Coordination Polymers with Tetracarboxylate Linker: Syntheses, Structural Traits, and Magnetism. J. Mol. Struct. **2023**, 1291, 136074. DOI: 10.1016/j.molstruc.2023.136074.

13. Feng, X.; Shang, Y.; Zhang, H.; Li, R.; Wang, W.; Zhang, D.; Wang, L.; Li, Z. Enhanced Luminescence and Tunable Magnetic Properties of Lanthanide Coordination Polymers Based on Fluorine Substitution and Phenanthroline Ligand. RSC Adv. **2019**, 9 (29), 16328–16338. DOI: 10.1039/C9RA01574D.

14. Sutar, P.; Maji, T. K. Coordination Polymer Gels: Soft Metal–Organic Supramolecular Materials and Versatile Applications. Chem. Commun. **2016**, 52 (52), 8055–8074. DOI: 10.1039/C6CC01955B.

15. Engel, E. R.; Scott, J. L. Advances in the Green Chemistry of Coordination Polymer Materials. Green Chem. **2020**, 22 (12), 3693–3715. DOI: 10.1039/D0GC01074J.

16. Wu, W.; Sun, J.; Ji, S.; Wu, W.; Zhao, J.; Guo, H. Tuning the Emissive Triplet Excited States of Platinum(Ii) Schiff Base Complexes with Pyrene, and Application for Luminescent Oxygen Sensing and Triplet–Triplet-Annihilation Based Upconversions. Dalton Trans. **2011**, 40 (43), 11550. DOI: 10.1039/c1dt11001b.

17. Chen, J.; Yi, F.-Y.; Yu, H.; Jiao, S.; Pang, G.; Sun, Z.-M. Fast Response and Highly Selective Sensing of Amine Vapors Using a Luminescent Coordination Polymer. Chem. Commun. **2014**, 50 (72), 10506–10509. DOI: 10.1039/C4CC04614E.

18. Lustig, W. P.; Mukherjee, S.; Rudd, N. D.; Desai, A. V.; Li, J.; Ghosh, S. K. Metal–Organic Frameworks: Functional Luminescent and Photonic Materials for Sensing Applications. Chem. Soc. Rev. **2017**, 46 (11), 3242–3285. DOI: 10.1039/C6CS00930A.

19. Okutani, K.; Nozaki, K.; Iwamura, M. Specific Chiral Sensing of Amino Acids Using Induced Circularly Polarized Luminescence of Bis(Diimine)Dicarboxylic Acid Europium(III) Complexes. Inorg. Chem. **2014**, 53 (11), 5527–5537. DOI: 10.1021/ic500196m.

20. Tan, H.; Ma, C.; Gao, L.; Li, Q.; Song, Y.; Xu, F.; Wang, T.; Wang, L. Metal–Organic Framework-Derived Copper Nanoparticle Carbon Nanocomposites as Peroxidase Mimics for Colorimetric Sensing of Ascorbic Acid. Chem. Eur. J. **2014**, 20 (49), 16377–16383. DOI: 10.1002/chem.201404960.

21. Dou, Z.; Yu, J.; Cui, Y.; Yang, Y.; Wang, Z.; Yang, D.; Qian, G. Luminescent Metal–Organic Framework Films As Highly Sensitive and Fast-Response Oxygen Sensors. J. Am. Chem. Soc. **2014**, 136 (15), 5527–5530. DOI: 10.1021/ja411224j.

22. Aakeröy, C. B.; Champness, N. R.; Janiak, C. Recent Advances in Crystal Engineering. CrystEngComm. **2010**, 12 (1), 22–43. DOI: 10.1039/B919819A.

23. Hoskins, B. F.; Robson, R. Infinite Polymeric Frameworks Consisting of Three Dimensionally Linked Rod-like Segments. J. Am. Chem. Soc. **1989**, 111 (15), 5962–5964. DOI: 10.1021/ja00197a079.

24. Venkataraman, D.; Lee, S.; Moore, J. S.; Zhang, P.; Hirsch, K. A.; Gardner, G. B.; Covey, A. C.; Prentice, C. L. Coordination Networks Based on Multitopic Ligands and Silver(I) Salts: A Study of Network Connectivity and Topology as a Function of Counterion. Chem. Mater. **1996**, 8 (8), 2030–2040. DOI: 10.1021/cm950594i.

25. Fujita, M.; Tominaga, M.; Hori, A.; Therrien, B. Coordination Assemblies from a Pd(II)-Cornered Square Complex. Acc. Chem. Res. **2005**, 38 (4), 369–378. DOI: 10.1021/ar040153h.

26. Yaghi, O. M.; O'Keeffe, M.; Ockwig, N. W.; Chae, H. K.; Eddaoudi, M.; Kim, J. Reticular Synthesis and the Design of New Materials. Nature **2003**, 423 (6941), 705–714. DOI: 10.1038/nature01650.

27. Carlucci, L.; Ciani, G.; Proserpio, D. M. Polycatenation, Polythreading and Polyknotting in Coordination Network Chemistry. Coord. Chem. Rev. **2003**, 246 (1–2), 247–289. DOI: 10.1016/S0010-8545(03)00126-7.

28. Girolami, G. S. X-Ray Crystallography; University Science Books: New York, **2015**.

29. Dhanaraj, G.; Byrappa, K.; Prasad, V.; Dudley, M. Crystal Growth Techniques and Characterization: An Overview; Springer Handbooks, **2010**.

30. Stock, N.; Biswas, S. Synthesis of Metal-Organic Frameworks (MOFs): Routes to Various MOF Topologies, Morphologies, and Composites. Chem. Rev. **2012**, 112 (2), 933–969. DOI: 10.1021/cr200304e.

31. Dominelli, B.; Correia, J. D. G.; Kühn, F. E. Medicinal Applications of Gold(I/III)-Based Complexes Bearing N-Heterocyclic Carbene and Phosphine Ligands. J. Organomet. Chem. **2018**, 866, 153–164. DOI: 10.1016/j.jorganchem.2018.04.023.

32. Bond, G. C.; Thompson, D. T. Gold-Catalysed Oxidation of Carbon Monoxide. Gold Bull. **2000**, 33 (2), 41–50. DOI: 10.1007/BF03216579.

33. Zhu, B.; Gong, S.; Cheng, W. Softening Gold for Elastronics. Chem. Soc. Rev. **2019**, 48 (6), 1668–1711. DOI: 10.1039/C8CS00609A.

34. Kumar, D.; Saini, N.; Jain, N.; Sareen, R.; Pandit, V. Gold Nanoparticles: An Era in Bionanotechnology. Expert Opin. Drug. Deliv. **2013**, 10 (3), 397–409. DOI: 10.1517/17425247.2013.749854.

35. He, X.; Yam, V. W.-W. Luminescent Gold(I) Complexes for Chemosensing. Coord. Chem. Rev. **2011**, 255 (17–18), 2111–2123. DOI: 10.1016/j.ccr.2011.02.003.

36. Scherbaum, F.; Grohmann, A.; Müller, G.; Schmidbaur, H. Synthesis, Structure, and Bonding of the Cation $[\{(C_6H_5)_3PAu\}_5C]^+$. Angew. Chem. Int. Ed. Engl. **1989**, 28 (4), 463–465. DOI: 10.1002/anie.198904631.

37. Seifert, T. P.; Naina, V. R.; Feuerstein, T. J.; Knöfel, N. D.; Roesky, P. W. Molecular Gold Strings: Aurophilicity, Luminescence and Structure–Property Correlations. Nanoscale **2020**, 12 (39), 20065–20088. DOI: 10.1039/D0NR04748A.

38. Schmidbaur, H.; Schier, A. A Briefing on Aurophilicity. Chem. Soc. Rev. **2008**, 37 (9), 1931. DOI: 10.1039/b708845k.

39. Schmidbaur, H.; Schier, A. Aurophilic Interactions as a Subject of Current Research: An up-date. Chem. Soc. Rev. **2012**, 41 (1), 370–412. DOI: 10.1039/C1CS15182G.

40. Puddephatt, R. J. Macrocycles, Catenanes, Oligomers and Polymers in Gold Chemistry. Chem. Soc. Rev. **2008**, 37 (9), 2012. DOI: 10.1039/b708622a

41. Gimeno, M. C.; Laguna, A. Chalcogenide Centred Gold Complexes. Chem. Soc. Rev. **2008**, 37 (9), 1952. DOI: 10.1039/b708618k.

42. Fackler, J. P. Forty-Five Years of Chemical Discovery Including a Golden Quarter-Century. Inorg. Chem. **2002**, 41 (26), 6959–6972. DOI: 10.1021/ic025734m.

43. Katz, M. J.; Sakai, K.; Leznoff, D. B. The Use of Aurophilic and Other Metal–Metal Interactions as Crystal Engineering Design Elements to Increase Structural Dimensionality. Chem. Soc. Rev. **2008**, 37 (9), 1884. DOI: 10.1039/b709061g.

44. Pyykkö, P. Theoretical Chemistry of Gold. Angew. Chem. Int. Ed. **2004**, 43 (34), 4412–4456. DOI: 10.1002/anie.200300624.

45. Bardají, M.; Laguna, A. Gold Chemistry: The Aurophilic Attraction. J. Chem. Educ. **1999**, 76 (2), 201. DOI: 10.1021/ed076p201.

46. Calvo, F.; Pahl, E.; Wormit, M.; Schwerdtfeger, P. Evidence for Low-Temperature Melting of Mercury Owing to Relativity. Angew. Chem. Int. Ed. **2013**, 52 (29), 7583–7585. DOI: 10.1002/anie.201302742.

47. Chernyshev, A. N.; Chernysheva, M. V.; Hirva, P.; Kukushkin, V. Yu.; Haukka, M. Weak Aurophilic Interactions in a Series of Au(III) Double Salts. Dalton Trans. **2015**, 44 (32), 14523–14531. DOI: 10.1039/C4DT03167A.

48. Che, C.; Lai, S. Luminescence and Photophysics of Gold Complexes. In Gold Chemistry; Wiley, **2009**; pp 249–281. DOI: 10.1002/9783527626724.ch5.

49. Leznoff, D. B.; Xue, B.-Y.; Batchelor, R. J.; Einstein, F. W. B.; Patrick, B. O. Gold−Gold Interactions as Crystal Engineering Design Elements in Heterobimetallic Coordination Polymers. Inorg. Chem. **2001**, 40 (23), 6026–6034. DOI: 10.1021/ic010756e.

50. Ovens, J. S.; Truong, K. N.; Leznoff, D. B. Structural Organization and Dimensionality at the Hands of Weak Intermolecular Au···Au, Au···X and X···X (X = Cl, Br, I) Interactions. Dalton Trans. **2012**, 41 (4), 1345–1351. DOI: 10.1039/C1DT11741F.

51. Ovens, J. S.; Truong, K. N.; Leznoff, D. B. Targeting $[AuCl_2(CN)_2]^-$ Units as Halophilic Building Blocks in Coordination Polymers. Inorganica Chim. Acta **2013**, 403, 127–135. DOI: 10.1016/j.ica.2013.02.011.

52. Leznoff, D. B.; Xue, B.-Y.; Stevens, C. L.; Storr, A.; Thompson, R. C.; Patrick, B. O. Synthesis, Structure and Magnetic Properties of 3D Interpenetrating Nets of M(Pyrazine)$[Au(CN)]_2$ (M=Cu, Ni, Co) Supported by Aurophilic Interactions. Polyhedron **2001**, 20 (11–14), 1247–1254. DOI: 10.1016/S0277-5387(01)00601-5.

53. Leznoff, D. B.; Xue, B.-Y.; Patrick, B. O.; Sanchez, V.; Thompson, R. C. An Aurophilicity-Determined 3-D Bimetallic Coordination Polymer: Using $[Au(CN)_2]^-$ to Increase Structural Dimensionality through Gold···Gold Bonds in (Tmeda)Cu$[Au(CN)_2]_2$. Chem. Commun. **2001**, No. 3, 259–260. DOI: 10.1039/b007342n.

54. Shorrock, C. J.; Xue, B.-Y.; Kim, P. B.; Batchelor, R. J.; Patrick, B. O.; Leznoff, D. B. Heterobimetallic Coordination Polymers Incorporating $[M(CN)_2]^-$ (M = Cu, Ag) and $[Ag_2(CN)_3]^-$ Units: Increasing Structural Dimensionality via M−M‘ and M···NC Interactions. Inorg. Chem. **2002**, 41 (25), 6743–6753. DOI: 10.1021/ic025850p.

55. Leznoff, D. B.; Lefebvre, J. Coordination Polymers with Cyanoaurate Building Blocks: Potential New Industrial Applications for Gold. Gold Bull. **2005**, 38, 47–54. DOI: 10.1007/BF03215233

56. Lefebvre, J.; Tyagi, P.; Trudel, S.; Pacradouni, V.; Kaiser, C.; Sonier, J. E.; Leznoff, D. B. Magnetic Frustration and Spin Disorder in Isostructural M(μ-$OH_2)_2[Au(CN)_2]_2$ (M = Mn, Fe, Co) Coordination Polymers Containing Double Aqua-Bridged Chains: SQUID and μSR Studies. Inorg. Chem. **2009**, 48 (1), 55–67. DOI: 10.1021/ic801094m.

57. Katz, M. J.; Aguiar, P. M.; Batchelor, R. J.; Bokov, A. A.; Ye, Z.-G.; Kroeker, S.; Leznoff, D. B. Structure and Multinuclear Solid-State NMR of a Highly Birefringent Lead−Gold Cyanide Coordination Polymer. J. Am. Chem. Soc. **2006**, 128 (11), 3669–3676. DOI: 10.1021/ja0566634.

58. Greer, B. J.; Michaelis, V. K.; Katz, M. J.; Leznoff, D. B.; Schreckenbach, G.; Kroeker, S. Characterising Lone-Pair Activity of Lead(II) by ^{207}Pb Solid-State NMR Spectroscopy: Coordination Polymers of $[N(CN)_2]^-$ and $[Au(CN)_2]^-$ with Terpyridine Ancillary Ligands. Chem. Eur. J. **2011**, 17 (13), 3609–3618. DOI: 10.1002/chem.201002913.

59. Thompson, J. R.; Ovens, J. S.; Williams, V. E.; Leznoff, D. B. Supramolecular Assembly of Bis(Benzimidazole)Pyridine: An Extended Anisotropic Ligand For Highly Birefringent Materials. Chem. Eur. J. **2013**, 19 (49), 16572–16578. DOI: 10.1002/chem.201302659.

60. Thompson, J. R.; Roberts, R. J.; Williams, V. E.; Leznoff, D. B. Birefringent, Emissive Coordination Polymers Incorporating Bis(Benzimidazole)Pyridine as an Anisotropic Building Block. CrystEngComm. **2013**, 15 (45), 9387. DOI: 10.1039/c3ce41556b.

61. Thompson, J. R.; Katz, M. J.; Williams, V. E.; Leznoff, D. B. Structural Design Parameters for Highly Birefringent Coordination Polymers. Inorg. Chem. **2015**, 54 (13), 6462–6471. DOI: 10.1021/acs.inorgchem.5b00749.

62. Thompson, J. R.; Goodman-Rendall, K. A. S.; Leznoff, D. B. Birefringent, Emissive Cyanometallate-Based Coordination Polymer Materials Containing Group(II) Metal-Terpyridine Building Blocks. Polyhedron **2016**, 108, 93–99. DOI: 10.1016/j.poly.2015.12.026.

63. Brown, M. L. Structural Insights into f -Block Heterobimetallic Dicyanoaurate Coordination Polymers. Ph.D. Dissertation, Simon Fraser University, 8888 University Drive, Burnaby, B.C. Canada, V5A 1S6, **2021**.

64. Korčok, J. L.; Katz, M. J.; Leznoff, D. B. Impact of Metallophilicity on “Colossal” Positive and Negative Thermal Expansion in a Series of Isostructural Dicyanometallate Coordination Polymers. J. Am. Chem. Soc. **2009**, 131 (13), 4866–4871. DOI: 10.1021/ja809631r.

65. Roberts, R. J.; Ahern, J. C.; Patterson, H. H.; Leznoff, D. B. Ce/$Au(CN)_2^-$ - Based Coordination Polymers Containing and Lacking Aurophilic Interactions. Eur. J. Inorg. Chem. **2016**, 2016 (13–14), 2082–2087. DOI: 10.1002/ejic.201600174.

66. Patterson, H. H.; Roper, G.; Biscoe, J.; Ludi, A.; Blom, N. Single-Crystal Luminescence Study of the Layered Compound $KAu(CN)_2$. Inorg. Chem., **1986**, 25 (17), 2947–2951. DOI: 10.1021/ic00237a006

67. Yersin, H.; Trümbach, D.; Strasser, J.; Patterson, H. H.; Assefa, Z. Tunable Radiationless Energy Transfer in $Eu[Au(CN)_2]_3 \cdot 3H_2O$ by High Pressure. Inorg. Chem. **1998**, 37 (13), 3209–3216. DOI: 10.1021/ic980252p.

68. Strasser, J.; Yersin, H.; Patterson, H. H. Effect of High Pressure on the Emission Spectrum of Single Crystals of $Tl[Au(CN)_2]$. Chem. Phys. Lett. **1998**, 295 (1–2), 95– 98. DOI: 10.1016/S0009-2614(98)00915-4.

69. Rawashdeh-Omary, M. A.; Larochelle, C. L.; Patterson, H. H. Tunable Energy Transfer from Dicyanoaurate(I) and Dicyanoargentate(I) Donor Ions to Terbium(III) Acceptor Ions in Pure Crystals. Inorg. Chem. **2000**, 39 (20), 4527–4534. DOI: 10.1021/ic990510y.

70. Rawashdeh-Omary, M. A.; Omary, M. A.; Patterson, H. H.; Fackler, J. P. Excited-State Interactions for $[Au(CN)_2^-]_n$ and $[Ag(CN)_2^-]_n$ Oligomers in Solution. Formation of Luminescent Gold−Gold Bonded Excimers and Exciplexes. J. Am. Chem. Soc. **2001**, 123 (45), 11237–11247. DOI: 10.1021/ja011176j.

71. Assefa, Z.; Omary, M. A.; McBurnett, B. G.; Mohamed, A. A.; Patterson, H. H.; Staples, R. J.; Fackler, J. P. Syntheses, Structure, and Photoluminescence Properties of the 1-Dimensional Chain Compounds $[(TPA)_2Au][Au(CN)_2]$ and (TPA)AuCl (TPA = 1,3,5-Triaza-7-Phosphaadamantane). Inorg. Chem. **2002**, 41 (24), 6274–6280. DOI: 10.1021/ic025784r.

72. Hettiarachchi, S. R.; Rawashdeh-Omary, M. A.; Kanan, S. M.; Omary, M. A.; Patterson, H. H.; Tripp, C. P. Spectroscopic Studies of “Exciplex Tuning” for Dicyanoaurate(I) Ions Doped in Potassium Chloride Crystals. J. Phys. Chem. B **2002**, 106 (39), 10058–10064. DOI: 10.1021/jp0209594.

73. Lu, H.; Yson, R.; Ford, J.; Tracy, H. J.; Carrier, A. B.; Keller, A.; Mullin, J. L.; Poissan, M. J.; Sawan, S.; Patterson, H. H. Tunable Energy Transfer from D10 Heterobimetallic Dicyanide(I) Donor Ions to Terbium(III) Acceptor Ions in Luminescent Tb[AgxAu1−x(CN)2]3 (X=0→1). Chem. Phys. Lett. **2007**, 443 (1–3), 55–60. DOI: 10.1016/j.cplett.2007.06.011.

74. Guo, Z.; Yson, R. L.; Patterson, H. H. Tunable Energy Transfer between $[Au(CN)_2]_n^-$ Luminescent Nanoclusters and Rare Earth Ions in Aqueous Solution. Chem. Phys. Lett. **2007**, 433 (4–6), 373–378. DOI: 10.1016/j.cplett.2006.11.019.

75. Hettiarachchi, S. R.; Schaefer, B. K.; Yson, R. L.; Staples, R. J.; Herbst-Irmer, R.; Patterson, H. H. Observation of a Mixed-Metal Transition in Heterobimetallic Au/Ag Dicyanide Systems. Inorg. Chem. **2007**, 46 (17), 6997–7004. DOI: 10.1021/ic700780k.

76. Welch, D.; Baril-Robert, F.; Li, X.; Patterson, H. H. Luminescence and Simulation of Mixed Metal Nanoclusters of Dicyanoargentate(I) and Dicyanoaurate(I) in Alkali Halides. Inorganica Chim. Acta **2011**, 370 (1), 279–285. DOI: 10.1016/j.ica.2011.01.076.

77. Abouelwafa, A. S.; Anson, C. E.; Hauser, A.; Patterson, H. H.; Baril-Robert, F.; Li, X.; Powell, A. K. Photophysical Properties of $\{[Au(CN)_2]^-\}_2$ Dimers Trapped in a Supramolecular Electron-Acceptor Organic Framework. Inorg. Chem. **2012**, 51 (3), 1294–1301. DOI: 10.1021/ic201109u.

78. Boucher, C.; Drew, M. G. B.; Giddings, P.; Harwood, L. M.; Hudson, M. J.; Iveson, P. B.; Madic, C. 12-Coordinate Complexes Formed by the Early Lanthanide Metals with 2,6-Bis(-1,2,4-Triazin-3-Yl)-Pyridine. Inorg. Chem. Commun. **2002**, 5 (8), 596–599. DOI: 10.1016/S1387-7003(02)00489-6.

79. Katz, M. J.; Ramnial, T.; Yu, H.-Z.; Leznoff, D. B. Polymorphism of $Zn[Au(CN)_2]_2$ and Its Luminescent Sensory Response to NH_3 Vapor. J. Am. Chem. Soc. **2008**, 130 (32), 10662–10673. DOI: 10.1021/ja801773p.

80. Hoskins, B. F.; Robson, R.; Scarlett, N. V. Y. Six Interpenetrating Quartz-Like Nets in the Structure of $ZnAu_2(CN)_4$. Angew. Chem. Int. Ed. Engl. **1995**, 34 (11), 1203–1204. DOI: 10.1002/anie.199512031.

81. Agustí, G.; Gaspar, A. B.; Muñoz, M. C.; Lacroix, P. G.; Real, J. A. Spin Crossover and Paramagnetic Behaviour in Two-Dimensional Iron(II) Coordination Polymers with Stilbazole Push–Pull Ligands. Aust. J. Chem. **2009**, 62 (9), 1155. DOI: 10.1071/CH09100.

82. Forward, J. M.; Bohmann, D.; Fackler, J. P.; Staples, R. J. Luminescence Studies of Gold(I) Thiolate Complexes. Inorg. Chem. **1995**, 34, 6330–6336. DOI: 10.1021/ic00129a019.

83. Pyykkö, P.; Li, J.; Runeberg, N. Predicted Ligand Dependence of the Au(I)…Au(I) Attraction in $(XAuPH_3)_2$. Chem. Phys. Lett. **1994**, 218 (1–2), 133–138. DOI: 10.1016/0009-2614(93)E1447-O.

84. Pearson, R. G. Absolute Electronegativity and Hardness: Application to Inorganic Chemistry. Inorg. Chem. **1988**, 27 (4), 734–740. DOI: 10.1021/ic00277a030.

85. Mansour, M. A.; Connick, W. B.; Lachicotte, R. J.; Gysling, H. J.; Eisenberg, R. Linear Chain Au(I) Dimer Compounds as Environmental Sensors: A Luminescent Switch for the Detection of Volatile Organic Compounds. J. Am. Chem. Soc. **1998**, 120 (6), 1329–1330. DOI: 10.1021/ja973216i.

86. Roberts, J. R. Exploring gold(I) as a luminophore for emissive coordination polymers. Ph.D. Dissertation, Simon Fraser University, 8888 University Drive, Burnaby, B.C. Canada, V5A 1S6, **2017**.

87. Forward, J. M.; Bohmann, D.; Fackler, J. P.; Staples, R. J. Luminescence Studies of Gold(I) Thiolate Complexes. Inorg. Chem. **1995**, 34, 6330–6336.

88. Pyykkö, P.; Li, J.; Runeberg, N. Predicted Ligand Dependence of the Au(I)…Au(I) Attraction in $(XAuPH_3)_2$. Chem. Phys. Lett. **1994**, 218 (1–2), 133–138. DOI: 10.1016/0009-2614(93)E1447-O.

89. Muñiz, J.; Wang, C.; Pyykkö, P. Aurophilicity: The Effect of the Neutral Ligand L on $[\{ClAuL\}_2]$ Systems. Chem. Eur. J. **2011**, 17 (1), 368–377. DOI: 10.1002/chem.201001765.

90. Schmidbaur, H.; Schier, A. A Briefing on Aurophilicity. Chem. Soc. Rev. **2008**, 37 (9), 1931. DOI: 10.1039/b708845k.

91. Leznoff, D. B.; Xue, B.-Y.; Batchelor, R. J.; Einstein, F. W. B.; Patrick, B. O. Gold−Gold Interactions as Crystal Engineering Design Elements in Heterobimetallic Coordination Polymers. Inorg. Chem. **2001**, 40 (23), 6026–6034. DOI: 10.1021/ic010756e.

92. Pyykkö, P.; Desclaux, J. P. Relativity and the Periodic System of Elements. Acc. Chem. Res. **1979**, 12 (8), 276–281. DOI: 10.1021/ar50140a002.

93. Yan, L.-L.; Yao, L.-Y.; Ng, M.; Yam, V. W.-W. Stimuli-Responsive and Structure-Adaptive Three-Dimensional Gold(I) Cluster Cages Constructed via “De-Aurophilic” Interaction Strategy. J. Am. Chem. Soc. **2021**, 143 (45), 19008–19017. DOI: 10.1021/jacs.1c07971.

94. Roberts, R. J.; Le, D.; Leznoff, D. B. Controlling Intermolecular Aurophilicity in Emissive Dinuclear Au(I) Materials and Their Luminescent Response to Ammonia Vapour. Chem. Commun. **2015**, 51 (76), 14299–14302. DOI: 10.1039/C5CC05277G.

95. Jin, M.; Ito, H. Solid-State Luminescence of Au(I) Complexes with External Stimuli-Responsive Properties. J. Photochem. Photobiol. C. **2022**, 51, 100478. DOI: 10.1016/j.jphotochemrev.2021.100478.

96. Seki, T.; Sakurada, K.; Muromoto, M.; Ito, H. Photoinduced Single-Crystal-to-Single-Crystal Phase Transition and Photosalient Effect of a Gold(I) Isocyanide Complex with Shortening of Intermolecular Aurophilic Bonds. Chem. Sci. **2015**, 6 (2), 1491–1497. DOI: 10.1039/C4SC02676D.

97. Xue, P.; Ding, J.; Wang, P.; Lu, R. Recent Progress in the Mechanochromism of Phosphorescent Organic Molecules and Metal Complexes. J. Mater. Chem. C **2016**, 4 (28), 6688–6706. DOI: 10.1039/C6TC01503D.

98. Pells, J. A.; Guan, D.; Leznoff, D. B. Heterobimetallic Ln(III)-Containing Materials Based on One-Dimensional Aurophilic Chains of Gold(I) Dithiolate Dimers and Their Vapochromic Response to DMF. Eur. J. Inorg. Chem. **2022**, 2022 (14), e202200049. DOI:10.1002/ejic.202200049.

99. Xue, P.; Ding, J.; Wang, P.; Lu, R. Recent Progress in the Mechanochromism of Phosphorescent Organic Molecules and Metal Complexes. J. Mater. Chem. C **2016**, 4 (28), 6688–6706. DOI: 10.1039/C6TC01503D.

100. Chung, K.; Kwon, M. S.; Leung, B. M.; Wong-Foy, A. G.; Kim, M. S.; Kim, J.; Takayama, S.; Gierschner, J.; Matzger, A. J.; Kim, J. Shear-Triggered Crystallization and Light Emission of a Thermally Stable Organic Supercooled Liquid. ACS Cent. Sci. **2015**, 1 (2), 94–102. DOI: 10.1021/acscentsci.5b00091.

101. Sagara, Y.; Yamane, S.; Mitani, M.; Weder, C.; Kato, T. Mechanoresponsive Luminescent Molecular Assemblies: An Emerging Class of Materials. Adv. Mater. **2016**, 28 (6), 1073–1095. DOI: 10.1002/adma.201502589.

102. SC-30 Integrating Sphere Module for FS5 User Guide, Edinburgh Instruments Ltd.,
Livingston, UK, **2017**.

103. De Mello, J. C.; Wittmann, H. F.; Friend, R. H. An Improved Experimental Determination of External Photoluminescence Quantum Efficiency. Adv. Mater. **1997**, 9 (3), 230–232. DOI: 10.1002/adma.19970090308.

104. Waseda, Y.; Matsubara, E.; Shinoda, K. X-Ray Diffraction Crystallography: Introduction, Examples and Solved Problems; Springer Berlin Heidelberg: Berlin, Heidelberg, **2011**. DOI: 10.1007/978-3-642-16635-8.

105. Glusker, J. P.; Trueblood, K. N. Crystal structure Analysis: A Primer (International Union of Crystallography Texts on Crystallography Book 14), 3rd Ed; Oxford University Press: New York, **1972**, DOI: 10.1093/oso/9780199576340.001.0001.

106. Khan, M. N. I.; Wang, S.; Fackler, J. P. Synthesis and Structural Characterization of the Gold Complex, $[n\text{-}Bu_4N]_2[Au_2(i\text{-}MNT)_2]$ (i-MNT = 1,1-Dicyanoethylene-2,2-Dithiolate) and Its Oxidative-Addition Products $[Ph_4As]_2[Au_2(i\text{-}MNT)_2Cl_2]$, $[n\text{-}Bu_4N]_2[Au_2(i\text{-}MNT)_2Br_2]$, and $[n\text{-}Bu_4N][Au(i\text{-}MNT)_2]$. Spectral Studies of the Disproportionation of $[n\text{-}Bu_4N]_2[Au_2(i\text{-}MNT)_2X_2]$ (X = Cl-, Br-, I-) into $[n\text{-}Bu_4N][AuX_2]$ and $[n\text{-}Bu_4N][Au(i\text{-}MNT)_2]$. Inorg. Chem. **1989**, 28 (18), 3579–3588. DOI: doi.org/10.1021/ic00317a036.

107. Baril-Robert, F.; Radtke, M. A.; Reber, C. Pressure-Dependent Luminescence Properties of Gold(I) and Silver(I) Dithiocarbamate Compounds. J. Phys. Chem. C **2012**, 116 (3), 2192–2197. DOI: 10.1021/jp206766p.

108. Yam, V. W.-W.; Cheng, E. C.-C. Photochemistry and Photophysics of Coordination Compounds II, ed. Balzani V. and Campagna S.; Springer Berlin Heidelberg: Berlin, Heidelberg, **2007**, pp. 269 – 309. DOI: 10.1007/128_2007_127.

109. Yang, L.; Wang, H.; Li, D.; Li, L.; Lou, X.; Liu, H. Self-Nucleation and Self-Assembly of Highly Fluorescent Au_5 Nanoclusters for Bioimaging. Chem. Mater. **2018**, 30 (15), 5507–5515. DOI: 10.1021/acs.chemmater.8b02770.

110. Roberts, R. J.; Bélanger-Desmarais, N.; Reber, C.; Leznoff, D. B. The luminescence properties of linear vs. kinked aurophilic 1-D chains of bis(dithiocarbamate)gold(I) dimers. Chem. Commun. **2014**, 50(24), 3148. DOI: 10.1039/c3cc47944g.

111. Seth, S.; Jhulki, S. Porous flexible frameworks: origins of flexibility and applications. Mater. Horiz., **2021**, 8, 700–727. DOI: 10.1039/D0MH01710H.

112. Seki, T.; Kashiyama, K.; Yagai, S.; Ito, H. Tuning the Lifetime of Transient Phases of Mechanochromic Gold Isocyanide Complexes through Functionalization of the Terminal Moieties of Flexible Side Chains. Chem. Lett. **2017**, 46 (9), 1415–1418. DOI: 10.1246/cl.170482.

113. Bruker Corporation. APEX 3 Crystallography Software Suite. Bruker AXS Inc.: Madison, WI, 53711, USA.

114. Sheldrick, G. M. SHELXT – Integrated space-group and crystal-structure determination. Acta Crystallogr. **2015**, 71(1), 3–8. DOI: 10.1107/S2053273314026370.

115. Dolomanov, O.V.; Bourhis, L.J.; Gildea, R.J.; Howard, J.A.K.; Puschmann, H., OLEX2: A complete structure solution, refinement, and analysis program. *J. Appl. Cryst.* **2009**, 42, 339–341.

116. Momma, K; Izumi, F. Vesta 3 for three-dimensional visualization of crystal, volumetric and morphology data. J. Appl. Crystallogr. **2011**, 44, 1272–1276.

117. Lin, Z.; Cai, J. J.; Scriven, L. E.; Davis, H. T. Spherical-to-Wormlike Micelle Transition in CTAB Solutions. J. Phys. Chem. **1994**, 98 (23), 5984–5993. DOI: 10.1021/j100074a027.

118. Coppola, L.; Gianferri, R.; Nicotera, I.; Oliviero, C.; Antonio Ranieri, G. Structural Changes in CTAB/H2O Mixtures Using a Rheological Approach. Phys. Chem. Chem. Phys. **2004**, 6 (9), 2364. DOI: 10.1039/b316621j.

119. Huang, M. H.; Soyez, H. M.; Dunn, B. S.; Zink, J. I.; Sellinger, A.; Brinker, C. J. In Situ Fluorescence Probing of the Chemical and Structural Changes during Formation of Hexagonal Phase Cetyltrimethylammonium Bromide and Lamellar Phase CTAB/Poly(Dodecylmethacrylate) Sol–Gel Silica Thin Films. J. Sol-Gel Sci. Technol. **2008**, 47 (3), 300–310. DOI: 10.1007/s10971-008-1755-7.

120. Liu, Y.; Tourbin, M.; Lachaize, S.; Guiraud, P. Silica Nanoparticles Separation from Water: Aggregation by Cetyltrimethylammonium Bromide (CTAB). Chemosphere **2013**, 92 (6), 681–687. DOI: 10.1016/j.chemosphere.2013.03.048

121. Li, Y.; Guo, Y.; Bao, M.; Gao, X. Investigation of Interfacial and Structural Properties of CTAB at the Oil/Water Interface Using Dissipative Particle Dynamics Simulations. J. Colloid Interface Sci. **2011**, 361 (2), 573–580. DOI: 10.1016/j.jcis.2011.05.078.

122. Hatchard, W. R. The synthesis of Isothiazoles. I. 3,5-Dichloro-4isothiazolecarbonitrile and Its Derivatives. J. Org. Chem. **1964**, 29, 660–665. DOI: 10.1021/jo01026a033.

123. Usón, R.; Laguna, A.; de la Orden, M. U.; Arrese, M. L.; Pentachlorophenyl Complexes of Gold(I) and Gold(III). In Synthesis and Reactivity in Inorganic and Metal-Organic Chemistry. 18(1), 69–82. DOI: 10.1080/00945718408055895.

124. Rendell, D. Fluorescence and Phosphorescence Spectroscopy 1st ed. John Wiley & Sons Inc: London, **1987**.

125. Lakowicz, R. J. Principle of Fluorescence Spectroscopy 3rd ed. Springer: New York, **2006**.

126. Callister, D. W. Fundamentals of Materials Science and Engineering 5th ed. John Wiley & Sons Inc: New York, **2001**.

Appendix.

Crystallographic Tables

Table A1: Crystallographic for [Cation][Au^{III}(*i*-mnt)$_2$]

[Cation]$^+$	[$(C_6H_{13})_4N$]	[$C_{12}Me_3N$]
Chemical formula	$C_{33}H_{55}N_5S_4Au$	$C_{23}H_{26}N_5S_4Au$
Formula weight (g·mol^{-1})	845.05	696.716
Crystal system	Triclinic	Monoclinic
Space group	P-1	$P2_1/n$
a (Å)	10.02151(6)	11.571(2)
b (Å)	14.0295(10)	8.4138(15)
c (Å)	14.2374(11)	29.751(5)
α (°)	98.742(3)	90
β (°)	103.802(2)	93.159(7)
γ (°)	95.570(3)	90
V (Å^3)	3422.4(2)	2892.0(9)
Z	19	2
T (K)	298	298
ρ_{calcd} (g·cm^{-3})	4.228	3.891
μ (mm^{-1})	36.997	32.066
R, R_w [$I_0 \geq 2\sigma(I_0)$]	0.0807, 0.2434	0.0515, 0.1353
Goodness of fit	0.988	0.986
Reflections [$I_0 \geq 2\sigma(I_0)$]	9517	7194

Table A2: Crystallographic Table for $[RMe_3N]_2[Au_2(i\text{-mnt})_2]$ systems

$[RMe_3N]^+$	$[C_4Me_3N]$	$[C_4Me_3N]\cdot MeCN$	$[C_8Me_3N]$	$[C_{10}Me_3N]$	$[C_{16}Me_3N]$
Chemical formula	$C_{22}H_{31}N_6S_4Au_2$	$C_{24}H_{39}N_7S_4Au_2$	$C_{30}H_{52}N_6S_4Au_2$	$C_{34}H_{60}N_6S_4Au_2$	$C_{46}H_{84}N_6Au_2S_4$
Formula weight ($g\cdot mol^{-1}$)	892.25	947.82	1018	1075	1243.42
Crystal system	Orthorhombic	Orthorhombic	Tetragonal	Tetragonal	Triclinic
Space group	*P*ccn	*P*ccn	$P4_2/n$	$P4_2/n$	$P-1$
a (Å)	11.8045(4)	11.8692(6)	19.3453(8)	19.6131(6)	11.4743(15)
b (Å)	24.8794(10)	24.2777(11)	19.3453(8)	19.6131(6)	11.6209(14)
c (Å)	11.6530(4)	11.5383(5)	11.3345(4)	11.3981(4)	22.395(3)
α (°)	90	90	90	90	82.300(4)
β (°)	90	90	90	90	78.901(5)
γ (°)	90	90	90	90	73.578(4)
V ($Å^3$)	3422.4(2)	3324.8(3)	4241.8(3)	4384.5(2)	2800.7(6)
Z	4	4	4	4	2
T (K)	296	220	220	299	296
ρ_{calcd} ($g\cdot cm^{-3}$)	1.732	1.893	1.596	1.629	1.474
μ (mm^{-1})	8.826	9.091	14.854	14.395	5.415
R, R_w [$I_0 \geq 2\sigma(I_0)$]	0.0482, 0.2169	0.0466, 0.1356	0.0565, 0.2976	0.0816, 0.2526	0.0480, 0.1154
Goodness of fit	0.9839	1.0307	1.1237	1.0561	0.9651
Reflections [$I_0 \geq 2\sigma(I_0)$]	3125	4138	3538	3716	19379

Table A3: Selected bond lengths, bond angles, and torsional angles in $[RMe_3N]_2[Au_2(i\text{-mnt})_2]$

$[RMe_3N]$	$[C_4Me_3N]$	$[C_4Me_3N]\cdot MeCN$	$[C_8Me_3N]$	$[C_{10}Me_3N]$	$[C_{16}Me_3N]$
Au – Au_{intra} (Å)	2.8170(7)	2.7992(7)	2.7827(9)	2.7836(13)	2.8151(6)
Au – Au_{inter} (Å)	3.0095(7)	2.9700(7)	2.8845(9)	2.9154(13)	3.0090(5)
Au1 – Au2 – Au1' (°)	180	180	180	180	172.062(18)
Au – S (Å)	2.286(4), 2.287(4)	2.287(4), 2.292(3)	2.279(4), 2.279(3)	2.282(6), 2.293(6)	2.291(3), 2.285(3) 2.288(2), 2.280(2)
C – S (Å)	1.729(10), 1.723(10)	1.727(9), 1.737(10)	1.714(9), 1.729(9)	1.175(18), 1.729(17)	1.175(7), 1.707(6) 1.726(8), 1.730(6)
C = C (Å)	1.387(16)	1.383(15)	1.360(14)	1.40(3)	1.365(11), 1.391(10)
C ≡ N (Å)	1.17(2), 1.138(19)	1.145(16), 1.138(18)	1.152(18), 1.142(19)	1.20(4) 1.13(4)	1.130(9), 1.140(13) 1.146(10),
S – Au – S (°)	177.38(12), 177.33(18)	177.19(12), 177.15(12)	173.45(12), 174.24(12)	173.9(3), 174.96(18)	173.12(2) 173.02(7)
C1 – S1 – S2 – C2 (°)	53.2(8)	53.8(8)	22.8(8)	37.1(14)	0.9(6) , 8.1(6)
C1 – S3 – S4 – C2 (°)	44.4(8)	47.2(8)	26.4(8)	28.7(15)	0.9(6), 8.1(6)

Table A4: Crystallographic table for $[R_2(imi)]_2[Au_2(i\text{-mnt})_2]$

R	Me	*i*-Pr	Me_3Ph
Chemical formula	$C_{81}H_{84}N_{39}Au_8O_3S_{16}$	$C_{43}H_{64}S_8Au_4N_{16}$	$C_{50}H_{54}Au_2N_8S_4$
Formula weight ($g \cdot mol^{-1}$)	3632.38	1849.45	1289.18
Crystal system	Orthorhombic	Monoclinic	Monoclinic
Space group	$P2_12_12_1$	Pc	C2/c
a (Å)	14.534(8)	12.0352(14)	32.046(2)
b (Å)	17.287(7)	24.361(3)	13.7852(10)
c (Å)	45.335(18)	11.5229(12)	11.7655(10)
α (°)	90	90	90
β (°)	90	100.610(3)	94.966(4)
γ (°)	90	90	90
V ($Å^3$)	11390(9)	3320.7(6)	5178.1(7)
Z	2	29	4
T (K)	150.15	298	298
ρ_{calcd} ($g \cdot cm^{-3}$)	2.118	3.931	1.654
μ (mm^{-1})	22.077	32.397	5.863
R, R_w [$I_0 \geq 2\sigma(I_0)$]	0.0513, 0.1059	0.0933, 0.2473	0.0279, 0.0572
Goodness of fit	1.074	1.066	1.012
Reflections [$I_0 \geq 2\sigma(I_0)$]	249857	7194	48198

Table A5: Cambridge Crystallographic Data Center (CCDC) crystallographic deposition number for $Q_2[Au_2(i\text{-mnt})_2]$.

Q	Deposition Number
C_4Me_3N	2365649
$C_4Me_3N \cdot MeCN$	2365647
C_8Me_3N	2365646
$C_{10}Me_3N$	2365648
$C_{16}Me_3N$	2365650
$[(Me_3Ph)_2(imi)]$	2379948